Fall 8-24-2017

Nonlinear Waves, Instabilities and Singularities in Plasma and Hydrodynamics

Denis Albertovich Silantyev
University of New Mexico - Main Campus

Recommended Citation

Silantyev, Denis Albertovich. "Nonlinear Waves, Instabilities and Singularities in Plasma and Hydrodynamics." (2017). https://digitalrepository.unm.edu/math_etds/121

Denis Albertovich Silantyev

Candidate

Mathematics and Statistics

Department

This dissertation is approved, and it is acceptable in quality and form for publication:

Approved by the Dissertation Committee:

Prof. Pavel Lushnikov, Chair

Prof. Alexander Korotkevich, Member

Prof. Evangelos Coutsias, Member

Prof. Jean-Claude Diels, Member

NONLINEAR WAVES, INSTABILITIES AND SINGULARITIES IN PLASMA AND HYDRODYNAMICS

by

Denis Albertovich Silantyev

B.S., Applied Mathematics and Physics, Moscow Institute of Physics and Technology, 2007

M.S., Mathematics, University of New Mexico, 2011

DISSERTATION

Submitted in Partial Fulfillment of the
Requirements for the Degree of

Doctor of Philosophy
Mathematics

The University of New Mexico

Albuquerque, New Mexico

December, 2017

ACKNOWLEDGMENTS

I am extremely grateful to my scientific advisor, Professor Pavel Lushnikov, for his solid support and numerous advice, extensive knowledge that he shared with me during uncountable discussions, and tremendous patience as I was working my way towards this degree.

I would like to express my gratitude to Dr. Harvey Rose at Los Alamos National Lab separately for his guidance, research ideas and extensive discussions.

I am thankful to Prof. Alexander Korotkevich, Prof. Daniel Appelö, Prof. Stephen Lau and Prof. Deborah Sulsky at the Department of Mathematics and Statistics at the University of New Mexico and Dr. Natalia Vladimirova who provided a lot of useful advice and discussions.

I would also like to thank my family for their immense support and encouragement.

NONLINEAR WAVES, INSTABILITIES AND SINGULARITIES IN PLASMA AND HYDRODYNAMICS

by

Denis Albertovich Silantyev

B.S., Applied Mathematics and Physics, Moscow Institute of Physics and Technology, 2007
M.S., Mathematics, University of New Mexico, 2011
Ph.D., Mathematics, University of New Mexico, 2017

ABSTRACT

Nonlinear effects are present in almost every area of science as soon as one tries to go beyond the first order approximation. In particular, nonlinear waves emerge in such areas as hydrodynamics, nonlinear optics, plasma physics, quantum physics, etc. The results of this work are related to nonlinear waves in two areas, plasma physics and hydrodynamics, united by concepts of instability, singularity and advanced numerical methods used for their investigation.

The first part of this work concentrates on Langmuir wave filamentation instability in the kinetic regime of plasma. In Internal Confinement Fusion Experiments (ICF) at National Ignition Facility (NIF), where attempts are made to achieve fusion by compressing a small target by many powerful lasers to extremely high temperatures and pressures, plasma is created in the first moments of the laser reaching the

target and undergoes complicated dynamics. Some of the most challenging difficulties arise from various plasma instabilities that occur due to interaction of the laser beam and a plasma surrounding the target. In this work we consider one of such instabilities that describes a decay of nonlinear plasma wave (aka Langmuir wave), initially excited due to interaction of the laser beam with the plasma, into many filaments in direction perpendicular to the laser beam, therefore named Langmuir filamentation (or transverse) instability. This instability occurs in the kinetic regime of plasma,$k\lambda_D > 0.2$, where k is the wavenumber and λ_D is the Debye length. The filamentation of Langmuir waves in turn leads to the saturation of the stimulated Raman scattering (SRS) [1] in laser-plasma interaction experiments which plays an essential role in ICF experiments.

The challenging part of this work was that unlike in hydrodynamics we needed to use fully kinetic description of plasma to capture the physics in question properly, meaning that we needed to consider the distribution function of charged particles and its evolution in time not only with respect to spatial coordinates but with respect to velocities as well. To study Langmuir filamentation instability in its simplest form we performed 2D+2V numerical simulations. Taking into account that the distribution function in question was 4-dimensional function, making these simulation quite challenging, we developed an efficient numerical method making these simulations possible on modern desktop computers.

Using the developed numerical method we studied how Langmuir wave filamentation instability depends on the parameters of the Langmuir wave such as wave length and amplitude that are relevant to ICF experiments. We considered several types of Langmuir waves, including nonlinear Langmuir waves exited by external electric field as well as an idealized approximation of such Langmuir waves [2] by a particular family of Bernstein-Greene-Kruskal (BGK) modes [3] that bifurcates from the linear Langmuir wave. The results of these simulations were compared to the theoretical predictions [4] in our recent papers [5, 6]. An alternative approach to overcome computational difficulty of this problem was considered by our research group in Ref. [7]. It involves reducing the number of transverse direction in the model therefore lowering computational difficulty at a cost of lesser accuracy of the model.

The second part of this work concentrates on 2D free surface hydrodynamics and in particular on computing Stokes waves with high-precision using conformal maps and spectral methods. Stokes waves are fully nonlinear periodic gravity waves propagating with the constant velocity on a free surface of two-dimensional potential flow of the ideal incompressible fluid of infinite depth. The increase of the scaled wave height H/λ, where H is the wave height and λ is the wavelength, from $H/\lambda = 0$ to the critical value H_{max}/λ marks the transition from almost linear wave to a strongly nonlinear limiting Stokes wave. The Stokes wave of the greatest height $H = H_{max}$ has an angle of 120° at the crest [8]. The non-limiting Stokes waves describe ocean swell and the slow time evolution of the Stokes wave toward its limiting form is one of the possible routes to wave-breaking and whitecapping in full wave dynamics. Wave-breaking and whitecapping carry away significant part of energy and momenta of gravity waves [9, 10]. Formation of the limiting Stokes wave is also considered to be a probable final stage of evolution of a freak (or rogue) wave in the ocean resulting in formation of approximate limiting Stokes wave for a limited period of time with a following wave breaking and disintegration of the wave or whitecapping and attenuation of the freak wave into wave of regular amplitude [11, 12, 13]. Thus the approach of non-limiting Stokes wave to the limiting Stokes wave has both significant theoretical and practical interests.

To obtain Stokes wave fully nonlinear Euler equations describing the flow can be reformulated in terms of conformal map of the fluid domain into the complex lower half-plane, with fluid free surface mapped into the real line. This description is convenient for analysis and numerical simulations since the whole problem is then reduced to a single nonlinear equation on the real line. Having computed solutions on the real line we extend them to the rest of the complex plane to analyze the singularities above real line. The distance v_c from the closest singularity in the upper half-plane to the real line goes to zero as we approach the limiting Stokes wave with maximum hight H_{max}/λ, which is the reason for the widening of the solution's Fourier spectrum.

In this dissertation we demonstrate a new approach that allows one to overcome this difficulty. We improve performance of our numerical method drastically by introducing second conformal map that pushes the singularity higher into the upper half-plane and correspondingly shrinks the spectrum of the solution while making the computations of extremely nonlinear solutions much more efficient. Using this approach we were able to demonstrate and confirm a predicted phenomenon of intricate parameter oscillation [14, 15, 16] for strongly nonlinear Stokes waves.

List of Papers

This dissertation is based on the following papers:

I Pavel M. Lushnikov, Harvey A. Rose, Denis A. Silantyev, Natalia Vladimirova,
Vlasov multi-dimensional model dispersion relation,
Physics of Plasmas, 21(7):072103, 2014.
Contributions: D. A. Silantyev developed codes, performed numerical simulations and analysis and wrote parts of Sections I and III-VII of the manuscript. H.A.Rose was the main inspirer of the paper and wrote Section II and partially Sections I and III. P.M. Lushnikov wrote the rest of the manuscript. The ideas were developed in close collaboration between all authors.

II Denis A. Silantyev, Pavel M. Lushnikov, and Harvey A. Rose,
Langmuir wave filamentation in the kinetic regime. I. Transverse instability of Bernstein-Greene-Kruskal modes and multidimensional Vlasov simulations,
Physics of Plasmas, 24(4):042104, 2017.
Contributions: D. A. Silantyev developed codes, performed numerical simulations, analyzed the results and wrote the manuscript except for Sections II and part of IIIC. P.M. Lushnikov wrote Section II of the manuscript and contributed to various sections of the manuscript as well. H.A.Rose wrote most of Section IIIC and contributed significantly to the formulation of the problem. The ideas were developed in close collaboration between all authors.

III Denis A. Silantyev, Pavel M. Lushnikov, and Harvey A. Rose,
Langmuir wave filamentation in the kinetic regime. II. Weak and strong pumping of nonlinear electron plasma waves as the route to filamentation,
Physics of Plasmas, 24(4):042105, 2017.
Contributions: D. A. Silantyev developed codes, performed numerical simulations, analyzed the results and wrote most of the manuscript except for Sections I. P.M. Lushnikov wrote Section I of the manuscript and contributed to various sections of the manuscript as well. The ideas were developed in close collaboration between all authors.

IV Pavel M. Lushnikov, Sergey A. Dyachenko, and Denis A. Silantyev,
New conformal mapping for adaptive resolving of the complex singularities of stokes wave,
Proceedings of the Royal Society of London A: Mathematical, Physical and Engineering Sciences, 473(2202), 2017.
Contributions: D. A. Silantyev and S.A. Dyachenko developed codes, performed numerical simulations and analyzed the results. P.M. Lushnikov provided analysis in Sections 2-4. All authors contributed various ideas as well as writing the manuscript in approximately equal parts.

Contents

Part I

NONLINEAR WAVES AND INSTABILITIES IN COLLISIONLESS PLASMA

Chapter 1

Introduction

Propagation of intense laser beam in high temperature plasma relevant for the inertial confinement fusion results in significant loss of laser energy to stimulated Raman back-scatter (SRS) [1] producing the electromagnetic waves at different frequency and Langmuir waves [17] (LW).

Consider a Langmuir wave [18, 19] wave packet with a typical wavenumber k. If $k\lambda_D \lesssim 0.2$, then the hydrodynamic approximation (the "fluid" regime) to LW dynamics is valid, where λ_D is the Debye length. In that regime a LW has a nonlinear frequency shift $\Delta\omega_{fluid}$, due to electron dynamics, proportional to the squared LW electric field amplitude E, i.e. $\Delta\omega_{fluid} \propto |E|^2$ [20, 21, 22]. As shown in Ref. [4], the transition from the fluid to the "kinetic" regime occurs at $k\lambda_D \sim 0.2$ when trapped electron effects cannot be ignored. The LW frequency shift due to electron trapping, $\Delta\omega_{trapped}$, perturbatively varies as $\Delta\omega_{trapped} \propto |E|^{1/2}$ [23, 21, 24, 2, 4] with possible higher order corrections as discussed in Ref. [25]. Thus $\Delta\omega_{trapped}$ at $k\lambda_D \gtrsim 0.2$ may dominate [4, 26, 27, 28, 25] over $\Delta\omega_{fluid}$. See Fig 1.1 taken from [26] for schematics of various LW regimes. Negative $\Delta\omega_{trapped}$, with positive diffraction, imply LW filamentation [4, 29, 30, 31]. 3D particle-in-cell (PIC) [32]

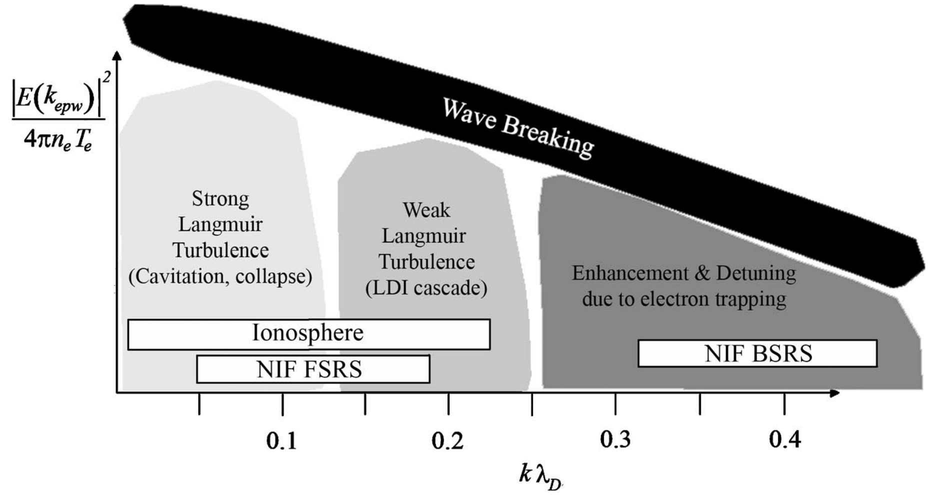

Figure 1.1: Pictorial view of nonlinear LW regimes.

simulation results have been interpreted as showing that the trapped electron LW filamentation instability can saturate [33, 34] stimulated Raman back-scatter (SRS) [1] by reducing the LWs coherence. In actual plasma, the SRS daughter LW is subject to other instabilities as well, such as LW-ion-acoustic decay (LDI). Fluid and kinetic regime LDI have been observed in SRS simulations [33, 35] while kinetic regime LDI has been experimentally [36] noted [26].

Additional complexity in the interpretation of experimental data gathered from laser-plasma interaction arises from instabilities of the laser beam [37, 38] coupled [39, 40, 41] to relatively low frequency ion-acoustic waves. Since direct experimental data pointing to kinetic LW filamentation has not been available, first principles simulation of pure LW dynamics is perhaps the cleanest way to "see" this phenomenon. Fully nonlinear PIC simulations [30] with Bernstein-Greene-Kruskal (BGK) mode [3] initial conditions have shown qualitative agreement with LW filamentation theory [4, 29], but the theory's finer points, such as instability thresholds, require a noise free model, namely the Vlasov simulations.

Here we address LW filamentation in the kinetic regime with $k\lambda_D > 0.3$ by studying the filamentation instability of BGK modes using 2D+2V (two velocity and two spatial dimensions) spectral Vlasov simulations. Our simulations only include collisionless electrostatic electron dynamics in a static neutralizing ion background, thereby excluding the LW ion-acoustic decay and ponderomotive LW filamentation instabilities, amongst others. BGK modes are constructed following the approach of Ref. [2] to approximate the adiabatically slow pumping by SRS. We concentrate on the linear stage of the filamentation instability development while observing strong LW filamentation in the nonlinear stage.

As an alternative we also consider BGK-like electron plasma waves (EPWs) prepared through either weak or strong SRS-like pumping(similar to Ref. [31]) and study their filamentation instability. We found that for small amplitudes these 1D BGK-like solutions obtained via weak pumping have the same transverse instability growth rates as BGK modes suggesting a universal mechanism for kinetic saturation of SRS in laser-plasma interaction experiments. We found that for two EPWs of the same amplitude strong pumping (vs. weak pumping) results in further increase of the growth rate of the transverse instability thus speeding up LW filamentation. We also compare the result of our numerical simulations to the corresponding results in Ref. [31, 42].

The part of dissertation is organized as follows. Chapter 2 introduces the Vlasov-Poisson system and its general BGK solutions (equilibria). In Chapter 3 we describe a special family [2] of 1D+1V BGK modes that bifurcate from linear LW (Section 3.1), outline their nonlinear dispersion relation (Section 3.2) and provide filamentation definition and analytical results on their growth rates (Section 3.3). In Chapter 4 we provide results of 2D+2V Vlasov simulations. Section 4.1 is devoted to the Vlasov simulations settings and our numerical method. Section 4.2 addresses filamentation instability results and their comparison with theory. Section 4.3 provides a comparison of the growth rates obtained in Section 4.2 with the growth rates from

PIC code simulations of Ref. [30].

Chapter 5 describes our method of producing BGK-like modes (pumped EPWs) by both weak pumping (Section 5.1) and strong pumping (Section 5.2) and their transverse instability analysis (Section 5.4). Chapter 6 is devoted to results of numerical 2D+2V Vlasov simulations of pumped EPWs and also provides a comparison of transverse instability of pumped EPWs with BGK modes (Section 6.2). In Chapter 7 the main results of this part are discussed.

Chapter 2

Basic Equations

The Vlasov equation for the phase space distribution function $f(\mathbf{r}, \mathbf{v}, t)$, in units such that electron mass m_e and charge e are normalized to unity, the spatial coordinate $\mathbf{r} = (x, y, z)$ to the electron Debye length λ_D, the time t to reciprocal electron plasma frequency, $1/\omega_{pe}$, [43] and the velocity $\mathbf{v} = (v_x, v_y, v_z)$ is normalized to the the electron thermal speed v_e, is

$$\left\{\frac{\partial}{\partial t} + \mathbf{v} \cdot \nabla + \mathbf{E} \cdot \frac{\partial}{\partial \mathbf{v}}\right\} f = 0, \tag{2.1}$$

where $\mathbf{E}$ is the electric field scaled to $k_B T_e/(\lambda_D e)$. Here T_e is the background electron temperature and k_B is the Boltzmann constant. Magnetic field effects are ignored for clarity. Then, in the electrostatic regime,

$$\mathbf{E} = -\nabla\Phi, \tag{2.2}$$

with the total electrostatic potential, Φ, given by

$$\Phi = \Phi^{ext} + \Phi^{int}, \tag{2.3}$$

where Φ^{ext} is prescribed external electrostatic potential and Φ^{int} is internal electrostatic potential Φ given by Poisson's equation

$$\nabla^2\Phi^{int} = 1 - \rho, \tag{2.4}$$

and electron density, ρ, is given by

$$\rho(\mathbf{r},t) = \int f(\mathbf{r},\mathbf{v},t)d\mathbf{v}. \tag{2.5}$$

The usual factor of 4π is absent from equation (2.4) because we choose to work in SI units and 1 in equation (2.4) comes from the neutralizing ion background.

Equations (2.1)-(2.5) form the closed Vlasov-Poisson system. Its finite amplitude travelling wave solutions, moving with phase velocity, v_φ, are called Bernstein-Greene-Kruskal (BGK) modes [3]. Here we assume without loss of generality that z is chosen in the direction of v_φ so that f assumes the form $f(\mathbf{r}_\perp, z - v_\varphi t, \mathbf{v})$, with $\mathbf{r}_\perp \equiv (x, y)$, and equation (2.1) reduces to

$$(v_z - v_\varphi)\frac{\partial}{\partial z}f + \mathbf{v}_\perp \cdot \nabla f + \mathbf{E} \cdot \frac{\partial}{\partial \mathbf{v}}f = 0. \tag{2.6}$$

The general solution of equations (2.2) and (2.6) in absence of external electric field ($\Phi^{ext} = 0$) is given by $f = g\,(W)$, where g is an arbitrary function of the single scalar argument

$$W \equiv \frac{(v_z - v_\varphi)^2}{2} + \frac{\mathbf{v}_\perp^2}{2} + \Phi(\mathbf{r}_\perp, z - v_\varphi t) \tag{2.7}$$

which is the single particle energy (kinetic energy in the moving reference frame plus electrostatic energy).

BGK modes are obtained if we require $g(W)$ to satisfy equations (2.4) and (2.5) [3]. That requirement still allows a wide variety of solutions.

Chapter 3

BGK Mode Construction and Filamentation Instability

Our goal is to study the transverse stability of BGK modes. In general, a linear instability is specific to a given BGK mode. We choose a BGK mode that is dynamically selected (at least approximately) by SRS with z being the direction of laser beam propagation in plasma. The simplest nontrivial BGK family of solutions $f_{BGK} = f_{BGK}(z - v_\varphi t, v_z)$ exists in 1D+1V (one space and one velocity dimension [3]). It can be easily extended to 3D+3V space as follows

$$f = f_{BGK}(z - v_\varphi t, v_z)\frac{\exp(-\mathbf{v}_\perp^2/2)}{2\pi}, \tag{3.1}$$

with no dependence on the transverse coordinate $\mathbf{r}_\perp$, while the dependence on the transverse velocity $\mathbf{v}_\perp$ being trivially Maxwellian.

Our initial model [2] of the SRS daughter LW in a laser speckle is presented in Eq. (3.5) below. If a time-dependent Vlasov equation solution has a symmetry, e.g., in 2D+2V when the initial condition (and possible external potential) only depends on one spatial coordinate z, or in 3D+3V a cylindrically symmetric configuration, then an instability may break that symmetry, allowing for a determination of growth rate. The former, revisited here, was explored in 2D+2V Vlasov simulations [31], while the latter was observed [33] in 3D PIC, SRS single speckle simulations. In addition, we present LW filamentation growth rates of linear fluctuations about a particular class of BGK modes, recalled in the next Section 3.1.

3.1 Construction of 1D+1V BGK

The beating of laser and SRS light provides a source of LWs thus pumping BGK modes. Following Ref. [2], we assume that the laser intensity is just above SRS instability threshold. Then the pumping of LWs is slow and can be idealized as a travelling wave sinusoidal external potential Φ^{ext}, with constant amplitude ϕ_{pump}, phase speed v_φ and wavenumber k_z such that

$$\Phi^{ext} = \phi_{pump} \cos[k_z(z - v_\varphi t)], \;\; k_z = |\mathbf{k}|. \tag{3.2}$$

The total electrostatic potential, Φ, is given by Eq. (2.3) while the internal potential Φ^{int} is determined from Poisson's equation (3.3)

$$\frac{\partial^2 \Phi^{int}}{\partial z^2} = 1 - \int f_{1D} dv_z, \tag{3.3}$$

where $f_{1D}(z, v_z, t)$ is the $1D$ electron phase space distribution function.

Inertial confinement fusion applications require a dynamic laser beam smoothing [44, 45, 46] resulting in a time-dependent speckle field of laser intensity. Φ^{ext} attains a local maximum in a laser speckle, which is a local maximum of laser beam intensity. Intense speckles have a width approximately $F\lambda_0$, with F the optic f-number (the ratio of the focal length of the lens divided by the lens diameter) and λ_0 the laser wavelength. The temporal scale t_c of beam smoothing is typically large compared with the inverse growth rate $1/\gamma_{SRS}$ of SRS (e.g. for the National Ignition Facility [45, 46] $t_c \sim$ 4ps and typically $1/\gamma_{SRS} \sim$ 0.03ps). It implies that the speckle can be considered as time-independent which we assume below. Electrons, with the typical speed v_e, cross a speckles width in a dimensional time scale $1/\nu_{SideLoss} \propto F\lambda_0/v_e$. As a result, f_{1D} tends to relax to the background distribution function, f_0, assumed Maxwellian,

$$f_0(v_z) = \frac{\exp(-v_z^2/2)}{\sqrt{2\pi}} \tag{3.4}$$

at the rate $\nu_{SideLoss}$. These considerations motivate our $1D + 1V$ model of BGK generation by introducing the relaxation term $-\nu_{SideLoss}[f_{1D}(z, v_z, t) - f_0(v_z)]$ into the Vlasov equation (2.1) as follows. In the wave frame (switching to that frame implies $z \to z + v_\varphi t$ and $v_z \to v_z + v_\varphi$),

$$\left\{\frac{\partial}{\partial t} + v_z\frac{\partial}{\partial z} - \frac{\partial \Phi}{\partial z}\frac{\partial}{\partial v_z}\right\} f_{1D}(z, v_z, t) = -\nu_{SideLoss}[f_{1D}(z, v_z, t) - f_0(v_z + v_\varphi)]. \tag{3.5}$$

Let f_{eq} be a time independent solution of Eq. (3.5). In the double limit

$$f_{BGK} = \lim_{\phi_{pump}\to 0} \lim_{\nu_{SideLoss}\to 0} f_{eq}, \tag{3.6}$$

a particular BGK mode which bifurcates [47, 48] from a linear LW, f_{BGK}, may be obtained [2]. This mode correspond to the adiabatically slow pumping by SRS. It depends on (z, v_z) only through the single particle energy, W,

$$W = \Phi(z) + \frac{v_z^2}{2} \tag{3.7}$$

which is the restriction of equation (2.7) to $1D + 1V$ case in the wave frame with $\Phi(\mathbf{r}_\perp, z - v_\varphi t) \to \Phi(z)$.

There are two methods to construct BGK modes in question. First method is numerical one and implies that we numerically solve equations (3.2)-(3.5) for each values of ϕ_{pump} and $\nu_{SideLoss}$ followed by taking numerically the double limit (3.6). Second method is analytical one and is based on the integration along the particle orbits of the time independent solution of Eq. (3.5), where the double limit (3.6) is evaluated analytically. We investigated both methods, found that they give similar results, but choose below to focus on the second method only since it is simpler to implement and free of numerical issues.

The electrostatic potential Φ traps electrons with velocities close enough to v_φ such that they cannot go over barriers created by Φ. Thus for different electrons there are both passing orbits outside the trapping region and periodic orbits inside the trapping region. Recall that passing orbits can have either positive or negative velocities, and this must be specified along with W. It was shown in Refs. [49] and [2] that taking the double limit (3.6) in the equation Eq. (3.5) we get

$$f_{BGK}(W) = \frac{1}{T(W)} \oint_W f_0[v(s) + v_\varphi] ds. \tag{3.8}$$

The integral sign here denotes integration around a particular orbit with constant W. The time-like characteristic variable s, used in integration, parametrizes a particular orbital location $(z(s), v(s))$ through the characteristic equations

$$\frac{dz}{ds} = v, \ \frac{dv}{ds} = -\frac{d\Phi}{dz}. \tag{3.9}$$

Also $T(W)$ denotes the orbit's period,

$$T(W) = \oint_W ds. \tag{3.10}$$

Here and throughout the remaining part of Chapter 3 we replace v_z by $v(.)$ when it describes the velocity of a particular electron with energy W as a function of some parameter (s or z), while we think of v_z as independent variable in the rest of the formulas. Also we abuse notation and use the same symbols for v and f_{BGK} irrespective of their parametrization by different variables. Φ is assumed periodic so that all orbits are closed by periodicity (including the passing orbits).

Assume $\Phi(z)$ is the given function of z. Then using Eq. (3.7), changing the integration variable from s to z in Eqs. (3.8) and (3.10), we can express $T(W)$ and $f_{BGK}(z, v_z) \equiv f_{BGK}(W)$ at any point (z, v_z) in the phase space as follows (see Fig.

3.1)

$$T(W) = \begin{cases} 4\int\limits_0^{z_{max}} \frac{dz}{v(z)}, \ \Phi_{min} < W < \Phi_{max}, \\ \int\limits_0^{L_z} \frac{dz}{v(z)}, \ W > \Phi_{max}, \end{cases} \tag{3.11}$$

$$f_{BGK}(W) = \frac{1}{T(W)} \begin{cases} 2\int\limits_0^{z_{max}} \frac{f_0[v_\varphi + v(z)] + f_0[v_\varphi - v(z)]dz}{v(z)}, \ \Phi_{min} < W < \Phi_{max}, \\ \int\limits_0^{L_z} \frac{f_0[v_\varphi + v(z)]dz}{v(z)}, \ W > \Phi_{max} \text{ and } v_z > v_\varphi, \\ \int\limits_0^{L_z} \frac{f_0[v_\varphi - v(z)]dz}{v(z)}, \ W > \Phi_{max} \text{ and } v_z < v_\varphi, \end{cases} \tag{3.12}$$

and $v(z)$ is determined from Eq. (3.7) as

$$v(z) = \sqrt{2[W - \Phi(z)]}, \tag{3.13}$$

with $\Phi_{min} \equiv \min\limits_z \Phi(z)$, $\Phi_{max} \equiv \max\limits_z \Phi(z)$, $L_z \equiv \frac{2\pi}{k_z}$. We assume that $\Phi(z)$ has a single local maximum and a single local minimum per period L_z. Also z_{max} is obtained by numerically inverting $\Phi(z_{max}) = W$ (see Fig. 3.1 for the illustration). Note that it is also possible to integrate Eqs. (3.8) and (3.10) directly in s variable which has more compact form compared to Eqs. (3.11)-(3.12). However, we chose to use Eqs. (3.11)-(3.13) because it is easier to implement a high-order numerical scheme for integrals (3.11) and (3.12) that depend only on one independent variable rather than calculating integrals in Eqs. (3.8)-(3.10) that require two-step process, first numerically finding orbits $(z(s), v(s))$ and then computing the integrals.

The amplitudes of Fourier harmonics of $\Phi(z)$ are rapidly decaying [2], so we start by constructing a BGK mode approximately by taking into account only the first harmonic

$$\Phi(z) = -\phi_0 \cos(k_z z) \tag{3.14}$$

parameterized by the amplitude ϕ_0. Then the comparison with definitions in Eq.

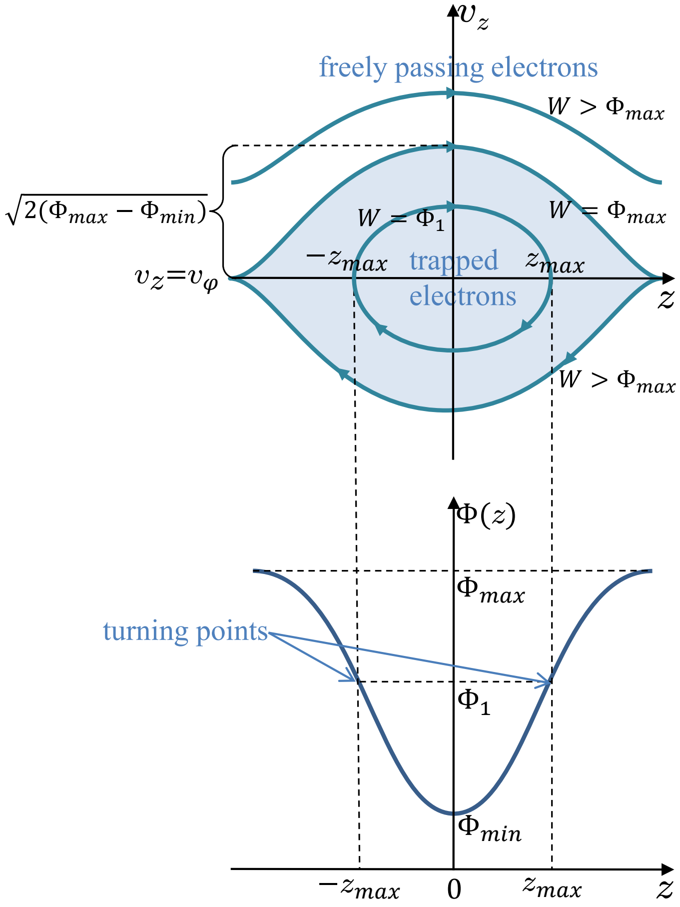

Figure 3.1: Schematics of the electric potential and the corresponding trapping region of $f_{BGK}(z, v_z)$.

(3.13) implies that $\Phi_{min} = -\phi_0$, $\Phi_{max} = \phi_0$, $v(z) = \sqrt{2(W + \phi_0\cos(k_z z))}$ and $z_{max} = \frac{1}{k_z}\arccos(\frac{-W}{\phi_0})$.

Integrating f_{BGK} over v_z that was obtained from Eqs. (3.11)-(3.13) and using the Poisson's equation (3.3), we get the corresponding electrostatic potential $\Phi_{approx}(z)$ of the approximate BGK solution. One can use k_z as the free parameter to rescale the solution in such a way that the amplitude of the first harmonic in the electrostatic potential is equal to ϕ_0 as was assumed in Eq. (3.14).

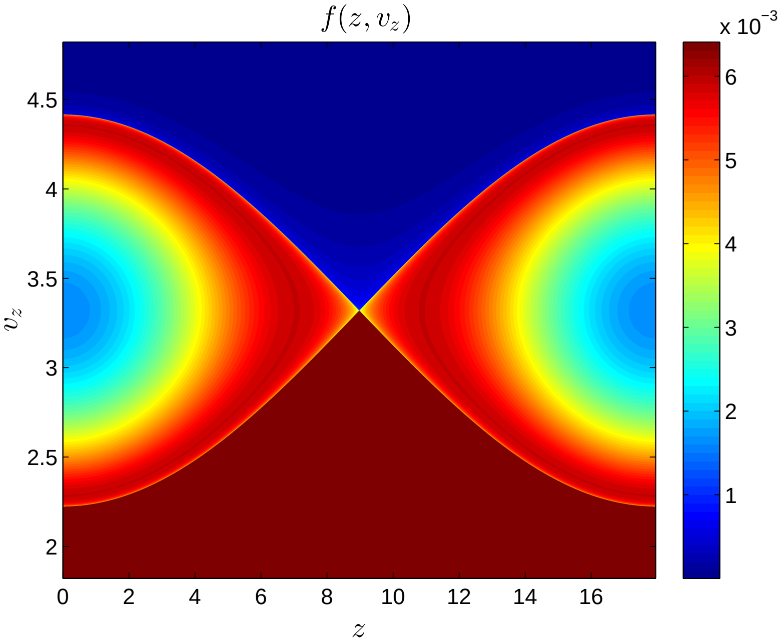

Figure 3.2: The phase space density distribution function $f_{BGK}(z, v_z)$ of BGK mode with $k_z = 0.35, \phi_0 = 0.3, v_\varphi = 3.321836$.

The result is however only approximate because of higher order Fourier harmonics beyond the fundamental one assumed for $\Phi(z)$ in Eq. (3.14). Our calculations show that the second harmonic in $\Phi(z)$ is typically 2-3 orders of magnitude less compared to the first one even for ϕ_0 of order 1, which validates our initial assumption. We found it satisfactory for the purpose of the subsequent results of this work to stop the process of BGK construction at this point. However we also used $\Phi_{approx}(z)$ to obtain the corresponding updated $f_{BGK}(z, v_z)$ from Eqs. (3.11)-(3.13), calculated second iteration of $\Phi_{approx}(z)$, and so on. We found that typically ~ 20 iterations is sufficient to converge $\Phi_{approx}(z)$ within 10^{-15} relative pointwise error over z (with the relative error being $\sim 1\%$ after first iteration) to the exact BGK mode. In this way one can construct a BGK mode for given values of ϕ_0 and v_φ as the input parameters producing the value k_z as the output parameter together with f_{BGK}. If one needs to find f_{BGK} with the specified value of $k_z = k_{z,input}$ then Newton iterations are

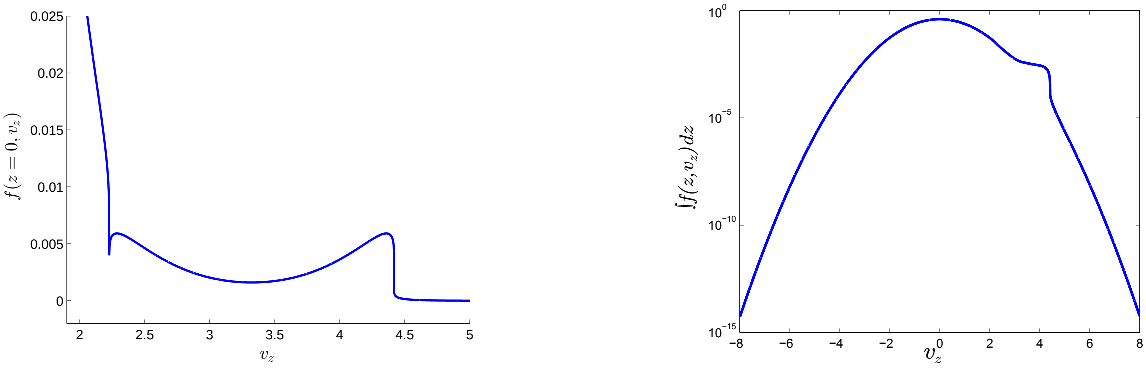

(a) Cross-section of $f_{BGK}(z=0,v_z)$

(b) Averaged density distribution function $\int f_{BGK}(z,v_z)dz/L_z$

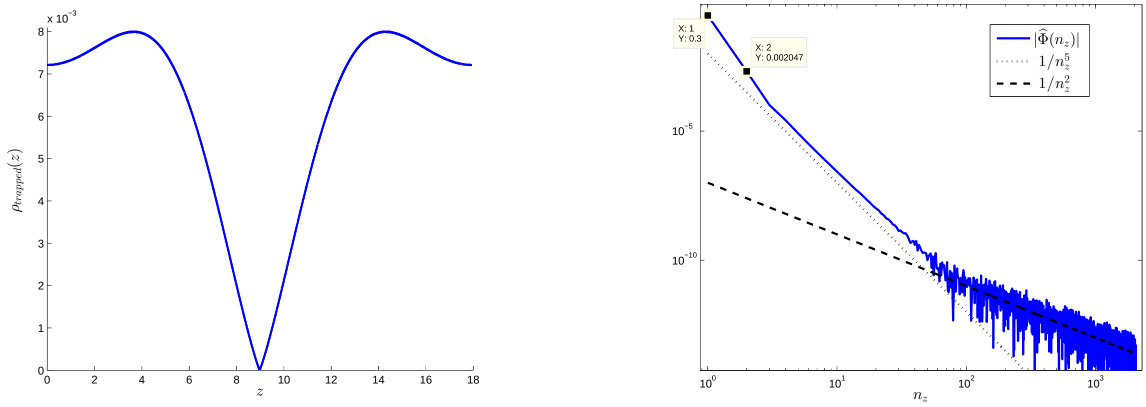

(c) Density of trapped particles $\int_{W<\Phi_{max}} f_{BGK}(z,v_z)dv_z$ as a function of z

(d) Amplitudes of Fourier harmonics of $\Phi(z)$ vs. the harmonic number n_z

Figure 3.3: BGK mode with $k_z = 0.35, \phi_0 = 0.3, v_\varphi = 3.321836$.

performed to find a root of $k_{z,input} - k_{z,output}(\phi_0, v_\varphi) = 0$ as a function of either ϕ_0 or v_φ keeping the other variable fixed. Here $k_{z,output}(\phi_0, v_\varphi)$ is the value of k_z obtained for given ϕ_0 and v_φ from the procedure described above.

An example of BGK mode constructed using this approach with Newton iterations over v_φ for $k_{z,input} = k_z = 0.35,\ \phi_0 = 0.3$ and resulting $v_\varphi = 3.321836\ldots$ is shown in Figs. 3.2-3.3. Fig. 3.2 shows $f_{BGK}(z,v_z)$ around the trapping region with a separatrix $\Phi(z) + v_z^2/2 = W = \Phi_{max}$. Fig. 3.3 shows: (a) the widest cross-section of the trapping region at $z = 0$, (b) the phase space distribution function averaged in z-direction as $\int f_{BGK}(z, v_z)dz/L_z$, (c) the density of trapped particles as a function of z, (d) the spectrum of electrostatic potential $\Phi(z)$ with the second harmonic being more than two orders of magnitude less than the first one.

3.2 BGK Dispersion Relation and Nonlinear Frequency Shift

The dispersion relation of the particular family of BGK modes in question has been presented in Refs. [2] and [4]. Unlike the linear regime, in which the parameters k_z and v_φ are related via well-known amplitude-independent dispersion relations [50, 51], a BGK mode's dispersion relation is ϕ_{eq} dependent. The BGK mode identified by Eqs. (3.5) and (3.6) is undamped and has a nonlinear dispersion relation determined [47, 48] by setting the real part of the dielectric function, ε, to zero. Recall that we define the nonlinear dielectric function ε as $\Phi = \Phi^{ext}/\varepsilon$ with Φ^{ext} being the external pump from SRS, Eq. (3.2). To lowest order in $\sqrt{\phi_{eq}}$ using f_{BGK} given by Eqs. (3.11)-(3.14) one obtains [2] that,

$$0 = \mathrm{Re}[\varepsilon] \approx \mathrm{Re}[\varepsilon_0] + 1.76 f_0''(v_\varphi)\frac{\sqrt{\phi_{eq}}}{k_z^2}, \tag{3.15}$$

where

$$\varepsilon_0(k_z, \omega) = 1 - \frac{\Xi_0(v_\varphi)}{k_z^2}, \tag{3.16}$$

$$\begin{aligned} \Xi_0(v) &= Z'(v/\sqrt{2})/2, \\ Z(v) &= e^{-v^2}\sqrt{\pi}(i - \mathrm{erfi}(v)) = e^{-v^2}(i\sqrt{\pi} - 2\int_0^v e^{t^2}dt), \end{aligned} \tag{3.17}$$

Z is the plasma dispersion function [52] and ε_0 is the linear dielectric function.

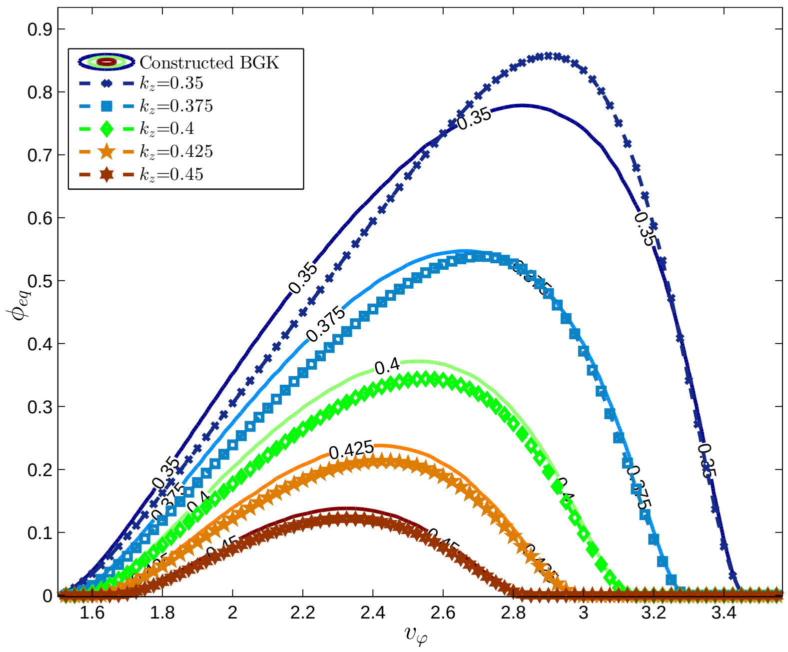

Figure 3.4: LW and EAW potential amplitude versus phase velocity for various k_z. Solid lines represent constructed BGK family dispersion relation, dashed - approximation of dispersion relation by formula (3.15).

Eq. (3.15) can be solved for $\phi_{eq}(k_z, v_\varphi)$. These solutions are illustrated in Fig. 3.4 by dashed lines with markers for various values of k_z together with solid lines corresponding to the BGK modes that were constructed numerically following the procedure in 3.1 with the same values of k_z and v_φ. For $k_z = 0.35$ the maximum amplitude of the constructed BGK is $\phi_{eq} \approx 0.78$ at $v_\varphi \approx 2.85$ while Eq. (3.15) overestimates the maximum ϕ_{eq} at 0.85. The correspondence of solutions of Eq. (3.15) and values of v_φ for the constructed BGKs for small ϕ_{eq} is quite good. For each k_z and ϕ_{eq} less than the maximum amplitude, we have two solutions for v_φ, the larger value corresponding to the nonlinear LW wave and the smaller one corresponding to the electron acoustic [53] wave (EAW), similar to two solutions of the Vlasov dispersion relation $\mathrm{Re}[\varepsilon_0(k_z, \omega)] = 0$ for a given k_z (see Fig. 2 in Ref. [54]). BGKs for $k_z > 0.53$ don't exist.

Alternatively, v_φ may be considered as a function of k_z and ϕ_{eq}, i.e. $v_\varphi(k_z, \phi_{eq})$, by inverting the graph shown in Fig. 3.4. Since a travelling wave's frequency, ω, is always the product of wavenumber and phase velocity, $\omega = k_z v_\varphi$, one may re-express the nonlinear dispersion relation as a wavenumber and amplitude dependent ω,

$$\omega(k_z, \phi_{eq}) = k_z v_\varphi(k_z, \phi_{eq}). \tag{3.18}$$

We define the nonlinear frequency shift as

$$\Delta\omega^{BGK} = \omega(k_z, \phi_{eq}) - \omega_0, \tag{3.19}$$

where $\omega_0 = \omega(k_z, \phi_{eq} \to 0)$. For $k_z = 0.35$, $\omega_0 = 1.21167$.

Expanding $\mathrm{Re}[\varepsilon_0(k_z, \omega)]$ in Eq. (3.15) in a Taylor series at $\omega = \omega_0$, taking into account that $\mathrm{Re}[\varepsilon_0(k_z, \omega_0)] = 0$, we get an approximation of $\Delta\omega^{BGK}$ given by

$$\Delta\omega_{NL}^{Rose} = -1.76 \left[\frac{\partial \mathrm{Re}[\varepsilon_0(\omega_0)]}{\partial\omega}\right]^{-1} f_0''(v_\varphi)\frac{\sqrt{\phi_{eq}}}{k_z^2}, \tag{3.20}$$

as presented in Eq. (50) of Ref. [2] and Eq. (9) and Fig. 5 of Ref. [4]. For $k_z = 0.35$, $\frac{\partial \mathrm{Re}[\varepsilon_0(\omega_0)]}{\partial\omega} = 2.335$.

In earlier works of Morales and O'Neil [24] and Dewar [21] an approximation for the nonlinear frequency shift of large-amplitude EPW was derived

$$\Delta\omega_{NL}^{Dewar} = -\alpha \left[\frac{\partial \mathrm{Re}[\varepsilon_0(\omega_0)]}{\partial\omega}\right]^{-1} f_0''(v_\varphi)\frac{\sqrt{\phi_{eq}}}{k_z^2}, \tag{3.21}$$

where $\alpha = 0.77\sqrt{2} = 1.089$ and $\alpha = 1.163\sqrt{2} = 1.645$ for the "adiabatic" and "sudden" excitation of nonlinear LW, respectively. The derivation was also summarized in Ref. [55] and used in Ref. [31]. In Ref. [2] after Eq. (48) H. Rose discusses the source of the discrepancy between 1.76 coefficient in Eq. (3.20) and 1.645 for "sudden" excitation in Eq. (3.21).

3.3 Filamentation Instability of BGK modes

LW filamentation instability theory has been presented in Refs. [4] and [31], but we believe that a more cogent and general result was obtained in Ref. [29], which we now review.

Let x denote a direction perpendicular to the LW propagation direction, the z axis, with wave amplitude ϕ_{eq}, the maximum value of $\Phi(z)$ over z (in particular case given by Eq. (3.14), $\phi_{eq} = \phi_0$). Near the equilibrium (BGK mode) in the moving frame, let

$$\Phi = \mathrm{Re}\left\{\exp(i\mathbf{k}\cdot\mathbf{r})[\phi_{eq} + \delta\phi(t)\exp(i\delta\mathbf{k}\cdot\mathbf{r})]\right\}, \tag{3.22}$$

where $\mathbf{k}$ is parallel to z direction and $\delta\mathbf{k}$ is responsible for the transverse perturbations with the amplitude $\delta\phi(t)$. Let $\delta\phi \sim \exp(\gamma t)$. In Ref. [29] it was shown that

$$(\gamma + \nu_{residual})^2 = -D\left(\phi_{eq}\frac{\partial\omega}{\partial\phi_{eq}} + D\right), \tag{3.23}$$

wherein the generalized diffraction operator, D,

$$2D = \omega(|\mathbf{k}+\delta\mathbf{k}|, \phi_{eq}) + \omega(|\mathbf{k}-\delta\mathbf{k}|, \phi_{eq}) - 2\omega(|\mathbf{k}|, \phi_{eq}) \tag{3.24}$$

reduces to the diffraction coefficient, $\frac{|\delta\mathbf{k}_\perp|^2}{2|\mathbf{k}|}\frac{\partial\omega}{\partial|\mathbf{k}|} + \frac{\delta k_z^2}{2}\frac{\partial^2\omega}{\partial|\mathbf{k}|^2}$, for small $|\delta\mathbf{k}|$.

When $\delta\mathbf{k}\cdot\mathbf{k} = 0$, Eq. (3.24) simplifies to

$$D = \omega(|\mathbf{k}+\delta\mathbf{k}|, \phi_{eq}) - \omega(|\mathbf{k}|, \phi_{eq}), \tag{3.25}$$

and the (possible) instability is customarily called filamentation, our main regime of interest.

Also assuming $\phi_{eq} \ll 1$ in addition to $\delta\mathbf{k}\cdot\mathbf{k} = 0$ and $|\delta\mathbf{k}| \ll 1$, we can approximate Eq. (3.25) as follows

$$D \approx D_{lin} = \frac{v_g}{2k_z}|\delta\mathbf{k}|^2, \quad v_g \equiv \left.\frac{\partial\omega(|\mathbf{k}|, 0)}{\partial|\mathbf{k}|}\right|_{|\mathbf{k}|=k_z}, \tag{3.26}$$

where v_g is the group velocity corresponding to the dispersion relation (3.15) at $\phi_{eq} = 0$, $v_g = 1.008$ for $k_z = 0.35$.

The residual damping, $\nu_{residual}$, from Eq. (3.23) is model dependent. For example, if the double limit of Eq. (3.6) stops short of zero value, but with

$$\frac{\nu_{residual}}{\omega_{bounce}} \ll 1, \ \frac{\phi_{pump}}{\phi_{eq}} \ll 1, \ \frac{\omega_{bounce}}{\omega_{pe}} = k_z\sqrt{\phi_{eq}}, \tag{3.27}$$

or in dimensional units, $\frac{\omega_{bounce}}{\omega_{pe}} = k_z\lambda_D\sqrt{e\phi_{eq}/k_BT_e}$. Then it follows from Eqs. (28), (71) of Ref. [2] and Fig. 3 of Ref. [2] that, for $v_\varphi \gtrsim 2.2$, in dimensional units,

$$\nu_{residual} \approx \frac{\omega_{pe}}{2}\mathrm{Im}[\varepsilon] \gtrsim \frac{\nu_{SideLoss}}{\omega_{bounce}}\nu_{Landau}. \tag{3.28}$$

In Eq. (3.28), the Landau damping rate, ν_{Landau}, is evaluated for a linear LW with wavenumber k_z. Also if $|\delta\mathbf{k}| \ll |\mathbf{k}|$ is not satisfied, it has been argued [31] that $\nu_{residual}$ is augmented by an amplitude dependent, but $\nu_{SideLoss}$ independent, form of Landau damping. However, as we discuss in Section 4.2 below, that addition to $\nu_{residual}$ is not consistent with our simulation results and we set $\nu_{residual} = 0$.

Eq. (3.18) may be used to find $\frac{\partial\omega}{\partial\phi_{eq}}$ in terms of $\frac{\partial v_\varphi}{\partial\phi_{eq}}$ which in turn may be obtained by applying $\frac{\partial}{\partial\phi_{eq}}$ to Eq. (3.15)

$$\{Re[\Xi_0'(v_\varphi)] - 1.76f_0'''\sqrt{\phi_{eq}}\}\frac{\partial v_\varphi}{\partial\phi_{eq}} = \frac{1.76f_0''(v_\varphi)}{2\sqrt{\phi_{eq}}}. \tag{3.29}$$

In the kinetic regime, D may assume negative values as $|\delta\mathbf{k}|$ [4] and/or ϕ_{eq} [29] increase. Therefore, the qualitative shape of γ contours determined by Eqs. (3.15), (3.23) and (3.24) may differ from fluid model modulational/filamentation [31], whose domain of applicability is limited, a priori, to $k_z \ll 1$. Contours of γ for $k_z = 0.35$ are shown in Fig. 3.5(a), with $\nu_{residual}$ set to 0. For more contours of γ and related figures see [29]. If we use linear approximation for D as in Eq. (3.26) and solve Eqs. (3.15), (3.23) for $k_z = 0.35$ and $\nu_{residual} = 0$ we get contours of γ as shown in Fig. 3.5(b). As k_z is increased, the range of amplitudes over which Eqs. (3.15), (3.23) and

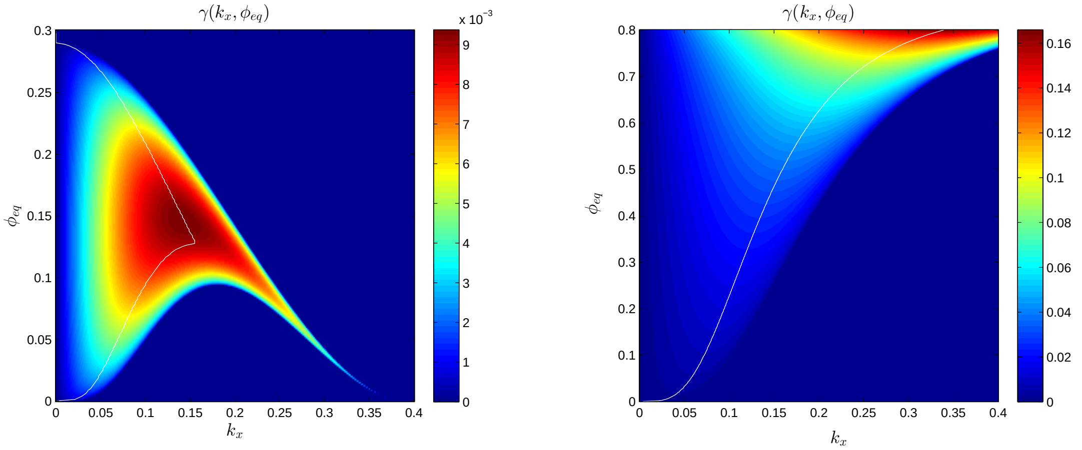

(a) Growth rates using D as in Eq. (3.25)

(b) Growth rates using linear approximation for D as in Eq. (3.26)

Figure 3.5: Theoretical LW filamentation growth rate contours for $k_z = 0.35$. White lines shows the maximum growth rate for given ϕ_{eq}.

(3.24) predict growth is reduced, while using D_{lin} from Eq. (3.26) provides growth in a full range of amplitudes for any k_z. The latter case in more consistent with the simulations as we will see in Chapter 4.

Another simplification can be made if one assumes at the leading order that the nonlinear frequency shift $\Delta\omega \propto \sqrt{\phi_{eq}}$. Then $\phi_{eq}\frac{\partial\omega}{\partial\phi_{eq}} = \frac{\Delta\omega}{2}$ and maximizing γ over D in Eq. (3.23) we obtain the maximum value

$$\gamma^{max} = \frac{|\Delta\omega|}{4}, \tag{3.30}$$

at

$$D = -\frac{\Delta\omega}{4}, \tag{3.31}$$

which is valid for $|\delta\mathbf{k}| \ll |\mathbf{k}|$ and $\nu_{residual} = 0$. Using the approximation (3.26), we obtain from Eq. (3.31) the position of the maximum

$$|\delta\mathbf{k}| = k_x^{max} = \left(\frac{-\Delta\omega\, k_z}{2v_g}\right)^{1/2}. \tag{3.32}$$

Chapter 4

Numerical Simulations of BGK mode Filamentation

Here we describe 2D+2V fully nonlinear Vlasov simulations that we performed to study the filamentation instability of BGK modes described in the previous Chapter.

4.1 Simulation Settings and Methods

We simulate 2D+2V Vlasov-Poisson system (2.1)-(2.5) in phase space, (z, v_z, x, v_x), using fully spectral (in all four dimensions) code and 2nd order in time split-step (operator splitting) method with periodic boundary conditions (BC) in all four dimensions. To ensure spectral convergence and imitate the weak effect of collisions, we added to Eq. (2.1) a small hyper-viscosity term as follows

$$\left\{\frac{\partial}{\partial t}+v_z\frac{\partial}{\partial z}+v_x\frac{\partial}{\partial x}+E_z\frac{\partial}{\partial v_z}+E_x\frac{\partial}{\partial v_x}\right\}f(z,v_z,x,v_x,t)=\\ -D_{16v_z}\frac{\partial^{16}}{\partial v_z^{16}}\left(f-\frac{1}{L_z}\int_0^{L_z}f dz\right), \tag{4.1}$$

where D_{16v_z} is the 16th order hyper-viscosity coefficient. We use periodic BC in z direction with period $L_z = 2\pi/k_z$ and $k_z = 0.35$ in our simulations. Choosing $L_z = 2\pi/k_z$ allows us to focus on the study of filamentation instability effects (along x) while avoiding subharmonic (sideband) instability [56] in the longitudinal z-direction. Periodic BC in x with the period L_x together with x-independent initial condition (IC) are used to separate filamentation instability effects from any sideloss effects due to trapped electrons traveling in the transverse direction (this is in contrast to Ref. [7], where the transverse spatial profile in the initial condition made sideloss comparable with filamentation instability growth rate). We chose typically $200\pi \leq L_x \leq 800\pi$ depending on the BGK mode's amplitude to capture all growing transverse modes. Periodic BC in v_z and v_x were used without sacrificing any accuracy of the simulation compared to outgoing BC since the particle flow through the boundary at $v_z = v_z^{max}$ is $\propto E_z\frac{\partial f}{\partial v_z}$ with $\frac{\partial f}{\partial v_z} \approx \frac{v_z}{\sqrt{2\pi}}e^{-\frac{v_z^2}{2}}$ which can be made as small as desired by picking large enough v_z^{max}. Typically we choose $v_z^{max} = 8$ for which $|E_z\frac{\partial f}{\partial v_z}| \approx 10^{-15}$. The same argument is applied in v_x direction with the only difference that in our simulations E_x is several orders less than E_z so v_x^{max} can be chosen smaller than v_z^{max}. Typically we choose $v_x^{max} = 6$ for which the flow through $v_x = v_x^{max}$ boundary is at the level of machine precision as well.

Split-step method of 2nd order was chosen over other methods since it is unconditionally stable (which allows large time steps), preserves number of particles at each time step exactly and produces small error in the full energy of the system. That error is not accumulated over time (in contrast with Runge-Kutta methods where such accumulation occurs). We also decided to choose 2nd order method over higher order methods because our experiments with the size of time step and methods of various orders showed that the time integration error is dominated by the errors coming from other sources (space discretization and hyper-viscosity smoothing). See more detail on the numerical method in Appendix A.

The hyper-viscosity term in the right-hand side (r.h.s.) of Eq. (4.1) is used to prevent recurrence [57] and aliasing (which causes propagation of numerical error from high modes to low modes) effects. The hyper-viscosity operator in r.h.s. of Eq. (4.1) has to be a smooth function in the Fourier transformed v_z space. At the same time we found it beneficial to use high-order (here we choose 16th order) over low-order hyper-viscosity since it affects low modes of solution less while having effectively the same damping effect on high modes. That allowed us to use a smaller numerical grid for the same overall precision. The coefficient D_{16v_z} is chosen as small as possible to prevent aliasing depending on the resolution of simulation in v_z directions. Our safe estimate $D_{16v_z} \approx |\gamma_{Landau}(k_z)|(\frac{2\Delta v_z}{\pi})^{16}$ with $\gamma_{Landau}(k_z = 0.35) = -0.034318\ldots$ found to be sufficient to avoid aliasing issues and completely remove the recurrence effect [57] in linear Landau damping simulations (while still recovering proper Landau damping with any desired accuracy for simulations with small-amplitude waves). Simulations with large amplitude waves (with $\Phi \sim 1$) might require higher value of hyper-viscosity coefficient D_{16v_z}, so one needs to keep track of spectrum of the solution in (z, v_z) space and adjust D_{16v_z} if needed. We typically used $D_{16v_z} = 10^{-25}$ for simulations with $N_z \times N_{v_z} = 64 \times 256$ grid points in (z, v_z) space and $D_{16v_z} = 10^{-30}$ for $N_z \times N_{v_z} = 128 \times 512$. Also hyper-viscosity does not affect conservation of number of particles in the system while having positive effect on conservation of energy in long-term simulations. While the term $-\frac{1}{L_z}\int_0^{L_z} f dz$ in r.h.s. side of (4.1) is not absolutely necessary, we found that the total energy of the system is conserved better if this term is included. This is because this term prevents filtering out of the 0th harmonic of f in z-space that holds most of the kinetic energy. We did not need any hyper-viscosity in v_x direction since the electrostatic field (and therefore both perturbations of electron density and amount of energy in high modes) in transverse direction is many orders of magnitude weaker compared to the longitudinal direction (z, v_z) throughout most of the simulation until nonlinear self-focusing event at the end. Detailed simulation of that event is however outside of the scope of this work.

All simulations are carried out in the lab frame rather then in moving frame, since in this case the tails of the distribution function in v_z direction are almost symmetric and have smaller values $\propto \exp(-(v_z^{max})^2/2)$ at the boundaries $\pm v_z^{max}$ compared to the tail value $\propto \exp(-(v_z^{max} - v_\varphi)^2/2)$ in simulations done in the wave frame moving with velocity v_φ with the same v_z^{max}. For this reason simulations performed in the lab frame have smaller numerical error due to periodic BC in v_z.

4.2 2D+2V Simulations and Filamentation Instability of 1D BGK Modes

In these simulations we use IC of the form of Eq. (3.1) that has the constructed BGK mode from Section 3.1 in the (z, v_z) directions, uniform in the x-direction and a Maxwellian distribution $f_0(v_x)$ in the v_x direction,

$$f(z, v_z, x, v_x, t = 0) = f_{BGK}(z, v_z) f_0(v_x). \tag{4.2}$$

We run simulations for a long enough time to observe the growth of oblique harmonics of electric field with wave vectors $(k_z = 0.35, k_x)$ (see Fig. 4.1 for a quarter of $E_z(z, x)$ spectrum, other quarters of the spectrum are similar to it) for several orders in magnitude (see Fig. 4.2), where k_z is the wavenumber corresponding to the BGK mode and k_x varies between $-k_x^{max}$ and $k_x^{max} = \pi/\Delta x$, $\Delta x = L_x/N_x$, where N_x is the number of grid points in x. The initial values in these harmonics are near the machine precision from the round-off errors. During the simulation they grow from values $\sim 10^{-16}$ to $\sim 10^{-1}$. The exponential growth rates γ_{k_x} for these harmonics are extracted (see Fig. 4.3) from the least-square fit when the amplitudes grow from $\sim 10^{-13}$ to

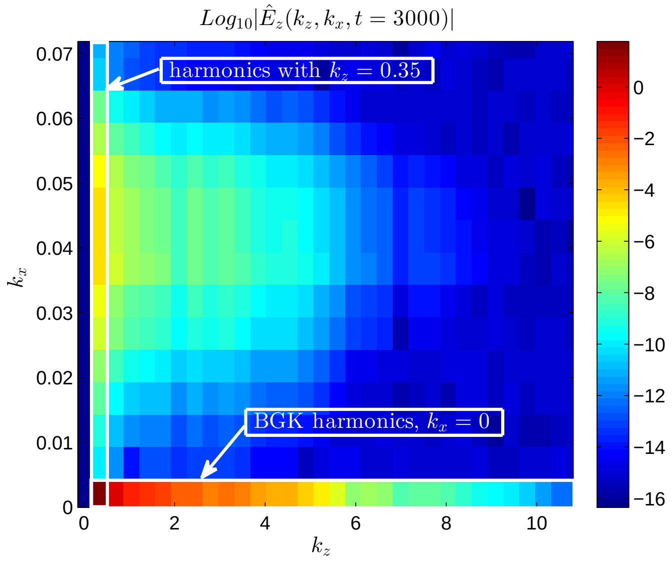

Figure 4.1: The density plot of the spectrum of $E_z(z, x)$ at $t = 3000$.

$\sim 10^{-8} - 10^{-6}$ (during these times a clear exponential growth $\propto e^{\gamma_{k_x} t}$ is observed). Later in the simulation, nonlinear self-focusing effects come into play and LW filamentation occurs (see Figs. 4.4 and 4.5) transferring a significant part of electric field energy, $\mathrm{P}(t)=\iint \frac{|E_z|^2+|E_x|^2}{2} dzdx$, into kinetic energy, $\mathrm{K}(t)=\int\!\!\int\!\!\int\!\!\int \frac{(v_z^2+v_x^2)}{2} f dzdxdv_zdv_x$ (see Fig. 4.6). Notice also that the relative error in full energy of the system, $\mathrm{Energy}(t)=\mathrm{P}(t)+\mathrm{K}(t)$, is small. Figs. 4.1-4.6 are obtained from the simulation with $\phi_{eq} = 0.2$. Other simulation parameters were $D_{16v_z} = 10^{-25}$, $64 \times 256 \times 64 \times 32$ grid points for (z, v_z, x, v_x) with $L_z = 2\pi/k_z, L_x = 400\pi, v_z^{max} = 8, v_x^{max} = 6$, the time step $\Delta t = 0.1$ and the final simulation time $T_{final} = 5000$. Simulations with a larger L_x and correspondingly larger extent of spectrum in k_x were done too but no other regions of growing modes in spectrum (such as in Figs. 4.1 and 4.3) were observed except for the one starting near $k_x = 0$.

These simulations were done for a variety of BGK modes with $k_z = 0.35$, amplitudes $0.025 \leq \phi_{eq} \leq 0.77$ and values of v_φ according to the BGK dispersion relation (3.15). The parameters of these simulation were $D_{16v_z} = 10^{-25}, 64\times256\times32\times32$ grid

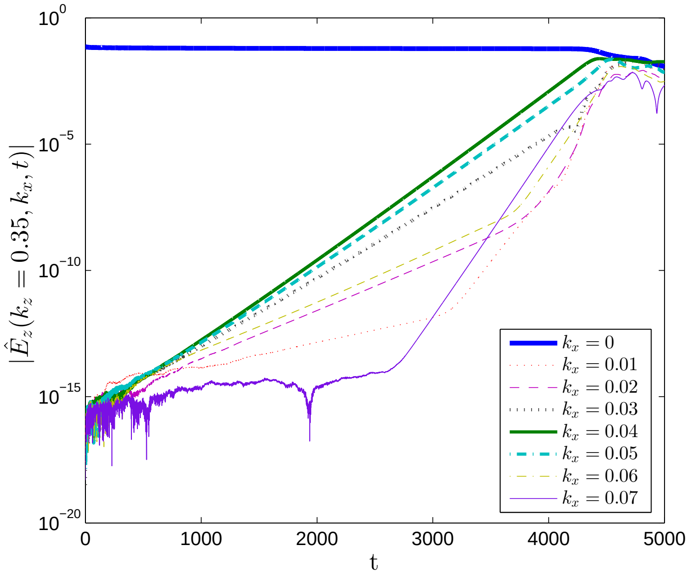

Figure 4.2: The growth of harmonics $|\hat{E}_z(k_z = 0.35, k_x, t)|$ in time.

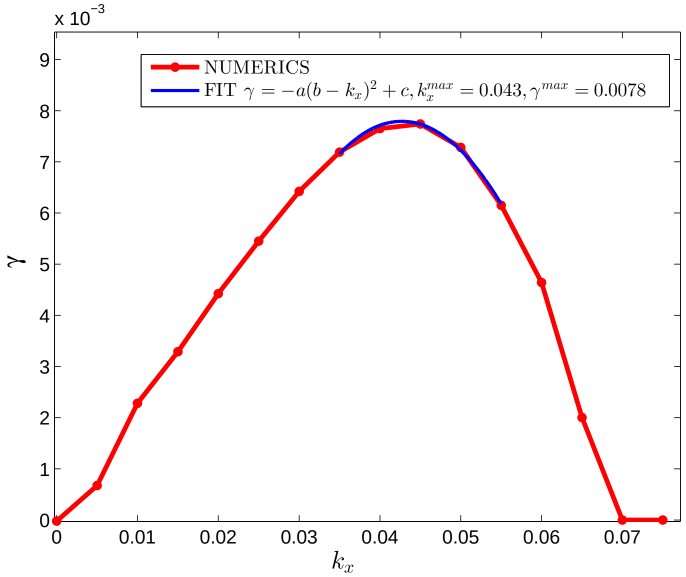

Figure 4.3: The growth rates γ_{k_x} of oblique harmonics extracted from the least-square fit to the data of Fig. 4.2. A fit to the quadratic law near the maximum is also shown.

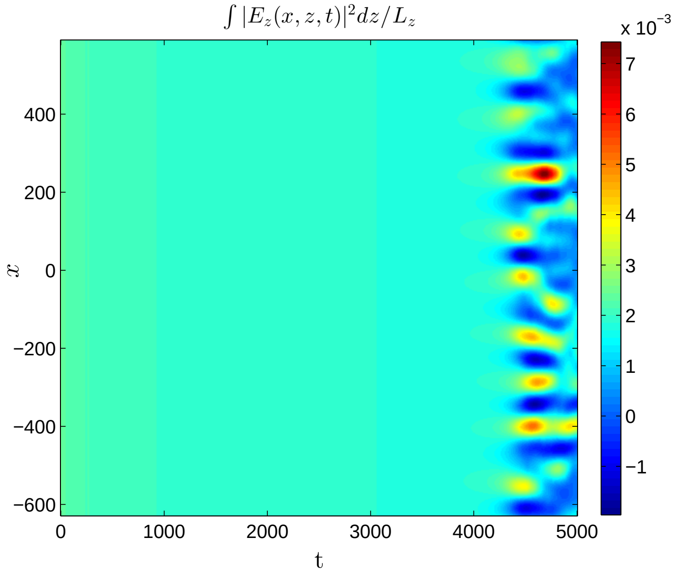

Figure 4.4: The density plot vs. x and t for $\langle |E_z|^2 \rangle_z \equiv L_z^{-1} \int_0^{L_z} |E_z|^2 dz$ ($|E_z|^2$ averaged over z) shows a development of LW filamentation with time from the initial BGK mode.

points for $(z, v_z, x, v_x), \Delta t = 0.1$ and $2000 \leq T_{final} \leq 30000$ depending on BGK amplitude (see Table 4.1). Another set of simulations was performed for $D_{16v_z} = 10^{-30}$ and $128 \times 512 \times 32 \times 32$ grid points with the rest of parameters being the same (see Table 4.2) to confirm smallness of discretization errors. Value ϕ_0 in Tables 4.1 and 4.2 indicate initial BGK amplitude with witch it was produced according to the recipe in Section 3.1 while ϕ_{eq} indicates an average amplitude the BGK had throughout long-term evolution of the system. ϕ_{eq} is smaller than initial ϕ_0 due to numerical effect, while the gap between them is reduced for higher resolution in (z, v_z) directions (compare Table 4.2 to Table 4.1).

We extract the nonlinear frequency shift $\Delta\omega^{NUM}$ from simulations by finding the wave frequency as the rate of change of the phase of the Fourier harmonic of Φ with $k_z = 0.35$, $k_x = 0$ and subtracting the frequency that corresponds to our undamped BGK mode in the limit of zero amplitude, $\omega_0 = \omega(k_z = 0.35, \phi_{eq} = 0) =$

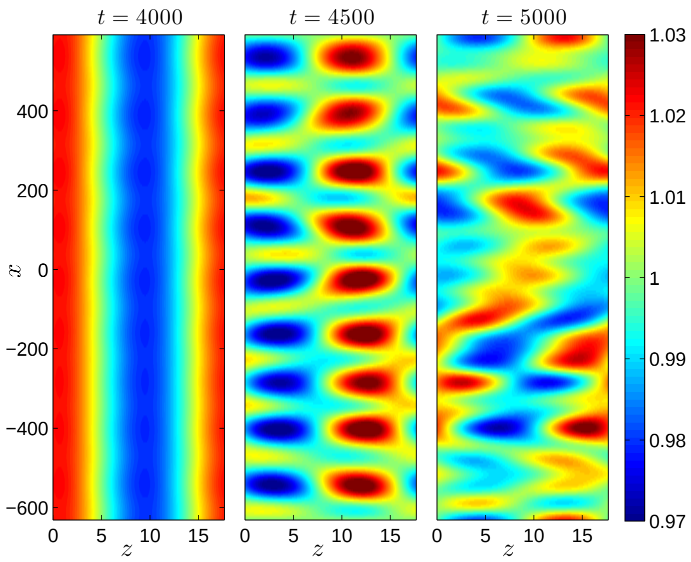

Figure 4.5: Modulation of particle density $\rho(z, x)$ before ($t = 4000$), during ($t = 4500$) and after ($t = 5000$) Langmuir wave filamentation.

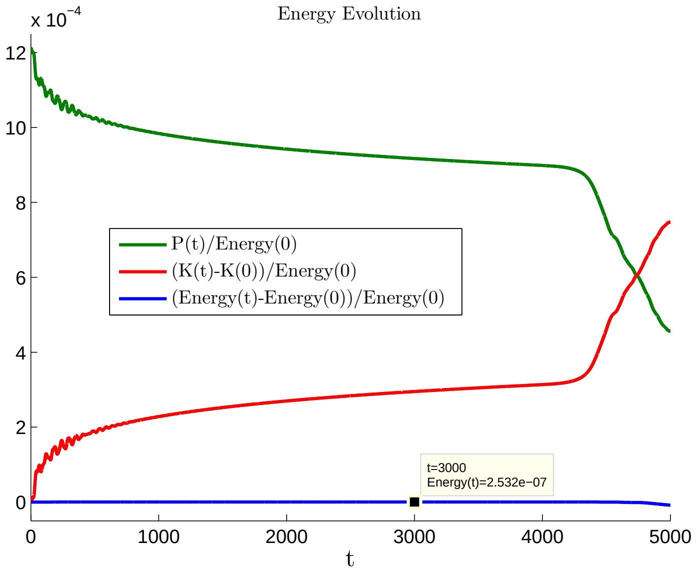

Figure 4.6: Evolution of electrostatic, P(t), kinetic, K(t), and total energy, Energy(t), in the simulation with BGK amplitude ϕ_{eq}=0.2.

Table 4.1: Parameters of 2D+2V BGK simulations with $k_z = 0.35, L_z = 2\pi/k_z, \Delta t = 0.1,$ $v_z^{max} = 8, v_x^{max} = 6, D_{16v_z} = 10^{-25},$ $N_z = 64, N_{v_x} = 256, N_x = 32, N_{v_x} = 32.$

ϕ_0	ϕ_{eq}	v_φ	T_{final}	L_x
0.025	0.014	3.4340	25000	800π
0.05	0.035	3.4185	20000	400π
0.075	0.058	3.4062	15000	400π
0.1	0.082	3.3941	10000	400π
0.2	0.177	3.3582	5000	400π
0.3	0.274	3.3229	4000	200π
0.4	0.359	3.2809	3000	200π
0.5	0.454	3.2327	3000	200π
0.6	0.542	3.1676	3000	200π
0.7	0.627	3.0719	1500	200π
0.77	0.703	2.9123	1500	200π

Table 4.2: Parameters of 2D+2V BGK simulations with $k_z = 0.35, L_z = 2\pi/k_z, \Delta t = 0.1,$ $v_z^{max} = 8, v_x^{max} = 6, D_{16v_z} = 10^{-30},$ $N_z = 128, N_{v_x} = 512, N_x = 32, N_{v_x} = 32.$

ϕ_0	ϕ_{eq}	v_φ	T_{final}	L_x
0.025	0.020	3.4327	25000	400π
0.05	0.043	3.4168	20000	400π
0.075	0.067	3.4056	15000	400π
0.1	0.093	3.3959	10000	400π
0.2	0.190	3.3585	5000	400π
0.3	0.287	3.3217	4000	200π
0.4	0.379	3.2803	3000	200π
0.5	0.476	3.2315	3000	200π
0.6	0.574	3.1667	3000	200π
0.7	0.668	3.0681	1500	200π
0.77	0.721	2.9108	1500	200π

$1.2116687\ldots$, which can be found as a real root of $\mathrm{Re}[\varepsilon_0(k_z,\omega)] = 0$ or Eq. (3.15) with $\phi_{eq} = 0$. Note that the frequency of the damped linear LW (real part of a complex root of $\varepsilon_0(k_z,\omega) = 0$ [18, 19]) is $\omega_{LW}(k_z = 0.35) = 1.22095\ldots$, for the discussion of Vlasov vs. Landau analysis see Ref. [48]. The difference is $\approx 1\%$ for $k_z = 0.35$ and it becomes larger for larger k_z. Fig. 4.7 shows $\Delta\omega^{NUM}$ (large blue circles) obtained from simulations in comparison with theoretical one $\Delta\omega^{BGK}$ (solid black line) computed using Eq. (3.19), approximations $\Delta\omega_{NL}^{Rose}$ (dashed black line with circle markers) and $\Delta\omega^{Dewar}$ (dashed red line with small "o" markers and pink line with "x" markers) given by Eqs. (3.20) and (3.21), respectively, for which we used $v_\varphi = \omega^{NUM}/k_z$. We conclude from Fig. 4.7 that both $\Delta\omega_{NL}^{Rose}$ and $\Delta\omega^{Dewar}$ with $\alpha = 1.645$ (sudden) work really well for the whole range of amplitudes whereas $\Delta\omega^{BGK}$ works well for amplitudes of BGK $\phi_{eq} \lesssim 0.5$ since v_φ for $\phi_{eq} > 0.5$ deviates from the solution of approximate dispersion relation Eq. (3.15) as can be seen in Fig. 3.4.

Growth rates of filamentation instability as a function of k_x from the series of

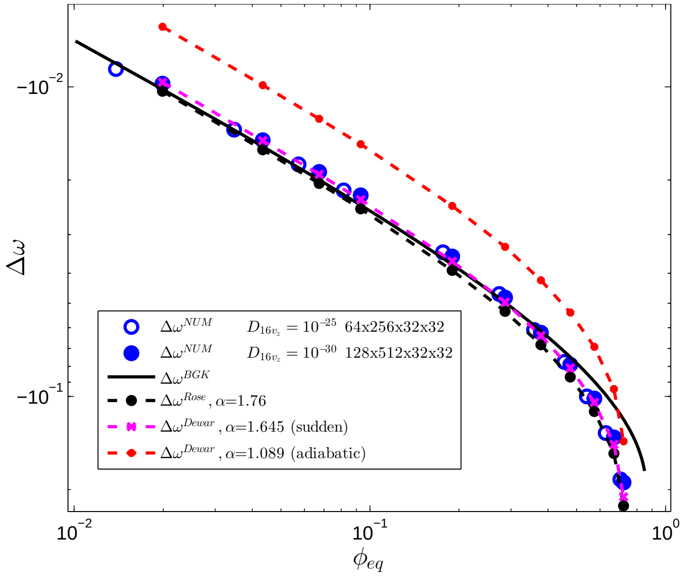

Figure 4.7: Nonlinear frequency shift as a function of BGK amplitude ϕ_{eq}.

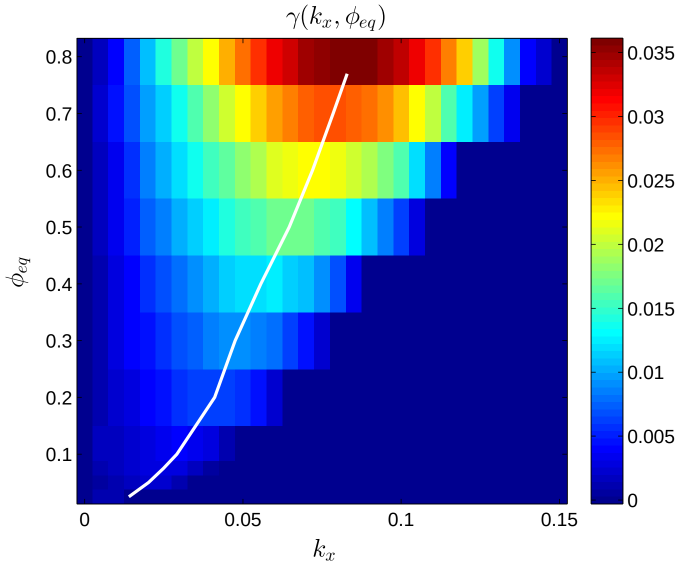

Figure 4.8: Numerical growth rates γ density plot as a function of k_x and BGK amplitude ϕ_{eq}. The white line shows the position of the maximum γ_{k_x} for each ϕ_{eq}.

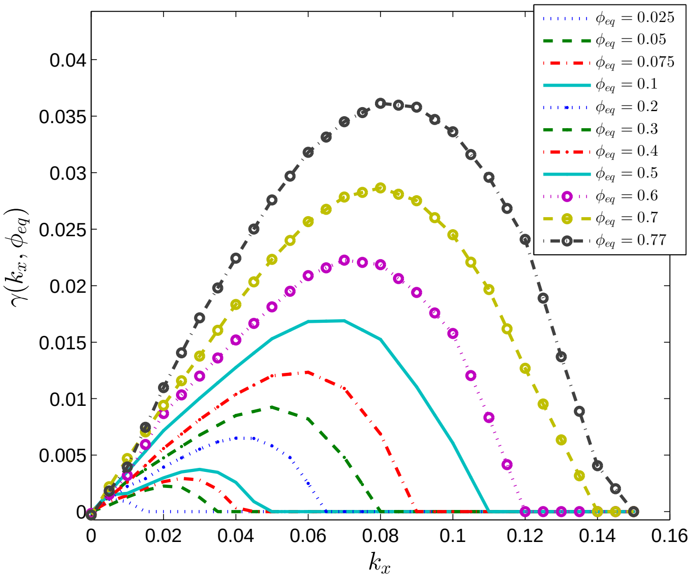

Figure 4.9: The growth rates γ_{k_x} as a function of k_x for BGK modes with various amplitudes ϕ_{eq} correspond to multiple cross-sections of Fig. 4.8.

simulations with $D_{16v_z} = 10^{-30}$ and various amplitudes ϕ_{eq} are given in Figs. 4.8 and 4.9. The maximum growth rate γ^{max} (the maximum vs. k_x for each fixed ϕ_{eq}) as a function of ϕ_{eq} is shown in Fig. 4.10 (for $D_{16v_z} = 10^{-30}$ and $D_{16v_z} = 10^{-25}$, filled and non-filled circles, respectively) together with the theoretical predictions given by Eqs. (3.15), (3.18), (3.23) and (3.25) (dashed-dotted line of brown color) and given by Eqs. (3.23) and (3.26) (dashed-dotted line of sand color). Other lines in Fig. 4.10 use the leading order approximation in ϕ_{eq} given by Eq. (3.30) with four estimates for $\Delta\omega$: from simulations $\Delta\omega = \Delta\omega^{NUM}$; $\Delta\omega = \Delta\omega^{Rose}_{NL}$ from Eq. (3.20) and $\Delta\omega = \Delta\omega^{Dewar}_{NL}$ for two cases of Eq. (3.21).

We conclude from Fig. 4.10 that while theoretical prediction based on Eqs. (3.15), (3.18), (3.23) and (3.25) claims no growth for the amplitudes $\phi_{eq} \gtrsim 0.3$, we still observe growth for even higher amplitudes. Eqs. (3.23) and (3.26) predict growth for any amplitudes but differ from the numerical results by $\sim 70\%$ while approximations $\gamma^{max} \approx |\Delta\omega^{Rose}|/4$,$\gamma^{max} \approx |\Delta\omega^{NUM}|/4$ and $\gamma^{max} \approx |\Delta\omega^{Dewar}|/4$

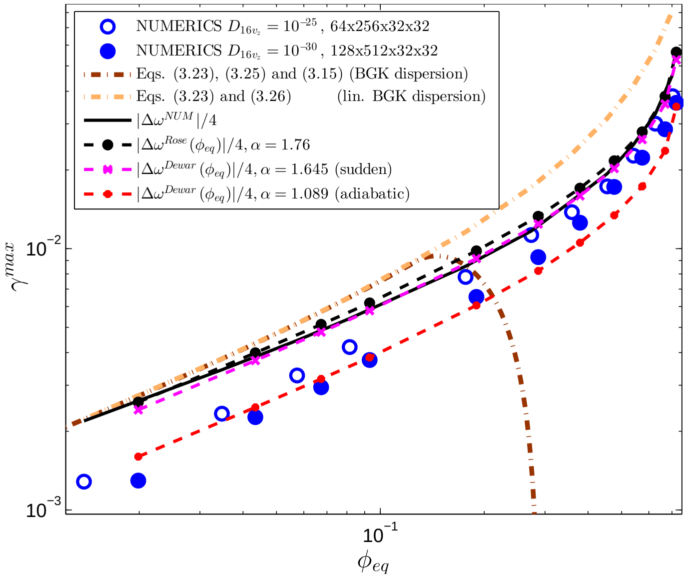

Figure 4.10: The maximum growth rate as a function of BGK amplitude ϕ_{eq}.

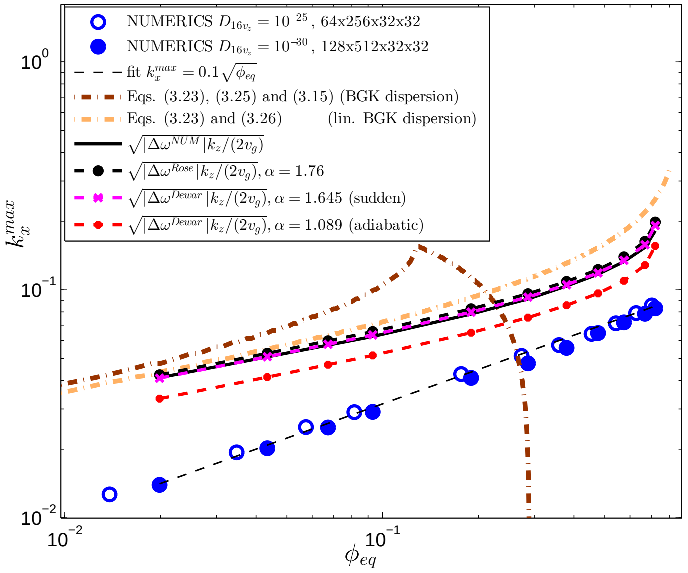

Figure 4.11: The wavenumber k_x^{max} at which the growth rate reaches the maximum as a function of BGK amplitude ϕ_{eq}.

with $\alpha = 1.645$ (sudden) work better, especially for amplitudes $\phi_{eq} > 0.1$, staying almost identical to each other. While including $\gamma^{max} \approx |\Delta\omega^{Dewar}|/4$ with $\alpha = 1.089$ (adiabatic) curve into Fig. 4.10 for comparison, we believe that it's most appropriate to compare the numerical results to $\gamma^{max} \approx |\Delta\omega^{Dewar}|/4$ with $\alpha = 1.645$ (sudden) as Fig. 4.7 clearly shows that an actual frequency shift $\Delta\omega^{NUM}$ is much closer to $\Delta\omega^{Dewar}$ with "sudden" distribution rather than "adiabatic" one. In all these comparisons with theory we assumed in Eq. (3.23) that $\nu_{residual} = 0$ consistent with the expected absence of sideloss in the periodic BC in x as discussed in the beginning of Section 4. Landau damping, for modes that propagate at some finite angle, is neglected. The authors are not aware of any satisfactory model for such in the literature. That which is available [31] is ad hoc and fails to properly describe the nonlinear frequency shift. It predicts approximately twice larger nonlinear frequency shift for a wave of given amplitude than the nonlinear frequency shift that Dewar's sudden model does or the actual frequency shift of our BGK modes.

The wavenumber $k_x = k_x^{max}$ at which the growth rate has the maximum is shown in Fig. 4.11 as a function of ϕ_{eq} together with the theoretical predictions. Dashed-dotted line of sand color represents prediction by Eqs. (3.15), (3.18), (3.23) and (3.25), dashed-dotted line of brown color represents prediction by Eqs. (3.23) and (3.26), other lines in Fig. 4.11 use the leading order approximation in ϕ_{eq} given by Eq. (3.32) with the BGK mode group velocity v_g defined in Eq. (3.26). They include different estimates of $\Delta\omega$, from Rose's model (3.20), Dewar's model (3.21) and measured $\Delta\omega^{NUM}$. The equation (3.32) predicts $k_x^{max} \propto \sqrt{\Delta\omega}$, which in case of $\Delta\omega \propto \sqrt{\phi_{eq}}$ as in Eqs. (3.20) and (3.21) becomes $k_x^{max} \propto (\phi_{eq})^{1/4}$ and fails to agree with numerical results for k_x^{max} somewhat well as seen in Fig. 4.11. It is also seen in Fig. 4.11 that the empirical dependence $k_x^{max} \sim 0.1\sqrt{\phi_{eq}}$ fits the numerical results pretty well but remains to be explained theoretically.

We also investigated the convergence of growth rates with $D_{16v_z} \rightarrow 0$ while

$\Delta z, \Delta v_z \to 0$ and, correspondingly, $N_z, N_{v_z} \to \infty$ while keeping $N_x = 32, N_{v_x} = 32$ (the discretization in x space does not affect the error in growth rates and 32 points in v_x space together with $v_x^{max} = 6$ are enough to resolve the Maxwellian distribution in v_x direction with error $< 10^{-8}$). We found that the relative errors in our numerical results for growth rates with $D_{16v_z} = 10^{-30}$ and $128 \times 512 \times 32 \times 32$ grid points for (z, v_z, x, v_x) are within $10-15\%$ range. Reducing Δt affected the growth rates results even less so we concluded that $\Delta t = 0.1$ was sufficient for these simulations.

4.3 Comparison of Filamentation Instability Growth Rates with PIC Code Simulations

We now compare γ_{k_x} that we obtained in Section 4.2 from our simulations for the mode with $(k_z = 0.35, k_x = 0.05)$ to the growth rates of the same mode obtained using PIC simulations in Fig. 9(j) of Ref. [30] given here in Fig. 4.12 for three different amplitudes of BGK modes: $\phi_{eq} = 0.2, 0.3, 0.5$. These BGK modes in both cases were constructed using $k_z = 0.35$ and have $v_\varphi = 3.35818,\ 3.32288,\ 3.23266$, respectively. Our growth rates for these three amplitudes are 0.0073, 0.0113 and 0.0158. The corresponding growth rates from Ref. [30] are 0.0075, 0.012, and 0.0147, i.e. only $\sim 10\%$ difference with our results. Also notice in Fig. 4.12 that due to intrinsic numerical noise in PIC simulations we can only observe growth of the corresponding harmonics for 1-2 orders of magnitude while using phase-space simulations like ours (see Fig. 4.2) we can observe growth of the corresponding harmonics for 10-14 orders of magnitude.

The total number of particles used in Ref. [30] was $\approx 2 \times 10^8$ with 32x1280 cells and 5000 particles per cell. Number of grid points in our simulations was 64x256x32x32 for (z, v_z, x, v_x) (total $\approx 1.6 \times 10^7$) with $L_z = 2\pi/k_z, L_x = 200\pi, v_z^{max} =$

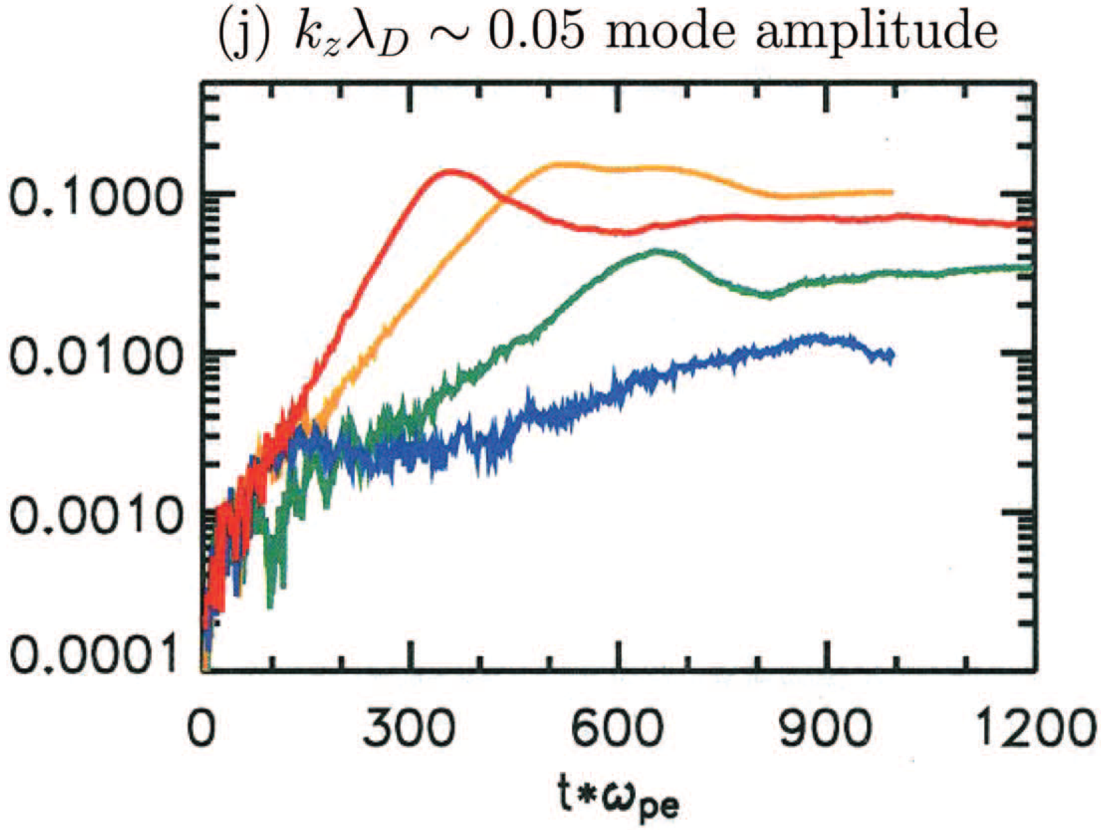

Figure 4.12: Results from 2D PIC simulations using BGK equilibrium for $k_z = 0.35$. (j) Comparison of the wave amplitude as a function of time for the mode at $k_x \sim 0.05$ for $\phi_{eq} = 0.15$ (blue), $\phi_{eq} = 0.2$ (green), $\phi_{eq} = 0.3$ (orange), and $\phi_{eq} = 0.5$ (red) in simulations with 1 Langmuir wavelength in z and 40 wavelengths in x.

$8, v_x^{max} = 6$, and $D_{16v_z} = 10^{-25}, \Delta t = 0.1, T_{final} = 5000$.

Chapter 5

Creation of 1D+1V EPWs By External Pumping and their Filamentation Instability

In this Chapter we consider the process of creation of nonlinear electron plasma waves (EPWs) by external pumping. These EPW are dynamically prepared by starting from uniform in space initial conditions with Maxwellian distribution of particle velocities and applying external electric field of constant amplitude for a finite period of time to create a nonlinear EPW with the desired amplitude. We consider two types of pump. The first type is a weak pump. We found from simulations that a pump amplitude cannot be made arbitrary small (even if applied for an arbitrary large period of time) if we aim to obtain an EPW with a given finite amplitude. Then by a weak pump we mean applying as small amplitude of the pump as possible to achieve the necessary amplitude of an EPW. The second type of pump (we called it a strong pump) has ten fold larger amplitude of the pump compared with the first type. This allows about a ten times shorter duration of pumping. After pumping of either type is extinguished, we observe nonlinear EPWs which are not constant amplitude waves even in 1D but rather they experience small oscillations $\sim 5\%$ near an average amplitude while travelling as shown in Fig. 5.1. In that sense we call these solutions BGK-like modes. By construction, they are the dynamically accessible nonlinear EPWs. We start by performing 1D+1V Vlasov simulations, solving Eqs. (2.1)-(2.5) with periodic boundary conditions and external electric potential given in (5.1) in phase space (z, v_z), to demonstrate the properties of these EPWs.

5.1 Creation of BGK-like Solutions by Weak External Pumping

We consider the beating of laser and SRS light as a source of LWs, idealized as a travelling wave sinusoidal external potential Φ^{ext}, with phase speed v_φ and wavenumber k_z:

$$\Phi^{ext} = \Phi_{pump}(t)\cos[k_z(z - v_\varphi t)],\ \ k_z = |\mathbf{k}|, \tag{5.1}$$

where $\Phi_{pump}(t)$ is prescribed.

1D BGK-like mode is prepared by starting from the spatially uniform Maxwellian distribution

$$f_0(v_z) = \frac{\exp(-v_z^2/2)}{\sqrt{2\pi}} \tag{5.2}$$

at $t = 0$ and adding the travelling external electric potential Φ^{ext} as in Eq. (5.1) with

$$\Phi_{pump}(t) = -\phi_{pump} H(T_{off} - t) \tag{5.3}$$

where T_{off} is the time when the pumping is turned off, $H(T_{off} - t)$ is the Heaviside step function ($H(T_{off} - t) = 1$ for $t < T_{off}$ and $H(T_{off} - t) = 0$ for $t > T_{off}$). $v_\varphi = \omega_{LW}(k_z)/k_z$, where ω_{LW} is the linear LW frequency (real part of a complex root of $\varepsilon_0(k_z, \omega_{LW}) = 0$, where ε_0 as in (3.16), see e.g. [18, 19]). In this dissertation we work with $\omega_{LW}(k_z = 0.35) = 1.22095\ldots$ and $\omega_{LW}(k_z = 0.425) = 1.31759\ldots$. Note that instead of $v_\varphi = \omega_{LW}(k_z)/k_z$, we can choose e.g. $v_\varphi = \omega_{BGK}(k_z, \phi_{eq})/k_z$ from BGK mode described in Chapter 3 which is a function of ϕ_{eq}. We found that such a choice results in $< 10\%$ variation of the growth rate of the transverse instability for typical values of ϕ_{eq} used in Section 6.1 below.

Since we pump the 1st harmonic of our system in z-direction then we expect that the 1st Fourier harmonic amplitude $\phi_1(t) \equiv 2|\int_0^{L_z} \Phi^{int}(z,t) \exp(ik_z z) dz|/L_z$ of internal electric field to be the strongest compared to other harmonics. Indeed, we observed throughout simulations that the 2nd harmonic of Φ^{int} is about 2 orders less than ϕ_1, the 3rd harmonic of Φ^{int} is about one order less than 2nd and so on.

If we pump the system continuously without turning off the external pump ($T_{off} = \infty$), we observe that ϕ_1 does not grow further than some maximum value, instead it first increases, reaches the global maximum (sometimes the global maximum is not the first local maximum), and then it decreases (in this stage $\Phi^{int}(z)$ and $\Phi^{ext}(z)$ are out of phase and the energy is being sucked out of the system by external electric field rather then being pumped into it) after which ϕ_1 keeps oscillating with a period much longer than the bounce period $T_{bounce} = 2\pi/\omega_{bounce}$, with the bounce frequency $\omega_{bounce} \approx k_z\sqrt{\phi_1}$ in dimensionless units.

Fig. 5.1 shows evolution of $\phi_1(t)$ for the two cases with $T_{off} = \infty$ and $T_{off} = 110$. In both cases we take $\phi_{pump} = 0.01$ and $k_z = 0.35$. In the first case, ϕ_1 experiences the initial growth, after which it keeps oscillating with a period $T_{big} \approx 230$ around an average value ~ 0.15. Notice that the global maximin of $\phi_1(t)$ is actually the second local maximum and the duration between two local maximums (at $t \approx 121$ and $t \approx 169$) is $\simeq 48$ which corresponds to the bounce period $T_{bounce} \approx 2\pi/(k_z\sqrt{\phi_1}) \approx 2\pi/(0.35\sqrt{0.15}) \approx 46$. In the second case, when the external pump is turned off at $t = T_{off} = 110$, ϕ_1 after short transient behaviour remains almost constant (≈ 0.21)

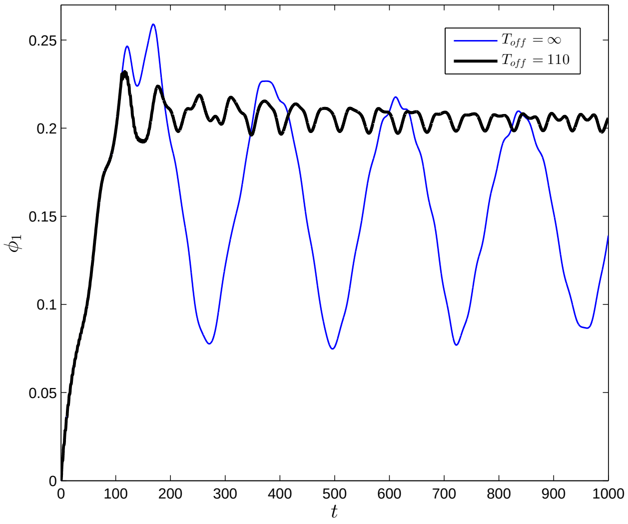

Figure 5.1: The evolution of ϕ_1, the first harmonic of internal electric field, for two cases: $T_{off} = \infty$ and $T_{off} = 110$. $\phi_{pump} = 0.01$ and $k_z = 0.35$ for the both cases.

for the rest of time experiencing small oscillations around the average value, which we call ϕ_{eq}.

Figs. 5.2(a) and 5.2(b) show snapshots of the electron phase space distribution function $f(z, v_z, t)$ around the trapping region for the simulation with $T_{off} = 110$ at times $t = T_{off} = 110$ and $t = 1000$, respectively. A spiral can be seen in these Figs. to develop in the trapping region with a number of revolutions $\approx t/T_{bounce}$. Fig. 5.3 shows the widest cross-sections of the trapping region from the same times as in Figs. 5.2(a) and 5.2(b). They are also compared to the cross-section of a BGK mode of the same amplitude $\phi_{eq} = 0.2$ that was constructed analytically as in Chapter 3 with parameters $k_z = 0.35$, $\phi_{eq} = 0.2$ and $v_\varphi = 3.3585$ (according to the BGK dispersion relation Eq. (3.15)). The trapping regions in Fig. 5.3 have the same width since the waves have the same amplitude while the absolute values of $f(z, v_z, t)$ are higher for the BGK mode since it has the smaller v_φ. These results were obtained in moving frame with the velocity v_φ. The spiral in the density distribution function of the BGK-like mode develops increasingly smaller scale structures with

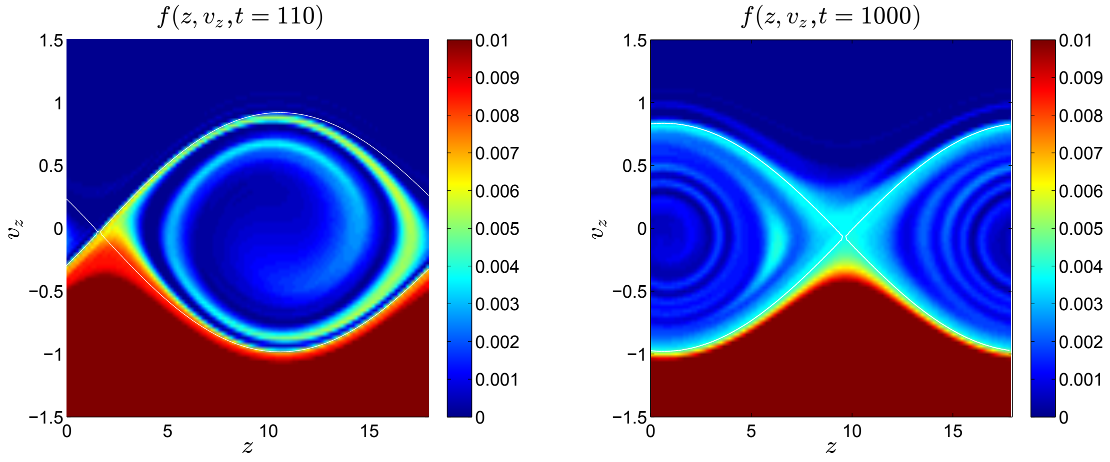

(a) $t = T_{off} = 110$, $n_{trapped}/n_{total} = 0.00222$ (b) $t = 1000$, $n_{trapped}/n_{total} = 0.00216$

Figure 5.2: The density plot of $f(z, v_z, t)$ at times $t = 110$ and $t = 1000$. $\phi_{pump} = 0.01$, $T_{off} = 110$ and $k_z = 0.35$. White contour marks the boundaries of the trapping region, the fraction of trapped particles is $n_{trapped}/n_{total}$.

time that need increasingly higher number of grid points to be resolved accurately. In our simulations these smaller scale structures are smoothed out by the presence of small hyper-viscosity (see more in Section 6) which is chosen to be small enough to not affect the amplitude ϕ_{eq} of BGK-like mode during the entire time of simulation.

The resulting amplitude ϕ_{eq} depends on ϕ_{pump} and T_{off}. As we already discussed at the beginning of this Section, if we fix ϕ_{pump}, there is only a certain range of amplitudes of EPW $0 \leq \phi_{eq} \leq \phi_{eq}^{max}(\phi_{pump})$ that can be achieved by varying T_{off}, where the dependence $\phi_{eq}^{max}(\phi_{pump})$ is obtained from simulations. To get ϕ_{eq} close to ϕ_{eq}^{max}, we need to turn the pump off around (but not exactly) the time when $\phi_1(t)$ is close to its global maximum as exemplified in Fig. 5.1. To study this question more systematically we performed a series of simulations with $k_z = 0.35$, $\phi_{pump} = 0.01$ and various T_{off} and obtained ϕ_{eq} as a function of T_{off} (see Fig. 5.4). The maximum $\phi_{eq}^{max} = 0.2358$ is obtained if we choose $T_{off} \approx 155$ while the global maximum of $\phi_1(t)$ is achieved at $t = t_{glob} = 169$. This difference $t_{glob} - T_{off}$ is about one third of the

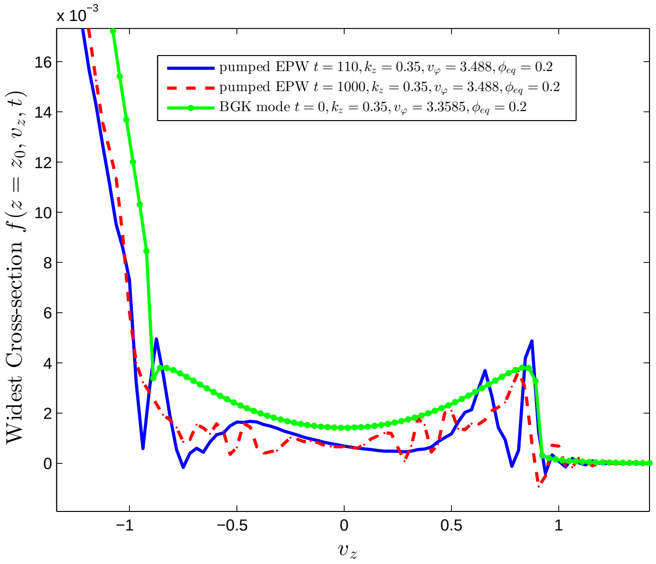

Figure 5.3: The widest cross-sections of $f(z = z_0, v_z, t)$ of the trapping regions at $t = 110$ and $t = 1000$ of the weakly pumped EPW obtained with parameters $k_z = 0.35$, $v_\varphi = 3.488$, $\phi_{pump} = 0.01$, $T_{off} = 110$ and resulting $\phi_{eq} = 0.2$ in comparison with the widest cross-sections of the trapping region of BGK mode constructed analytically as in Chapter 3 with parameters $k_z = 0.35$, $\phi_{eq} = 0.2$ and $v_\varphi = 3.3585$ (according to the BGK dispersion relation (3.15)). z_0 is chosen such that the resulting cross-sections have the maximum width.

bouncing period $t_{glob} - T_{off} = 14 \simeq T_{bounce}/3 \approx 12$ estimated from ϕ_{eq}^{max}. Looking at other values ϕ_{pump} we found that typically the maximal value of $\phi_{eq} = \phi_{eq}^{max}$ can be obtained if the pump is switched off about $T_{bounce}/3$ before the global maximum of $\phi_1(t)$ is achieved. The same ϕ_{eq} can also be achieved by using a larger ϕ_{pump} (and respectively smaller T_{off}) but not a smaller ϕ_{pump}. In this sense we obtain EPW with amplitude $\phi_{eq} = \phi_{eq}^{max}$ using the smallest ϕ_{pump} possible (and correspondingly the largest T_{off}). We call these forcing parameters (ϕ_{pump} and T_{off}) obtained for the given $\phi_{eq} = \phi_{eq}^{max}$ the *weak pumping*. After such smallest ϕ_{pump} (together with T_{off}) is found for a given ϕ_{eq} (or, in practice, we fix ϕ_{pump} and maximize ϕ_{eq} varying T_{off}), we run 2D+2V simulations with the forcing (5.3) as described above.

Tables 5.1 and 5.2 provide a set of approximate values ϕ_{pump} and T_{off} found by

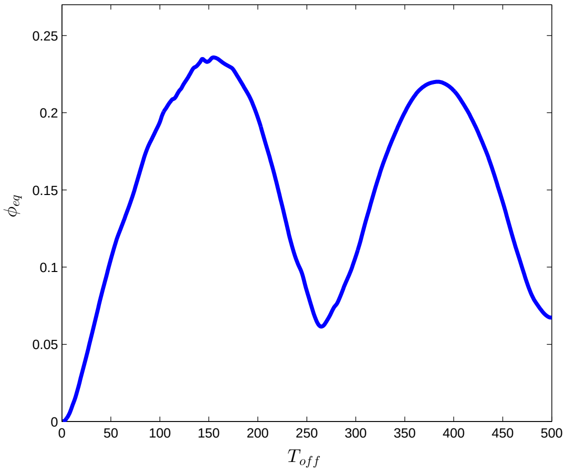

Figure 5.4: The amplitude ϕ_{eq} of EPW as a function of T_{off} for $\phi_{pump} = 0.01$ and $k_z = 0.35$.

this procedure that we used for our 2D+2V simulations for $k_z = 0.35$ and $k_z = 0.425$ correspondingly. We did not aim to obtain these values with very high precision (but rather $\sim 20\%$ within the optimal values) because further increase in precision has a

Table 5.1: Parameters of simulations with *weak pumping* for $k_z = 0.35$, $L_z = 2\pi/k_z, v_z^{max} = 8, v_x^{max} = 6, N_x = 64, N_{v_x} = 32$.

Δt	D_{16v_z}	N_z	N_{v_z}	ϕ_{pump}	T_{off}	ϕ_{eq}	T_{final}	L_x
0.1	10^{-30}	32	512	0.0005	200	0.007	20000	1600π
0.1	10^{-30}	48	512	0.001	200	0.022	20000	1600π
0.1	10^{-25}	48	256	0.002	200	0.053	10000	1600π
0.05	10^{-25}	48	256	0.003	210	0.085	7500	800π
0.05	10^{-25}	64	256	0.005	210	0.13	5000	800π
0.05	10^{-25}	64	256	0.01	110	0.20	4000	800π
0.05	10^{-25}	64	256	0.015	110	0.29	3000	400π
0.05	10^{-25}	96	256	0.02	120	0.38	3000	400π
0.05	10^{-25}	96	256	0.03	100	0.50	3000	400π
0.05	10^{-25}	96	256	0.04	100	0.59	2000	400π
0.05	10^{-25}	96	256	0.05	90	0.69	2000	400π
0.05	10^{-25}	128	256	0.06	80	0.77	2000	400π
0.05	10^{-25}	128	256	0.07	80	0.84	1500	400π
0.05	10^{-25}	128	256	0.1	70	1.01	1200	400π

Table 5.2: Parameters of simulations with *weak pumping* for $k_z = 0.425$, $L_z = 2\pi/k_z, v_z^{max} = 8, v_x^{max} = 6, N_x = 64, N_{v_x} = 32$.

Δt	D_{16v_z}	N_z	N_{v_z}	ϕ_{pump}	T_{off}	ϕ_{eq}	T_{final}	L_x
0.1	10^{-30}	64	512	0.002	100	0.0106	7000	1600π
0.1	10^{-30}	64	512	0.003	100	0.0195	6000	1600π
0.1	10^{-30}	64	512	0.005	100	0.036	6000	1600π
0.05	10^{-25}	48	256	0.007	100	0.052	5000	800π
0.05	10^{-25}	48	256	0.01	100	0.075	5000	800π
0.05	10^{-25}	48	256	0.016	60	0.10	3500	800π
0.05	10^{-25}	64	256	0.025	60	0.15	2500	400π
0.05	10^{-25}	64	256	0.035	60	0.21	2000	400π
0.05	10^{-25}	96	256	0.06	50	0.31	1600	400π
0.05	10^{-25}	128	256	0.13	35	0.51	1100	400π
0.05	10^{-25}	128	256	0.2	30	0.63	1000	200π
0.05	10^{-25}	128	256	0.25	30	0.73	8000	200π
0.05	10^{-25}	128	256	0.4	27	0.86	600	200π

small effect on transverse instability growth rates. First three rows in Tables 5.1 and 5.2 are even more than 20% away from optimal parameters ϕ_{pump} and T_{off}.

Another way to look at the degree of "strength" of the pumping of EPW is to see how many revolutions the spiral in the trapping region of the distribution function makes before the pumping is turned off. Following the estimates in Ref. [58], we conventionally call the pumping *weak* if it makes more than one revolution during the pumping period or $\int_0^{T_{off}} dt/T_{bounce}(t) > 1$, or equivalently $\int_0^{T_{off}} \omega_{bounce}(t)dt > 2\pi$. Assume that the pump is switched off not later than a global maximum of $\phi_1(t)$ is achieved and that $\phi_1(t)$ grows approximately linearly during $0 < t < T_{off.}$ Also we estimate ϕ_{eq} as $\phi_{eq} \approx \phi_1(T_{off})$, then the condition of pumping strength of Ref. [58] is reduced to $k_z\sqrt{\phi_{eq}}T_{off} > 3\pi$, i.e.

$$T_{off} > 3\pi/(k_z\sqrt{\phi_{eq}}). \tag{5.4}$$

All simulation parameters of Tables 5.1 and 5.2 satisfy the criterion of adiabaticity Eq. (5.4) except for the first row in Table 5.1 and the first three rows in Table 5.2.

5.2 Creation of BGK-like Solutions via Strong External Pumping

After the weak pump parameters (ϕ_{pump} and T_{off}) are found for the desired amplitude of EPW ϕ_{eq} we can find stronger pumping parameters (with larger ϕ_{pump} and smaller T_{off}) that provide the same ϕ_{eq}. Typically, if we want to keep ϕ_{eq} fixed and increase ϕ_{pump} two times we need to decrease T_{off} a little more than two times. In the limit $\phi_{pump} \to \infty$ and $T_{off} \to 0$, the action of the pump becomes equivalent to an initial perturbation of electron density in z-direction by δ-function in time followed by a further evolution of the system without external pump.

To study the difference in terms of transverse instability of EPWs obtained by weak and strong pumps we performed another set of simulations with $k_z = 0.35$ and the rest of parameters the same as in Table 5.1 with the only difference that ϕ_{pump} was 10 times larger and T_{off} was 10 times smaller than in Table 5.1. We call such pumping parameters by *strong pumping.* The corresponding amplitudes ϕ_{eq} for the strong pumps were $30 - 60\%$ larger than for the weak pumps and are given in Table 5.3 with the rest of simulation parameters. They could have been matched to the amplitudes ϕ_{eq} of corresponding weak pumps by further adjusting T_{off}, but it was not necessary for us below since we were comparing the simulations not one-to-one but rather a set of simulations with weak pumps to a set of simulations with strong pumps. All the simulations with strong pumping do not satisfy the criterion of adiabaticity Eq. (5.4).

Table 5.3: Parameters of simulations with *strong pumping* for $k_z = 0.35$, $L_z = 2\pi/k_z, v_z^{max} = 8, v_x^{max} = 6, N_x = 64, N_{v_x} = 32$.

Δt	D_{16v_z}	N_z	N_{v_z}	ϕ_{pump}	T_{off}	ϕ_{eq}	T_{final}	L_x
0.1	10^{-30}	32	512	0.005	20	0.0082	11000	1600π
0.1	10^{-30}	48	512	0.01	20	0.039	8000	1600π
0.1	10^{-30}	48	512	0.015	20	0.055	7000	1600π
0.05	10^{-25}	48	256	0.02	20	0.081	5000	800π
0.05	10^{-25}	48	256	0.025	20	0.11	5000	800π
0.05	10^{-25}	48	256	0.03	21	0.14	4000	800π
0.05	10^{-25}	48	256	0.04	21	0.14	4000	800π
0.05	10^{-25}	64	256	0.05	21	0.25	3000	800π
0.05	10^{-25}	64	256	0.1	11	0.26	2500	800π
0.05	10^{-25}	96	256	0.15	11	0.40	2000	400π
0.05	10^{-25}	96	256	0.2	12	0.59	1500	400π
0.05	10^{-25}	96	256	0.3	10	0.72	1200	400π
0.05	10^{-25}	128	256	0.4	10	0.91	1000	400π
0.05	10^{-25}	128	256	0.5	9	0.98	1000	400π
0.05	10^{-25}	128	256	0.6	8	1.00	1000	200π
0.05	10^{-25}	128	256	0.7	8	1.11	1000	200π
0.05	10^{-25}	128	256	1	7	1.27	700	200π

5.3 Nonlinear Frequency Shift of EPW

Contrary to Section 3.2 where we had the dispersion relation (3.15) for a special class of BGK waves, we don't have a single dispersion relation for a general nonlinear EPW as it strongly depends on how that EPW was created (in particular it's particle distribution) as there is a big freedom in terms of many distributions that correspond to EPWs with the same parameters k_z, v_φ and ϕ_{eq}.

However, we can recover EPW's frequency $\omega(k_z, \phi_{eq})$ directly from simulations after it was created as the rate of change of phase of the first Fourier harmonic of internal electric field $\Phi^{int}(z, t)$.

We define EPW's nonlinear frequency shift as

$$\Delta\omega^{BGK} = \omega(k_z, \phi_{eq}) - \omega_{LW}(k_z), \tag{5.5}$$

where $\omega_L W(k_z)$ is the liner LW frequency $\omega_{LW}(k_z)$ (real part of a complex root of $\varepsilon_0(k_z, \omega_{LW}) = 0$, where ε_0 as in (3.16), contrary to $\omega_0(k_z)$ in Section 3.2 which was a real root of $\mathrm{Re}[\varepsilon_0(k_z, \omega_0)] = 0$). For example, $k_z = 0.35$, $\omega_L W = 1.22095$.

As we mention, the nonlinear frequency shift of an EPW depends on the way it was created. Two limiting cases for finite amplitude EPWs have been treated analytically by Dewar in Ref. [21] providing the nonlinear frequency shift approximation

$$\Delta\omega_{NL}^{Dewar} = -\alpha \left[\frac{\partial\varepsilon_0(\omega_{LW})}{\partial\omega}\right]^{-1} f_0''(v_\varphi) \frac{\sqrt{\phi_{eq}}}{k_z^2}, \tag{5.6}$$

where ε_0 is linear dielectric function given by Eq. (3.16) in Section 3.2 and $\alpha = 0.77\sqrt{2} = 1.089$ and $\alpha = 1.163\sqrt{2} = 1.645$ for the "adiabatic" and "sudden" excitation of nonlinear LW, respectively. Our *weak* pump is only somewhat adiabatic in Dewar's sense since its amplitude stays constant for the whole time of driving EPW rather than slowly varying. Our *strong* pump is closer to the sudden case in Dewar's theory yet still no exactly the same since after turning off the external pump our EPW still evolves while Dewar considers the asymptotic limit in which the distribution function is constant along the lines of constant wave-frame energy. $\frac{\partial\varepsilon_0(\omega_{LW})}{\partial\omega} = 2.267$ for $k_z = 0.35$ and $\frac{\partial\varepsilon_0(\omega_{LW})}{\partial\omega} = 1.781$ for $k_z = 0.425$.

5.4 Filamentation Instability of BGK-like Solutions

After the pumping is turned off at $t = T_{off}$, BGK-like solution with the amplitude ϕ_{eq} continue to slowly evolve as shown in Fig. 5.1 and described in Section 5.1. During that slow evolution, the transverse instability of BGK-like solution starts to develop. Similarly to Section 3.3, we look at the linear stage of this instability analytically through the solution in the moving frame in the following form

$$\Phi = \mathrm{Re}\left\{\exp(ik_z z)[\phi_{eq} + \delta\phi(t)\exp(i\delta\mathbf{k}\cdot\mathbf{r})]\right\}, \tag{5.7}$$

where the wave vector $\delta\mathbf{k} \perp \hat{z}$ is responsible for the transverse perturbations with the amplitude $\delta\phi(t)$. Here $\hat{z}$ is the unit vector in z direction. Let $\delta\phi \sim \exp(\gamma t)$. Assuming that ϕ_{eq} does not change with time, we use the result of Ref. [29] outlined in Section 3.3, that

$$(\gamma + \nu_{residual})^2 = -D\left(\phi_{eq}\frac{\partial\omega}{\partial\phi_{eq}} + D\right), \tag{5.8}$$

where D is the generalized diffraction operator given by

$$D = \omega(|k_z\hat{z} + \delta\mathbf{k}|, \phi_{eq}) - \omega(k_z, \phi_{eq}), \tag{5.9}$$

and $\omega(k_z, \phi_{eq})$ is the nonlinear frequency of EPW with the amplitude ϕ_{eq} which we recover directly from simulations.

Additionally, assuming $\phi_{eq} \ll 1$, we approximate $\omega(k_z, \phi_{eq}),\ \phi_{eq} \to 0$ through the liner LW frequency $\omega_{LW}(k_z)$. Also assuming $|\delta\mathbf{k}| \ll 1$, we reduce Eq. (5.9) to the following expression

$$D \approx D_{lin} = \frac{v_g^{LW}}{2k_z}|\delta\mathbf{k}|^2, \quad v_g^{LW} \equiv \frac{\partial\omega_{LW}(k_z)}{\partial k_z}, \tag{5.10}$$

where v_g^{LW} is the linear LW group velocity. Also the residual damping, $\nu_{residual}$, from Eq. (5.8) is model dependent and, as we discussed in Section 3.2, we set $\nu_{residual} = 0$ in (5.8) as it is the only choice that appears to be consistent with our simulations.

For the term $\phi_{eq}\frac{\partial\omega}{\partial\phi_{eq}}$ in Eq. (5.8), we have to take into account the dependence on ϕ_{eq}. Assuming at the leading order that the nonlinear frequency shift $\Delta\omega \equiv \omega(k_z, \phi_{eq}) - \omega_{LW}(k_z) \propto \sqrt{\phi_{eq}}$ we obtain that $\phi_{eq}\frac{\partial\omega}{\partial\phi_{eq}} = \frac{\Delta\omega}{2}$. Maximizing γ over D in Eq. (5.8) we get the maximum value

$$\gamma^{max} = \frac{|\Delta\omega|}{4}, \tag{5.11}$$

at

$$D = -\frac{\Delta\omega}{4}, \tag{5.12}$$

which is valid for $|\delta\mathbf{k}| \ll |\mathbf{k}|$. Using the approximation (5.10), we obtain from Eq. (5.12) the position of the maximum

$$|\delta\mathbf{k}| = k_x^{max} = \left(\frac{-\Delta\omega\, k_z}{2v_g^{LW}}\right)^{1/2}. \tag{5.13}$$

Chapter 6

Numerical Simulations of BGK-like EPWs Filamentation

Here we describe the results of 2D+2V fully non-linear Vlasov simulations performed to study the transverse instability of nonlinear electron plasma waves that were dynamically prepared by starting with uniform in space initial conditions with Maxwellian distribution of particle velocities and pumping the system by both weak and strong pumps described in Section 5.

Boundary conditions and numerical method that we used were the same as described in Section 4.1, except for the initial conditions that were uniform in z and x direction with Maxwellian particle distribution in v_z and v_x directions and the presence of external electrostatic potential for $0 < t < T_{off}$ that pumped the system to create EPW of desired amplitude as described in Chapter 5.

6.1 2D+2V Simulations and Filamentation Instability of Nonlinear EPWs

We start by presenting an example of a simulation with $k_z = 0.35$, $\phi_{pump} = 0.01$, $T_{off} = 110$ and resulting $\phi_{eq} \approx 0.2$. Fig. 6.1 shows the amplitude of the electrostatic potential $\Phi^{int}(z,x,t)$ vs. t. Solid line is for the first $z-$harmonic, $\phi_1(x,t) \equiv 2|\int_0^{L_z} \Phi^{int}(z,x,t)\exp{(ik_z z)}dz|/L_z$ evaluated at $x = 0$, dashed line is for the averaged value $\langle\phi_1\rangle_x = \int_0^{L_x} \phi_1(x,t)dx/L_x$ and dotted line is for the maximum of electrostatic potential $\max\limits_{z,x} \Phi^{int}(z,x,t)$. Other simulation parameters were $D_{16v_z} = 10^{-25}$, $64 \times 256 \times 64 \times 32$ grid points for (z, v_z, x, v_x) with $L_z = 2\pi/k_z, L_x = 800\pi, v_z^{max} = 8, v_x^{max} = 6, \Delta t = 0.05, T_{final} = 5000$. It is seen in Fig. 6.1 that during the action of pumping $\langle\phi_1\rangle_x$ reaches the global maximum. Then after pumping is switched off, $\langle\phi_1\rangle_x$ experiences a short initial transient behaviour, after that it remains almost constant until $t \sim 3500$, after that a strong LW filamentation occurs at $t \sim 4000$ (see Figs. 6.2 and 6.3). During the long quasi-stationary dynamics $500 \lesssim t \lesssim 3500$, we call the quasi-equilibrium value of $\langle\phi_1\rangle_x$ by ϕ_{eq}. In Fig. 6.1 $\phi_{eq} \approx 0.2$. LW filamentation peaks after $t = 4000$ with the value of $\max\limits_{z,x} \Phi^{int}(z,x,t)$ almost twice higher than before filamentation. At that time, a large portion of electrostatic field energy from the first Fourier mode (that has the most of electric field energy) is transferred into kinetic energy as can be seen from the dynamics of $\langle\phi_1\rangle_x$.

We run the simulation for a long enough time (after the pumping is off) to observe the growth of oblique harmonics of electric field with wave vectors $(k_z = 0.35, k_x)$ (see Fig. 6.4 for the spectrum of E_z, the z component of the electric field) in several orders in magnitude (see Fig. 4.2), where k_z is the wavenumber of the pump and k_x varies between $-k_x^{max}$ and $k_x^{max} = \pi/\Delta x$. Here $\Delta x = L_x/N_x$, where N_x is the number of grid points in x. The initial values in these harmonics are near the machine precision. During the simulation they grow from values $\sim 10^{-16}$ to $\sim 10^{-1}$. The exponential

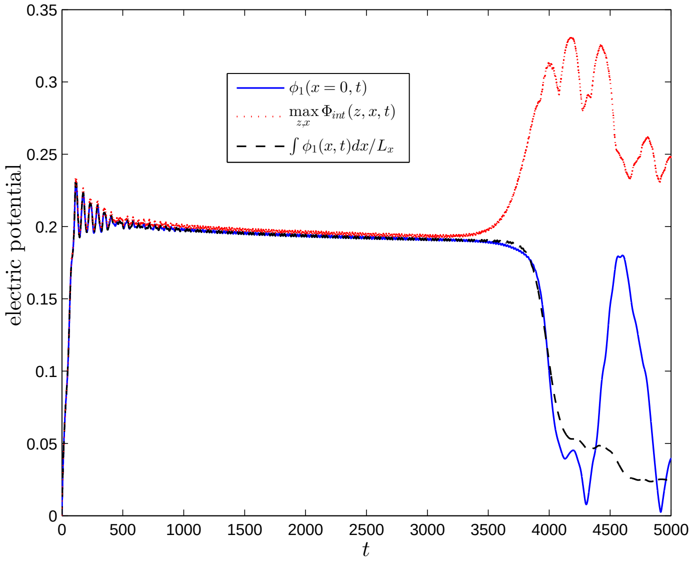

Figure 6.1: Solid line is for the first $z-$harmonic $\phi_1(x,t)$ evaluated at $x = 0$, dashed line is for the averaged value $\int_0^{L_x} \phi_1(x,t)dx/L_x$ and dotted line is for the maximum of electrostatic potential $\max\limits_{z,x} \Phi^{int}(z,x,t)$. Simulation parameters are $\phi_{pump} = 0.01, T_{off} = 110$ and $k_z = 0.35$.

growth rates γ_{k_x} for these harmonics are extracted (see Fig. 6.6) when amplitudes grow from $\sim 10^{-13}$ to $\sim 10^{-8} - 10^{-6}$ (during these times a clear exponential growth $\propto \exp(\gamma_{k_x} t)$ is observed before the nonlinear effects become noticeable). In Fig. 6.6 the maximum growth rate γ^{max} (the maximum over k_x for each fixed ϕ_{eq}) and k_x^{max} are found using quadratic fit to several data points around the maximum.

These kind of simulations were done for a variety of pumped EPWs with $k_z = 0.35$ and $k_z = 0.425$ and amplitudes $0.007 \leq \phi_{eq} \leq 1$. For $k_z = 0.35$ we also considered two cases of pumping (weak and strong) as described in Chapter 5. Parameters typically used for simulations were $D_{16v_z} = 10^{-30} - 10^{-25}$, the time step $\Delta t = 0.05 - 0.1$, the final simulation time T_{final} in the range $1000 \leq T_{final} \leq 20000$ (depending on EPW amplitude ϕ_{eq}) and from $32 \times 256 \times 64 \times 32$ up to $128 \times 512 \times 64 \times 32$ grid points for (z, v_z, x, v_x) with $L_z = 2\pi/k_z, L_x = 200\pi - 1600\pi, v_z^{max} = 8, v_x^{max} = 6$. Smaller

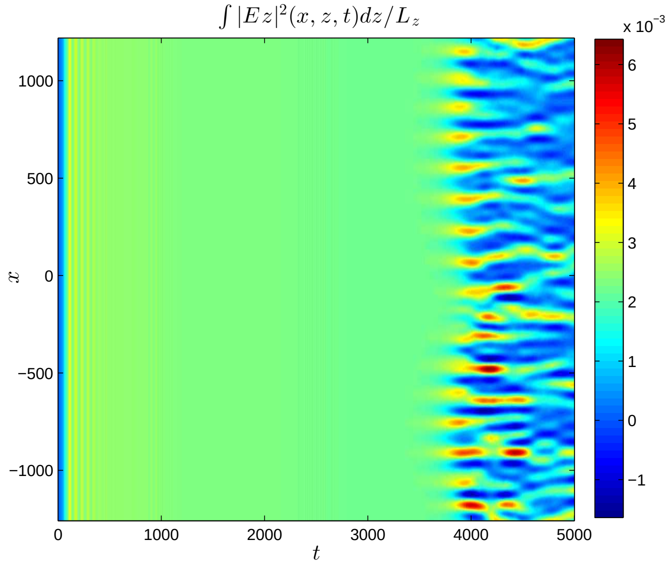

Figure 6.2: The density plot vs. x and t for $\langle|E_z|^2\rangle_z \equiv \int_0^{L_z} |E_z|^2 dz/L_z$ ($|E_z|^2$ averaged over z) shows a development of LW filamentation with time from the pumped EPW with $k_z = 0.35, \phi_{eq} \approx 0.2$.

amplitudes waves have narrower trapping region which requires more grid points and smaller hyper-viscosity coefficient to keep errors at approximately the same level in all of the of simulations. All parameters for simulations with weak pumping and $k_z = 0.35$ are collected in Table 5.1 and with $k_z = 0.425$ are collected in Table 5.2. All parameters for simulations with strong pumping and $k_z = 0.35$ are collected in Table 5.3, these simulations done with the same parameters as in Table 5.1 with the only difference that ϕ_{pump} was 10 times larger and T_{off} was 10 times smaller.

Figs. 6.7 and 6.8 show the measured growth rates as a function of k_x and ϕ_{eq} obtained from a set of simulations with $k_z = 0.35$ and weak pump. We can clearly see the transverse instability for the whole range of amplitudes with higher amplitudes yielding larger growth rates.

In the further discussion we also overlayed data from Refs. [31, 42] (denoted as “LOKI code data” in figures’ legends) that were produced in somewhat similar

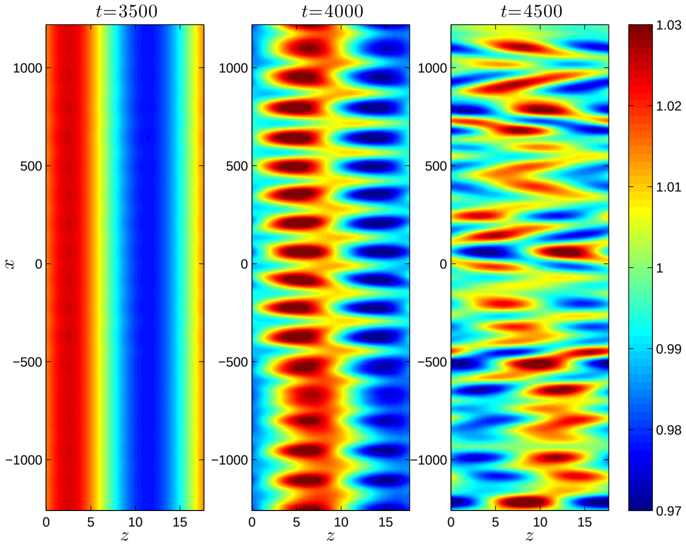

Figure 6.3: The density plot of particle density $\rho(z, x)$ before ($t = 3500$), during ($t = 4000$) and after ($t = 4500$) LW filamentation for pumped EPW with $k_z = 0.35$, $\phi_{eq} \approx 0.2$.

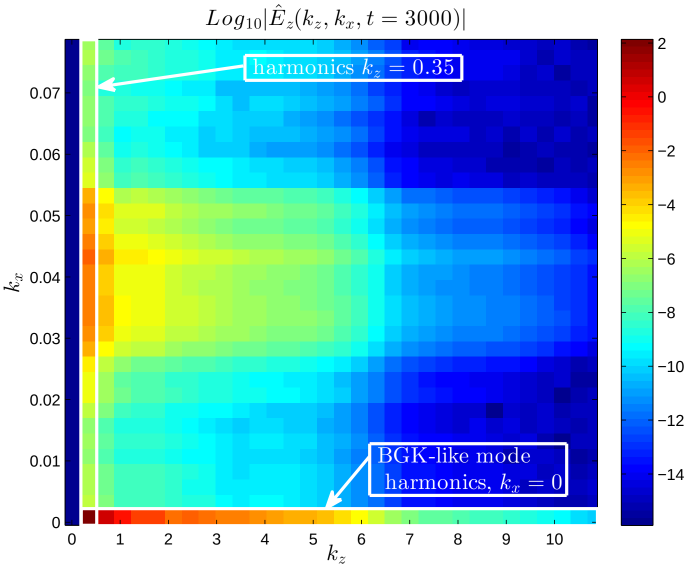

Figure 6.4: The density plot of the spectrum of $E_z(z, x)$ at $t = 3000$.

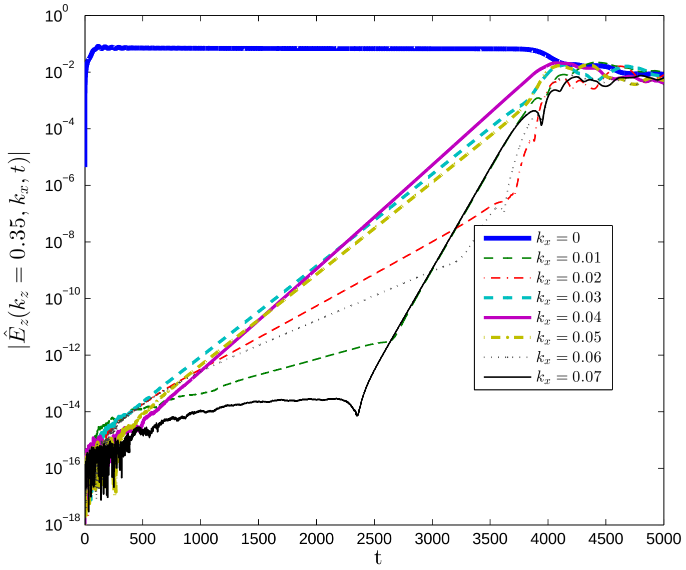

Figure 6.5: The growth of harmonics $|\hat{E}_z(k_z = 0.35, k_x, t)|$ in time.

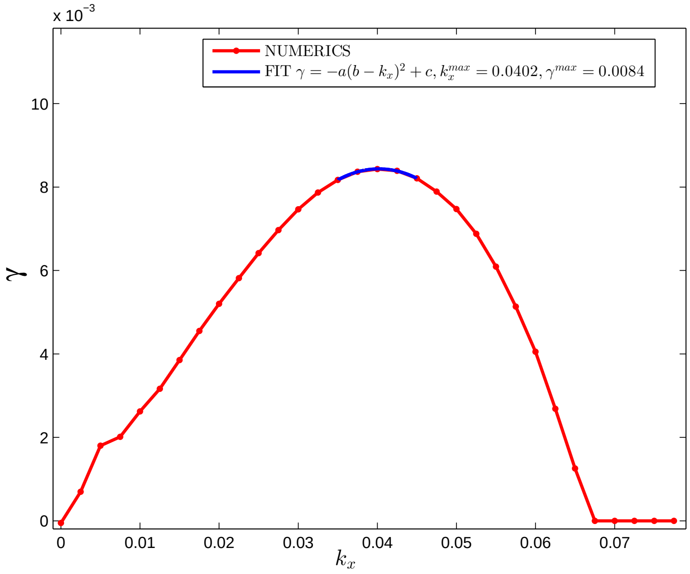

Figure 6.6: The growth rates γ_{k_x} of oblique harmonics extracted from the least-square fit of the data of Fig. 4.2. Also shown a fit to the quadratic law near the maximum.

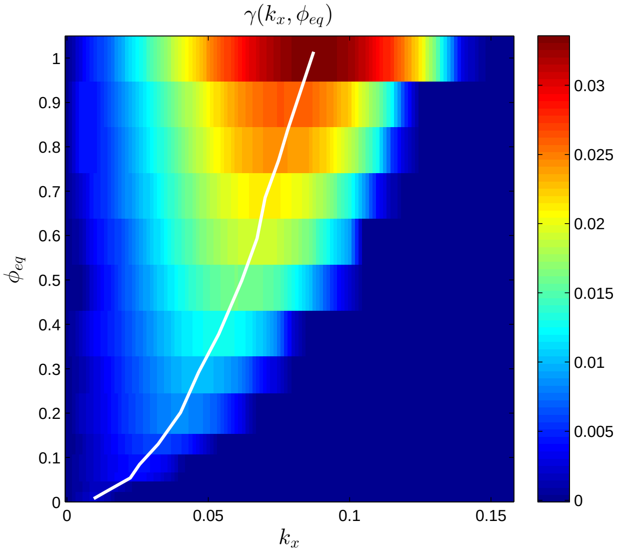

Figure 6.7: The density plot of the growth rate γ_{k_x} as a function of k_x and ϕ_{eq} for $k_z = 0.35$, $v_\varphi = 3.488$. The white line shows the maximum γ_{k_x} over k_x for each ϕ_{eq}.

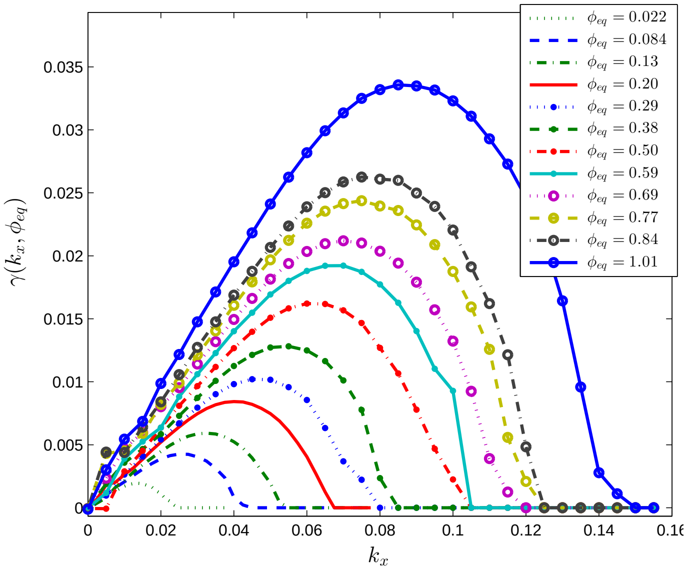

Figure 6.8: The growth rates γ_{k_x} as a function of k_x for EPWs with various amplitudes ϕ_{eq} correspond to multiple cross-sections of Fig. 6.7. $k_z = 0.35$, $v_\varphi = 3.488$.

way (by pumping the system with external electric field in longitudinal direction for $0 < t < 100 = T_{off}$ and measuring growth rates afterwards, however without systematic attempts to minimize ϕ_{pump}) using different kind of numerical scheme (finite volume method of 3-to-4 order) and turning on and off external pumping smoothly with $\tanh(t)$ function. Comparing smooth and non-smooth ways of turning the pump on and off in our simulations, we observed that the differences in results were negligible. Also we used $k_z = 0.35$ and corresponding $\omega_{LW}(kz = 0.35) = 1.22095\ldots$ and $v_\varphi = 3.488$ in our first set of simulations while Refs. [31, 42] used $k_z = 1/3$ and corresponding $\omega_{LW}(k_z = 1/3) = 1.2$ and $v_\varphi = 3.6$ which accounts for 5% difference in k_z, 1.7% difference in ω_{LW} and 3.2% difference in v_φ, but we overlayed these data on the same graphs anyways for comparison. Second set of simulations was performed with exactly matching parameters $k_z = 0.425$, $\omega_{LW}(k_z = 0.425) = 1.3176$ and $v_\varphi = 3.1$ for both our simulations and simulations from Refs. [31, 42].

During the simulations we extract the nonlinear frequency shift $\Delta\omega^{NUM}$ from simulations by finding the wave frequency as the rate of change of the phase of $\phi_1(x = 0, t)$ and subtracting the reference value $\omega_{LW}(k_z)$. Fig. 6.9 shows the nonlinear frequency shift $\Delta\omega^{NUM}$ for both weak and strong pumping (denoted as “STRONG PUMP” in the legend) obtained from simulations in comparison with theoretical ones computed using Dewar’s [21] nonlinear frequency shift approximation as in Eq. (5.6) for the cases of adiabatic ($\alpha = 1.089$) and sudden ($\alpha = 1.645$) excitations. The measured nonlinear frequency shift $\Delta\omega^{NUM}$ is nearly the same for both weak and strong pumping and is close to $\Delta\omega^{Dewar}$ with $\alpha = 1.645$. Also $\Delta\omega^{NUM}$ is mostly within Dewar’s bounds (with $\alpha = 1.089$ and $\alpha = 1.645$) and scales as $\Delta\omega \propto \sqrt{\phi_{eq}}$ for the whole range of amplitudes. Also we overlayed the data from Refs. [31, 42] for comparison. It shows $\sim 30\%$ smaller nonlinear frequency shift since it was produced for $k_z = 1/3$, $v_\varphi = 3.6$ and exhibits different scaling for $\phi_{eq} > 0.4$. If we were to plot the corresponding Dewar’s bounds for the parameters $k_z = 1/3$, $v_\varphi = 3.6$ we would see that their nonlinear frequency shift data are also within those bounds for

$\phi_{eq} < 0.4$.

The maximum growth rate γ^{max} (the maximum over k_x for each fixed ϕ_{eq}) as a function of ϕ_{eq} is shown in Fig. 6.10 together with the perturbative theoretical predictions given by Eq. (5.11) with different estimates for $\Delta\omega$ including Dewar's model (5.6) and $\Delta\omega^{NUM}$ recovered directly from simulations (with weak and strong pumps, respectively). We see that theoretical prediction $\gamma^{max} \approx |\Delta\omega^{NUM}|/4$ from Eq. (5.11) works pretty well for EPWs obtained with weak pump and $\phi_{eq} < 0.2$. In this case the measured growth rates are within $20 - 25\%$ from the estimate, and scale like $\gamma^{max} \propto \sqrt{\phi_{eq}}$. The measured growth rates for the strong pump are $30 - 50\%$ larger compared to the weak pump growth rates and also larger than a corresponding estimate $|\Delta\omega^{NUM}|/4$ in the whole range of amplitudes ϕ_{eq}. Also for amplitudes $\phi_{eq} > 0.3$, the scaling changes for both weak and strong pumps and becomes $\gamma^{max} \propto \phi_{eq}$. The data from Refs. [31, 42] exhibit similar behaviour regarding the scalings and match the corresponding estimate $\gamma^{max} \approx |\Delta\omega^{NUM}|/4$ for amplitudes $\phi_{eq} < 0.4$.

The wavenumber k_x^{max} at which the growth rate is maximum as a function of ϕ_{eq} is shown in Fig. 6.11 together with the theoretical predictions given by Eq. (5.13) with different estimates for $\Delta\omega$. For the group velocity v_g in Eq. (5.13) we use the value $v_g = v_g^{LW} = 1.26112...$ that is calculated using the liner LW dispersion relation for $k_z = 0.35$. For $\Delta\omega$ in theoretical predictions we use Dewar's model as well as the measured $\Delta\omega^{NUM}$ for weak and strong pump cases. None of the theoretical approximations predict k_x^{max} well for small amplitudes ϕ_{eq}. All of them predict $k_x^{max} \propto \phi_{eq}^{1/4}$ while from numerical results we see that $k_x^{max} \sim 0.1\sqrt{\phi_{eq}}$. Absolute values of the measured k_x^{max} differ from $\sqrt{|\Delta\omega^{NUM}|k_z/(2v_g^{LW})}$ of Eq. (5.13) by a factor ~ 3 at $\phi_{eq} = 0.01$ and by factor ~ 2 at $\phi_{eq} = 0.1$. The data from Ref. [31] exhibit a similar scaling, but absolute values of k_x^{max} are smaller by 50% in average. The measured k_x^{max} for the strong pump are $10-20\%$ larger than for the weak pump

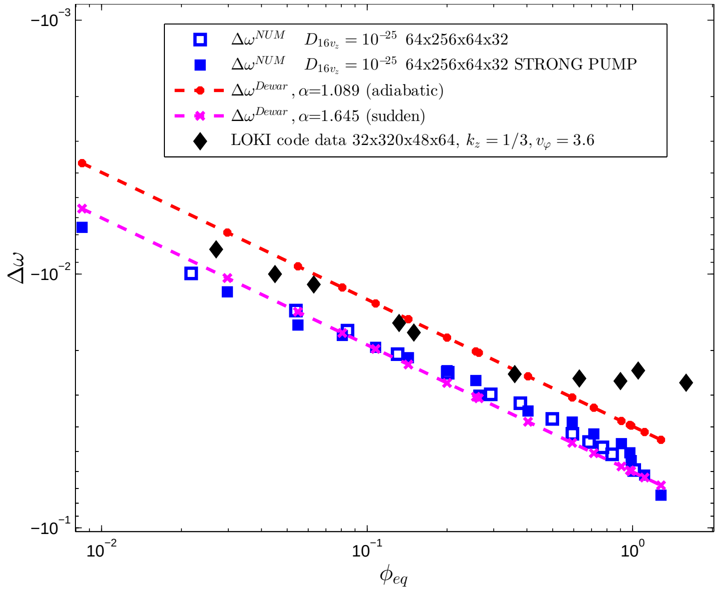

Figure 6.9: The nonlinear frequency shift $\Delta\omega$ as a function of ϕ_{eq} for $k_z = 0.35$, $v_\varphi = 3.488$.

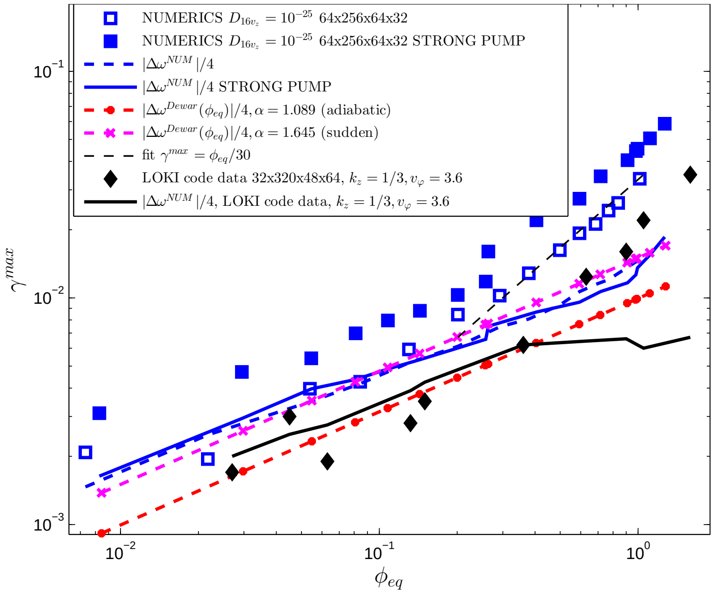

Figure 6.10: The maximum growth rate as a function of ϕ_{eq} for $k_z = 0.35$, $v_\varphi = 3.488$.

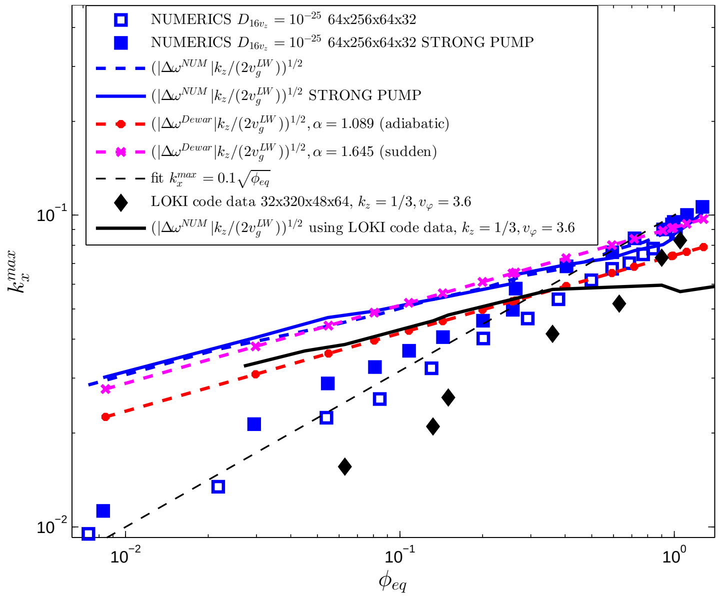

Figure 6.11: The wavenumber k_x^{max} at which the growth rate reaches the maximum as a function of ϕ_{eq} for $k_z = 0.35$, $v_\varphi = 3.488$.

and exhibit the same scaling in the whole range of amplitudes ϕ_{eq}.

The same kind of simulations with weak pump are done for $k_z = 0.425$ with $\omega_{LW}(k_z = 0.425) = 1.3176$, $v_\varphi = 3.1$ and $v_g = v_g^{LW}(k_z = 0.425) = 1.304545...$. The results and a comparison with data from Ref. [31, 42] (when available) are given in Figs. 6.12-6.14. In this case our measured frequency shift $|\Delta\omega^{NUM}|$ is close to $\alpha = 1.645$ (sudden) case in Dewar's theory. In Fig. 6.13 the approximation $\gamma^{max} \approx |\Delta\omega^{NUM}|/4$ works pretty well for $\phi_{eq} < 0.5$. The measured growth rates are within $20 - 25\%$ from the estimate and scale like $\gamma^{max} \propto \sqrt{\phi_{eq}}$. Also for amplitudes $\phi_{eq} > 0.5$ the scaling changes and becomes $\gamma^{max} \propto \phi_{eq}$. The data form Ref. [31, 42] exhibit a similar behaviour regarding the scalings, but absolute values of γ^{max} are approximately 2 times smaller. Using Dewar's approximation for $|\Delta\omega|$ we notice that our growth rates are close to $|\Delta\omega^{Dewar}|/4$ with $\alpha = 1.645$ (sudden), whereas data growth rates from Ref. [31, 42] are close to the case of $\alpha = 1.089$ (adiabatic) for small amplitudes. Unfortunately, the measured $\Delta\omega^{NUM}$ from Ref. [31, 42] were

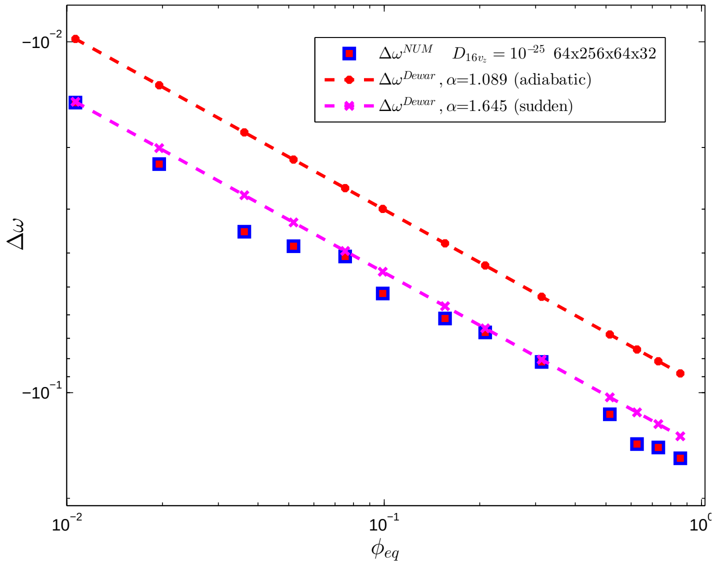

Figure 6.12: The nonlinear frequency shift $\Delta\omega$ as a function of ϕ_{eq} for $k_z = 0.425$, $v_\varphi = 3.1$.

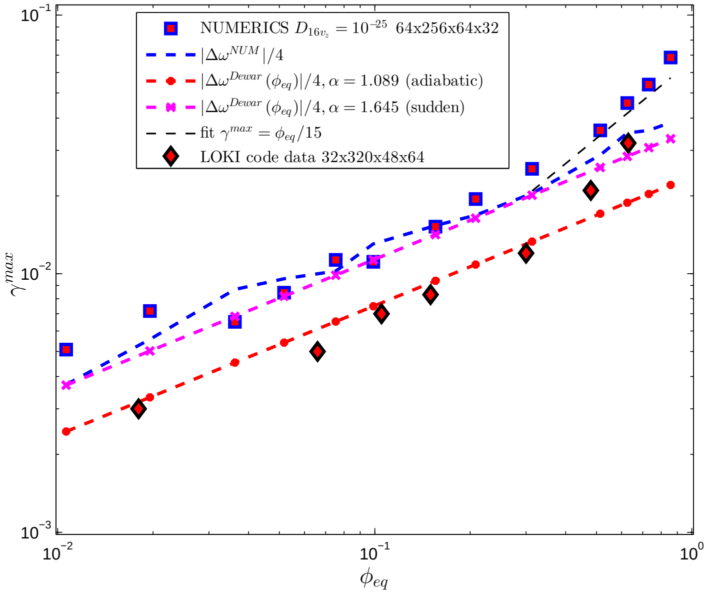

Figure 6.13: The maximum growth rate as a function of ϕ_{eq} for $k_z = 0.425$, $v_\varphi = 3.1$.

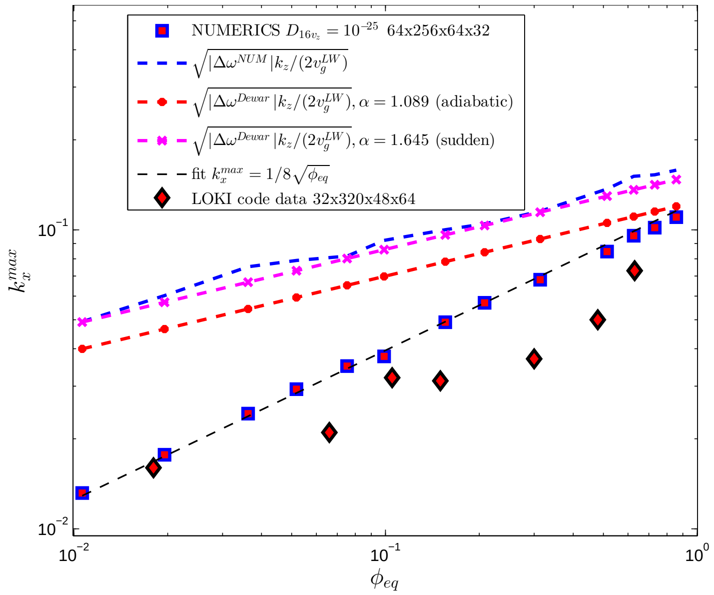

Figure 6.14: The wavenumber k_x^{max} at which the growth rate reaches the maximum as a function of ϕ_{eq} for $k_z = 0.425$, $v_\varphi = 3.1$.

not available for comparison. For k_x^{max} we clearly see that $k_x^{max} \sim 1/8\sqrt{\phi_{eq}}$, so none of the theoretical approximations predict k_x^{max} well.

6.2 Comparison of Filamentation Instability of Nonlinear EPWs and BGK modes

Here we compare the transverse instability results for weakly pumped EPWs with $k_z = 0.35$ found in Section 6 with transverse instability of BGK modes in Chapter 4. Notice that all BGK-like EPWs with various amplitudes were obtained using the pumping frequency $\omega_{LW}(k_z = 0.35) = 1.22095\ldots$ and, respectively, $v_\varphi = 3.488$, whereas the BGK modes for different amplitudes were constructed such that $v_\varphi = v_\varphi(\phi_{eq})$ according to the dispersion relation given by Eq. (3.15) in Section 3.2.

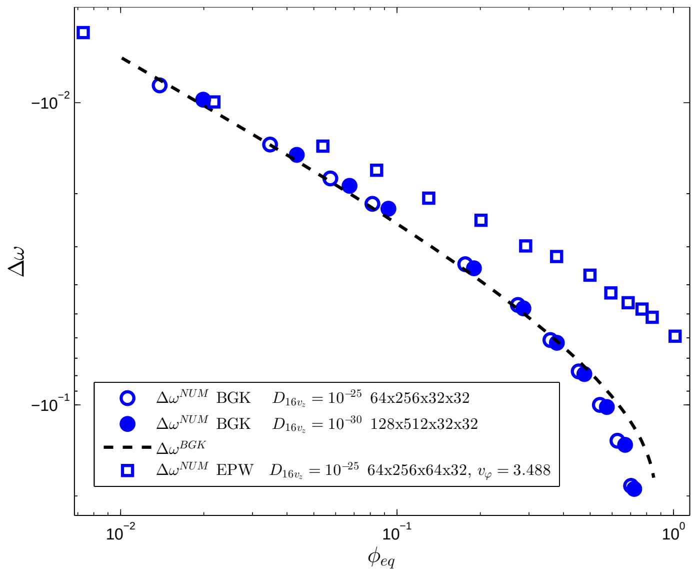

Figure 6.15: The nonlinear frequency shift $\Delta\omega$ as a function of ϕ_{eq} for both BGK modes and pumped EPWs (BGK-like modes) with $k_z = 0.35$.

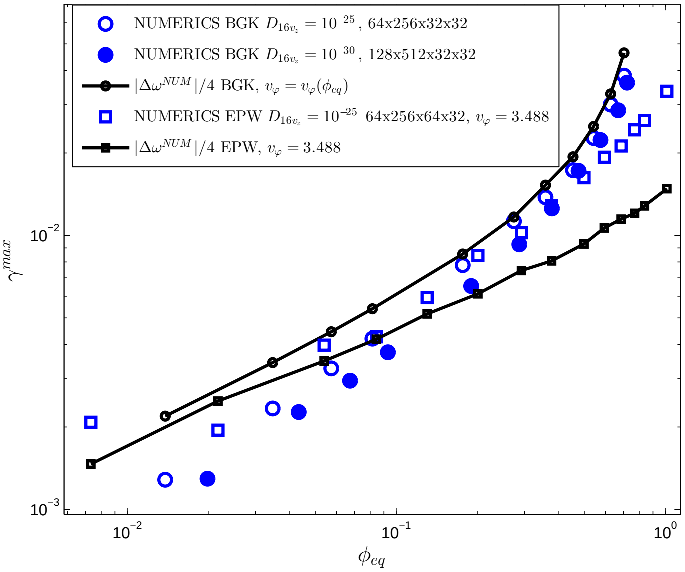

Figure 6.16: The maximum growth rate as a function of ϕ_{eq} for both BGK modes and pumped EPWs with $k_z = 0.35$.

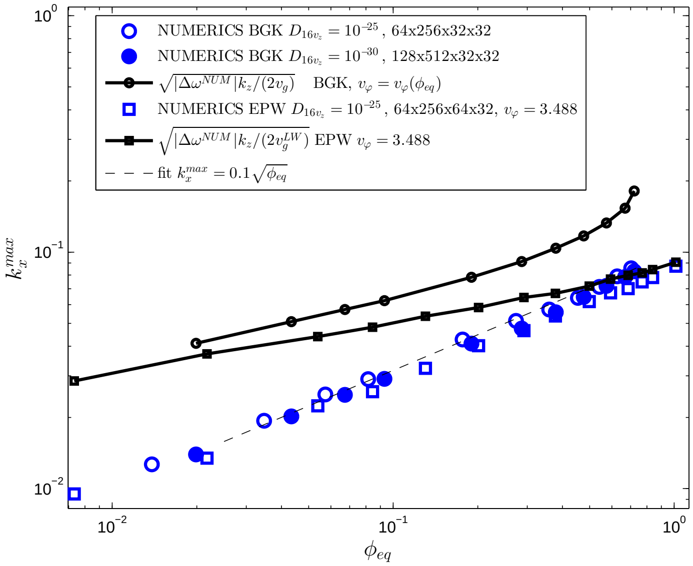

Figure 6.17: The wavenumber k_x^{max} at which the growth rate reaches the maximum as a function of ϕ_{eq} for both BGK modes and pumped EPWs with $k_z = 0.35$.

Fig. 6.15 shows the nonlinear frequency shift obtained from both kinds of simulations. We can see that for small amplitudes $\phi_{eq} < 0.05$, the nonlinear frequency shift for both BGK and pumped EPWs basically coincide, whereas for higher amplitudes it changes its scaling for BGK modes while staying $\propto \sqrt{\phi_{eq}}$ for weakly pumped EPWs.

The maximum growth rate γ^{max} (the maximum vs. k_x for each fixed ϕ_{eq}) as a function of ϕ_{eq} is shown in Fig. 6.16 together with the theoretical predictions given by $\gamma^{max} \approx |\Delta\omega^{NUM}|/4$ from Eq. (5.11). We see that growth rates coincide for a wide range of amplitudes up to $\phi_{eq} < 0.5$ despite the growing difference in the nonlinear frequency shift between these two kinds of waves in Fig. 6.15 (e.g. at $\phi_{eq} = 0.5$, the BGK mode nonlinear frequency shift is twice larger than for BGK-like pumped EPW).

The wavenumber k_x^{max} at which the growth rate is maximum as a function of ϕ_{eq} is shown in Fig. 6.17 together with the theoretical predictions given by $k_x^{max} \approx$

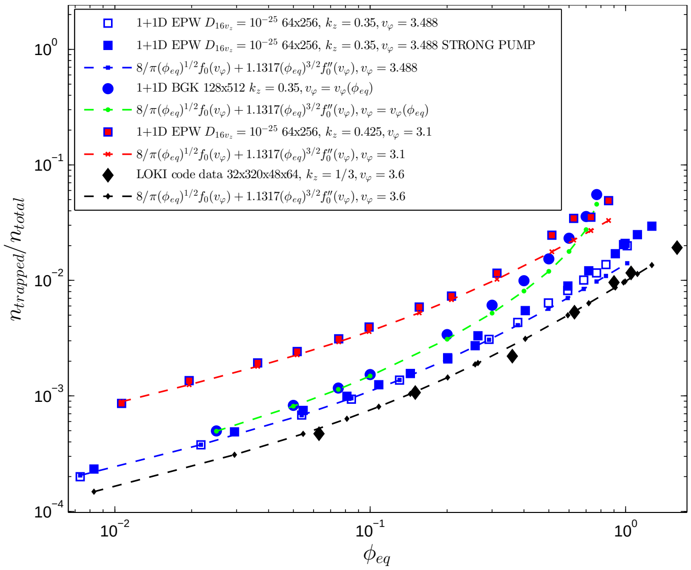

Figure 6.18: The fraction of trapped particles $n_{trapped}/n_{total}$ as a function of ϕ_{eq} for both BGK modes and pumped EPWs.

$\sqrt{|\Delta\omega^{NUM}|k_z/(2v_g)}$ from Eq. (5.13). We used BGK dispersion relation Eq. (3.15) in Section 3.2 to calculate v_g for the comparison with BGK results and linear LW dispersion to calculate v_g^{LW} for the comparison with pumped EPW results. We see that k_x^{max} for these two classes of waves coincide for the whole range of amplitudes (up to $\phi_{eq} \approx 0.72$) and fit well to $k_x^{max} = 0.1\sqrt{\phi_{eq}}$ law despite quite a big discrepancy with theoretical predictions.

These results suggest that the nonlinear frequency shift $\Delta\omega$ or the amplitude ϕ_{eq} are not sufficient to fully characterize the transverse instability of BGK and BGK-like modes. Perhaps the details of the phase space distribution function f behaviour in the trapping region have to be taken into account which is however beyond the scope of this work.

We also compared in Fig. 6.18 the fraction of trapped particles $n_{trapped}/n_{total}$ for all simulation data we obtained (marked with squares for the pumped EPWs with $k_z = 0.35$ and $k_z = 0.425$, circles for the BGK modes with $k_z = 0.35$, and

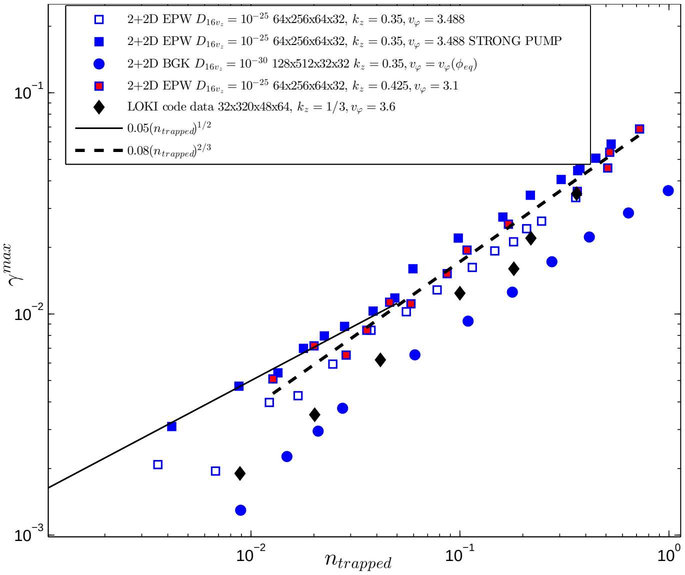

Figure 6.19: The maximum growth rate as a function of $n_{trapped}$ for both BGK modes and pumped EPWs.

diamonds for the LOKI code data from Refs.[31],[42] for EPWs with $k_z = 1/3$) with the theoretical prediction from Ref. [2] (dashed lines with the corresponding markers):

$$
\begin{aligned}
\frac{n_{trapped}}{n_{total}} &\approx \frac{8}{\pi}(\phi_{eq})^{1/2} f_0(v_\varphi) + 1.1317(\phi_{eq})^{3/2} f_0''(v_\varphi), \\
n_{trapped} &= \iint\limits_{W<\Phi_{max}} f(z, v_z)\, dv_z dz, \\
n_{total} &= \iint f(z, v_z)\, dv_z dz = L_z = \frac{2\pi}{k_z}.
\end{aligned}
\tag{6.1}
$$

It was derived for the BGK modes as in Chapter 3 but we found it to work really well for pumped EPWs also. Here f_0 is defined in Eq. (5.2). Eqs. (6.1) take into account not only the leading order term $(\phi_{eq})^{1/2}$ approximation but the next order term $(\phi_{eq})^{3/2}$) as well. One can see in Fig. 6.18 that the data are within 10% from the corresponding theoretical curves for all of our simulation with $\phi_{eq} \lesssim 0.3$. Also EPWs with $k_z = 0.35$ obtained using the strong pump exhibit $\approx 10\%$ higher values of

$n_{trapped}$ compared to EPWs obtained using weak pump. Notice that the EPW results with $k_z = 0.35$ converge to the BGK results with $k_z = 0.35$ in the limit $\phi_{eq} \to 0$ as expected since the BGK waves were constructed as a finite-amplitude bifurcation of the linear LW. For pumped EPWs, $n_{trapped}$ was calculated numerically from 1D+1V simulations some time after the pump was switched off (typically $t = 1000$). As EPW evolved in our simulations between $t = T_{off}$ and $t = 1000$, then $n_{trapped}$ would typically decreased only by $1-2\%$ due to numerical effects. For BGK modes, $n_{trapped}$ was calculated numerically after constructing 1D+1V BGK solution analytically (no evolution). Also note that for the pumped EPW, v_φ is the same (and given by LW dispersion relation) in all simulations with a particular k_z, while for BGK modes, $v_\varphi = v_\varphi(\phi_{eq})$ according to the dispersion relation given by Eq. (3.15) in Section 3.2. We have not included into Fig. 6.18 the number of trapped particles for BGK modes obtained on a smaller resolution (64x256) as in Section 3.1 since the difference in $n_{trapped}$ values was less than 1%.

Also Fig. 6.19 shows the maximum growth rate γ^{max} as a function of $n_{trapped}$ for both BGK modes and pumped EPWs. Even though it is hard to conclude anything regarding the scaling for the simulations with small amplitudes (left side of the graph) due to the larger numerical errors for γ^{max} in these simulations, it appears that the dependance γ^{max} on $n_{trapped}$ has somewhat more universal scaling for higher amplitudes (close to $\gamma^{max} \propto (n_{trapped})^{2/3}$) compared to the dependance γ^{max} on ϕ_{eq} in Figs. 6.10, 6.13 and 6.16, where the scaling changes from $\gamma^{max} \propto \sqrt{\phi_{eq}}$ to $\gamma^{max} \propto \phi_{eq}$.

Chapter 7

Conclusion And Discussion

We studied the linear Langmuir wave (LW) filamentation instability of a particular family of BGK modes that bifurcates from a linear periodic Langmuir wave for $k\lambda_D = 0.35$. These BGK modes approximate the nonlinear electron plasma wave resulting from adiabatically slow pumping by SRS. The construction process of these BGK modes is described in detail. Performing direct 2D+2V Vlasov-Poisson simulations of collisionless plasma we found that the maximal growth rates from simulations are $30 - 70\%$ smaller compared to the theoretical prediction but exhibit the proper scaling for small amplitudes of BGK wave $\gamma^{max} \propto \sqrt{\phi_{eq}}$ while $k_x^{max} \propto \sqrt{\phi_{eq}}$. These results await an improved theory since current theory predicts $k_x^{max} \propto (\phi_{eq})^{1/4}$.

We also studied the filamentation instability of electron plasma wave (EPWs) obtained by pumping of the system by external electric potential. Weak and strong pumps were considered and compared. Performing direct 2D+2V Vlasov-Poisson simulations of collisionless plasma we found that the maximal growth rates γ^{max} for weakly pumped EPWs are within $20 - 30\%$ from the theoretical prediction for small amplitudes ($\phi_{eq} < 0.2$) both for $k_z = 0.35$ and $k_z = 0.425$. Strongly pumped LWs have higher filamentation grow rates (by 30 50% compared to weakly pumped) even though their nonlinear frequency shift essentially coincide. γ^{max} for both types of pumping exhibits the proper scaling for small amplitudes of EPWs $\gamma^{max} \propto \sqrt{\phi_{eq}}$ while $k_x^{max} \propto \sqrt{\phi_{eq}}$ result remains to be explained theoretically. Also it appears that the scaling $\gamma^{max} \propto (n_{trapped})^{2/3}$ might be somewhat more universal among pumped EPWs and BGK modes with various k_z and amplitudes ϕ_{eq}.

We found that both BGK modes and weakly pumped BGK-like modes have the same transverse instability growth rates for $k_z = 0.35$ and peaked at the same wavenumber $k_x = k_x^{max}$ even though the electron phase space distribution function $f(z, v_z, t)$ is not the same for these solutions as shown in Fig. 5.3. It suggests the universal mechanism for the kinetic saturation of stimulated Raman scatter in laser-plasma interaction experiments.

In the nonlinear stage of filamentation LW wave is found to self-focus and forms a pattern of bright spots (as seen in Figs. 4.4 and 6.2) which later defocus and turns into a turbulent picture. This behavior contrasts strongly with LW propagation [19] in the "fluid" regime, $k\lambda_D \lesssim 0.2$, in which both two-dimensional (2D) and three-dimensional (3D) collapse [59, 60, 27] may occur if we take into account ion dynamics. As shown in Ref. [4], the transition from the fluid to the regime where the trapped electron effects cannot be ignored occurs at $k\lambda_D \sim 0.2$. Thus at $k\lambda_D \gtrsim 0.2$. LW frequency reduction due to electron trapping may dominate [4] the ponderomotive [19] frequency shift [28, 25] with $\triangle\omega \propto |E|^2$. Contrary to the result of Ref. [28] where fluid nonlinearity frequency shift $\Delta\omega_{fluid}$ is shown to be positive via use of water bag distribution of electrons, the result of Ref. [25] indicates that $\Delta\omega_{fluid}$ can have either sign depending on k, for example in case of Maxwellian distribution. Refs. [28] and [25] suggest that kinetic effects might dominate fluid effects even for large amplitudes of LW if $k\lambda_D > 0.3$. Though the trapped electron frequency shift, perturbatively, varies as $|E|^{1/2}$ [23, 21, 24], and therefore cannot lead to LW collapse [59, 60, 27], 3D PIC simulation results [32] have been interpreted as showing that the trapped electron LW filamentation instability can saturate [33] stimulated Raman back-scatter (SRS) [1] by reducing the LWs coherence.

Since experimental data in the kinetic LW regime is at best qualitative and indirect, such as furnished by observations of SRS light, first principle Vlasov simulations and theory appear to be the chief tools for analyzing LW properties in the kinetic regime. Because LW filamentation is a multi-dimensional effect, with qualitatively different [33] 2D versus 3D nonlinear behavior, analysis via Vlasov numerical solutions will remain an outstanding challenge.

Future work in this area might include:

- Improving the theory of LW filamentation instability
- Exploring what classes of BGKs are dynamically accessible
- Exploring longitudinal stability of various BGK modes
- Developing 3D+3V Vlasov-Poisson and 3D+3V Vlasov-Maxwell code with adaptive mesh refinement to simulate the reduction of SRS due to LW filamentation
- Studying plasma turbulence (nonlinear stage of instability development)
- Including collisions of particles into the model

Appendix A

Numerical Method of Solving Vlasov-Poisson System

Here we describe numerical methods used for simulations in 4 and 6. First, we describe general Split-Step numerical method for time integration, and then we describe it's application to 1D+1V and 2D+2V Vlasov-Poisson Systems as in Chapter 2.

A.1 Split-Step Numerical Method

Suppose we know initial condition $f(t=0)$ and we want to numerically integrate in time up to $t = t_{final}$ the following differential equation:

$$\frac{\partial f}{\partial t} = \hat{A}f + \hat{B}f, \tag{A.1}$$

where $\hat{A}$ and $\hat{B}$ are some operators acting on function f and we know how to compute $\hat{A}f$ and $\hat{B}f$.

Partition the whole interval $0 \leqslant t \leqslant t_{final}$ into N^t equal intervals Δt. We need to determine how do we obtain a solution $f(t+\Delta t)$ at time $t+\Delta t$ from a known data $f(t)$ at time t.

We can write a formal exact solution of (A.1) as

$$f^{exact}(t+\Delta t) = e^{\Delta t(\hat{A}+\hat{B})} f(t), \tag{A.2}$$

where

$$\begin{gathered}
e^{\Delta t(\hat{A}+\hat{B})} \equiv 1 + \Delta t(\hat{A}+\hat{B}) + \frac{(\Delta t)^2}{2!}(\hat{A}+\hat{B})^2 + \frac{(\Delta t)^3}{3!}(\hat{A}+\hat{B})^3 + \ldots = \\
1 + \Delta t(\hat{A}+\hat{B}) + \frac{(\Delta t)^2}{2!}(\hat{A}^2 + \hat{A}\hat{B} + \hat{B}\hat{A} + \hat{B}^2) + \\
\frac{(\Delta t)^3}{3!}(\hat{A}^3 + \hat{A}^2\hat{B} + \hat{A}\hat{B}\hat{A} + \hat{B}\hat{A}^2 + \hat{A}\hat{B}^2 + \hat{B}\hat{A}\hat{B} + \hat{B}^2\hat{A} + \hat{B}^3) + \mathcal{O}((\Delta t)^4).
\end{gathered} \tag{A.3}$$

If operators $\hat{A}$ and $\hat{B}$ do not commute then $\hat{A}\hat{B} \neq \hat{B}\hat{A}$, so we cannot simplify expression in (A.3).

Now, instead of (A.1) Eq. consider two equations:

$$\frac{\partial f}{\partial t} = \hat{A} f, \tag{A.4a}$$

$$\frac{\partial f}{\partial t} = \hat{B} f, \tag{A.4b}$$

and write their formal solutions as:

$$\frac{\partial f}{\partial t} = \hat{A} f \longrightarrow f(t+\Delta t) = e^{\Delta t \hat{A}} f(t), \tag{A.5a}$$

$$\frac{\partial f}{\partial t} = \hat{B} f \longrightarrow f(t+\Delta t) = e^{\Delta t \hat{A}} f(t), \tag{A.5b}$$

where

$$e^{\Delta t \hat{A}} \equiv 1 + \Delta t \hat{A} + \frac{(\Delta t)^2}{2!}\hat{A}^2 + \frac{(\Delta t)^3}{3!}\hat{A}^3 + \ldots, \tag{A.6a}$$

$$e^{\Delta t \hat{B}} \equiv 1 + \Delta t \hat{B} + \frac{(\Delta t)^2}{2!}\hat{B}^2 + \frac{(\Delta t)^3}{3!}\hat{B}^3 + \ldots. \tag{A.6b}$$

Combine solution (A.5) of Eqs. (A.4) as follows (**SS1**):

$$f^{SS1}(t+\Delta t) = e^{\Delta t \hat{A}} e^{\Delta t \hat{B}} f(t), \tag{A.7}$$

then using (A.6) we get

$$e^{\Delta t\hat{A}}e^{\Delta t\hat{B}} = (1 + \Delta t\hat{A} + \frac{(\Delta t)^2}{2!}\hat{A}^2 + \mathcal{O}((\Delta t)^3))(1 + \Delta t\hat{B} + \frac{(\Delta t)^2}{2!}\hat{B}^2 + \mathcal{O}((\Delta t)^3)) =$$
$$1 + \Delta t(\hat{A} + \hat{B}) + \frac{(\Delta t)^2}{2!}(\hat{A}^2 + 2\hat{A}\hat{B} + \hat{B}^2) + \mathcal{O}((\Delta t)^3)), \tag{A.8}$$

which differs from (A.3) starting order $(\Delta t)^2$, so

$$f^{SS1}(t + \Delta t) = f^{exact}(t + \Delta t) + \mathcal{O}((\Delta t)^2), \tag{A.9}$$

that means that the local error is of order $(\Delta t)^2$ and the global error (at $t = t_{final}$) is of order Δt making SS1 a method of 1st order.

Now, combine solution (A.5) of Eqs. (A.4) as follows (**SS2 or Strang splitting**):

$$f^{SS2}(t + \Delta t) = e^{\frac{\Delta t}{2}\hat{A}}e^{\Delta t\hat{B}}e^{\frac{\Delta t}{2}\hat{A}}f(t), \tag{A.10}$$

then using (A.6) we get

$$\begin{aligned} e^{\frac{\Delta t}{2}\hat{A}}e^{\Delta t\hat{B}}e^{\frac{\Delta t}{2}\hat{A}} = {} & (1 + \frac{\Delta t}{2}\hat{A} + \frac{(\Delta t)^2}{2^2 2!}\hat{A}^2 + \frac{(\Delta t)^3}{2^3 3!}\hat{A}^3 + \mathcal{O}((\Delta t)^4)) \\ & (1 + \Delta t\hat{B} + \frac{(\Delta t)^2}{2!}\hat{B}^2 + \frac{(\Delta t)^3}{3!}\hat{B}^3 + \mathcal{O}((\Delta t)^4)) \\ & (1 + \frac{\Delta t}{2}\hat{A} + \frac{(\Delta t)^2}{2^2 2!}\hat{A}^2 + \frac{(\Delta t)^3}{2^3 3!}\hat{A}^3 + \mathcal{O}((\Delta t)^4)) = \\ & 1 + \Delta t(\hat{A} + \hat{B}) + \frac{(\Delta t)^2}{2!}(\hat{A}^2 + \hat{A}\hat{B} + \hat{B}\hat{A} + \hat{B}^2) + \\ \frac{(\Delta t)^3}{3!}(\hat{A}^3 + \frac{3}{4}\hat{A}^2\hat{B} + \frac{3}{2}\hat{A}\hat{B}\hat{A} & + \frac{3}{4}\hat{B}\hat{A}^2 + \frac{3}{2}\hat{A}\hat{B}^2 + \frac{3}{2}\hat{B}^2\hat{A} + \hat{B}^3) + \mathcal{O}((\Delta t)^4), \end{aligned} \tag{A.11}$$

which differs from (A.3) starting order $(\Delta t)^3$, so

$$f^{SS2}(t + \Delta t) = f^{exact}(t + \Delta t) + \mathcal{O}((\Delta t)^3), \tag{A.12}$$

that means that the local error is of order $(\Delta t)^3$ and the global error (at $t = t_{final}$) is of order $(\Delta t)^2$ making SS2 a method of 2nd order.

Another method of 2nd order **SS**$2'$ can be obtained by swapping operators $\hat{A}$ and $\hat{B}$ in Eq.(A.10):

$$f^{SS2'}(t+\Delta t) = e^{\frac{\Delta t}{2}\hat{B}} e^{\Delta t \hat{A}} e^{\frac{\Delta t}{2}\hat{B}} f(t). \tag{A.13}$$

Higher orders of Split-Step methods can be constructed [61]. For example, a 4th order Splitting scheme (**SS4**) [61, 62] for Eq. (A.1) is:

$$f^{SS4}(t+\Delta t) = e^{\alpha_4 \Delta t \hat{A}} e^{\beta_3 \Delta t \hat{B}} e^{\alpha_3 \Delta t \hat{A}} e^{\beta_2 \Delta t \hat{B}} e^{\alpha_2 \Delta t \hat{A}} e^{\beta_1 \Delta t \hat{B}} e^{\alpha_1 \Delta t \hat{A}} f(t), \tag{A.14}$$

where $\alpha_1 = \alpha_4 = \frac{w}{2}, \alpha_2 = \alpha_3 = \frac{1-w}{2}, \beta_1 = \beta_3 = w, \beta_2 = 1 - 2w, w = \frac{2+2^{1/3}+2^{-1/3}}{3}$ and

$$f^{SS4}(t+\Delta t) = f^{exact}(t+\Delta t) + \mathcal{O}((\Delta t)^5), \tag{A.15}$$

which can be verified in a similar way as for SS1 and SS2 methods. Note that $w = \frac{2+2^{1/3}+2^{-1/3}}{3} \approx 1.35$, so $\alpha_2 = \alpha_3 \approx -0.175 < 0$ and $\beta_2 \approx -1.7 < 0$.

Methods SS1 and SS2 are unconditionally stable (have no CFL condition on Δt) as long as problems (A.4) are well-posed and we can solve Eqs.(A.4) exactly (that is to compute $e^{\Delta t \hat{A}}$ and $e^{\Delta t \hat{B}}$ exactly) or numerically via unconditionally stable numerical schemes. However, any Split-Step method of order higher than 2 (including SS4 method described here) has "negative time steps" due to negative coefficients α_i and β_i [63, 64, 65, 66]. So any differential operator in $\hat{A}$ or $\hat{B}$ of even order (in hyperbolic PDE or mixed hyperbolic-parabolic PDE) will make problems (A.4) ill-posed during these "negative time steps". But since overall time steps for operators $\hat{A}$ and $\hat{B}$ are positive ($\alpha_1 + \alpha_2 + \alpha_3 + \alpha_4 = 1$ and $\beta_1 + \beta_2 + \beta_3 = 1$) we typically just need to make sure that the fastest growing harmonics in the system don't grow to much during the negative parts of the time stepping, since that growth is going to be compensated by a decay during positive parts of time stepping. This effectively gives a CFL condition on Δt in SS4 method in case of even order differential operators. This issue of constructing unconditionally stable high order Split-Step methods for hyperbolic and hyperbolic-parabolic PDEs could be overcome by using complex-valued coefficients α_i and β_i with positive real parts [67].

Also if Eqs.(A.4) are solvable analytically then the only error of time integration comes from the splitting. Otherwise, in case we need to solve one of the equations (A.4) using conditionally stable method (for example Runge-Kutta method) the overall schemes for SS1 and SS2 becomes conditionally stable, plus we will have an additional contribution to the overall error of the scheme. This might render the splitting not as advantageous and the numerical scheme could turn out to be even less efficient than using, say, Runge-Kutta method for the entire problem. But this is problem dependent and should be checked by a numerical experiment in each particular case.

If one needs to solve

$$\frac{\partial f}{\partial t} = \hat{A}f + \hat{B}f + \hat{C}f, \tag{A.16}$$

one can generalize Split-Step schemes that we considered above by first splitting the right hand side into $\hat{A}f$ and $\hat{B}f + \hat{C}f$ and then splitting $\hat{B}f + \hat{C}f$ into $\hat{B}f$ and $\hat{C}f$. Then for **SS1** we get

$$\begin{aligned} f^{exact}(t+\Delta t) = e^{\Delta t(\hat{A}+\hat{B}+\hat{C})} f(t) \approx \\ e^{\Delta t\hat{A}} e^{\Delta t(\hat{B}+\hat{C})} f(t) \approx \\ e^{\Delta t\hat{A}} e^{\Delta t\hat{B}} e^{\Delta t\hat{C}} f(t) =& f^{SS1}(t+\Delta t), \end{aligned} \tag{A.17}$$

for **SS2** we get

$$\begin{aligned} f^{exact}(t+\Delta t) = e^{\Delta t(\hat{A}+\hat{B}+\hat{C})} f(t) \approx \\ e^{\frac{\Delta t}{2}\hat{A}} e^{\Delta t(\hat{B}+\hat{C})} e^{\frac{\Delta t}{2}\hat{A}} f(t) \approx \\ e^{\frac{\Delta t}{2}\hat{A}} e^{\frac{\Delta t}{2}\hat{B}} e^{\Delta t\hat{C}} e^{\frac{\Delta t}{2}\hat{B}} e^{\frac{\Delta t}{2}\hat{A}} f(t) =& f^{SS2}(t+\Delta t), \end{aligned} \tag{A.18}$$

and for **SS4** we get

$$\begin{aligned} f^{exact}(t+\Delta t) = e^{\Delta t(\hat{A}+\hat{B}+\hat{C})} f(t) \approx \\ e^{\alpha_4 \Delta t \hat{A}} e^{\beta_3 \Delta t(\hat{B}+\hat{C})} e^{\alpha_3 \Delta t \hat{A}} e^{\beta_2 \Delta t(\hat{B}+\hat{C})} e^{\alpha_2 \Delta t \hat{A}} e^{\beta_1 \Delta t(\hat{B}+\hat{C})} e^{\alpha_1 \Delta t \hat{A}} f(t) \approx \\ e^{\alpha_4 \Delta t \hat{A}} e^{\beta_3 \Delta t \hat{BC}} e^{\alpha_3 \Delta t \hat{A}} e^{\beta_2 \Delta t \hat{BC}} e^{\alpha_2 \Delta t \hat{A}} e^{\beta_1 \Delta t \hat{BC}} e^{\alpha_1 \Delta t \hat{A}} f(t) =& f^{SS4}(t+\Delta t), \end{aligned} \tag{A.19}$$

where

$$e^{\gamma \Delta t \hat{BC}} = e^{\gamma \alpha_4 \Delta t \hat{B}} e^{\gamma \beta_3 \Delta t \hat{C}} e^{\gamma \alpha_3 \Delta t \hat{B}} e^{\gamma \beta_2 \Delta t \hat{C}} e^{\gamma \alpha_2 \Delta t \hat{B}} e^{\gamma \beta_1 \Delta t \hat{C}} e^{\gamma \alpha_1 \Delta t \hat{B}}, \quad \gamma = \beta_1, \beta_2, \beta_3, \tag{A.20}$$

with total 25 parts in this SS4 scheme.

Again, interchanging operators $\hat{A}, \hat{B}$ and $\hat{C}$ in Eqs. (A.17)-(A.20) we get different splitting schemes of the corresponding orders. Total error estimates and different computational complexity of computing operators $e^{\Delta t \hat{A}}, e^{\Delta t \hat{B}}$ and $e^{\Delta t \hat{C}}$ make one or the other choice of numerical scheme preferable.

A.2 Split-Step for 1D+1V Vlasov-Poisson System

Consider the simplest 1D+1V Vlasov-Poisson System as in Eqs. (2.1)-(2.5), we rewrite 1D+1V Vlasov equation here:

$$\left\{\frac{\partial}{\partial t} + v_z\frac{\partial}{\partial z} + E_z(z,t)\frac{\partial}{\partial v_z}\right\} f(z,v_z,t) = 0, \tag{A.21}$$

where

$$\begin{aligned}
&E_z(z,t) = E_z^{int}(z,t) + E_z^{ext}(z,t),\\
&E_z^{int}(z,t) = -\frac{\partial\Phi^{int}(z,t)}{\partial z}, \qquad E_z^{ext}(z,t) = -\frac{\partial\Phi^{ext}(z,t)}{\partial z},\\
&\frac{\partial^2\Phi^{int}(z,t)}{\partial z^2} = 1-\rho(z,t),\\
&\rho(z,t) = \int f(z,v_z,t)dv_z.
\end{aligned} \tag{A.22}$$

We split Vlasov equation into two parts, advection:

$$\frac{\partial f}{\partial t} = \hat{A}f, \qquad \hat{A} = -v_z\frac{\partial}{\partial z}, \tag{A.23}$$

and acceleration:

$$\frac{\partial f}{\partial t} = \hat{B}(t)f, \qquad \hat{B}(t) = -E_z(z,t)\frac{\partial}{\partial v_z}. \tag{A.24}$$

Solving Eq. (A.23) for each fixed v_z we formally get

$$f(t+\Delta t) = e^{-\Delta t\hat{A}}f(t), \tag{A.25}$$

where here and further we omit dependance of f on z and v_z for brevity.

In practice, it's easy to compute solution of Eq. (A.23) in Fourier Transformed space with respect to z-direction (k-space) where $\frac{\partial}{\partial z}$ becomes ik and Eq. (A.23) becomes

$$\frac{\partial f_k}{\partial t} = \hat{A}_k f_k, \qquad \hat{A}_k = -v_z ik. \tag{A.26}$$

Solving it we get

$$f_k(t+\Delta t) = e^{\Delta t \hat{A}_k} f_k(t) = e^{-i\Delta t v_z k} f_k(t). \tag{A.27}$$

Matrix $e^{-i\Delta t v_z k}$ is diagonal, corresponds to rotation of phase (since the absolute values of it's entries are ones) and can be precomputed in advance, requiring only $N_z \times N_{v_z}$ multiplication operations to apply, where N_z is number of grid points in z-direction and N_{v_z} is number of grid points in v_z-direction. Also we need $2 \times O(N_z \log(N_z)) \times N_{v_z}$ operations to do FFT and IFFT going to k-space and back.

Solving Eq. (A.24) for each fixed z we formally get

$$f(t+\Delta t) = e^{\Delta t < \hat{B} >} f(t), \qquad \text{where} \qquad < \hat{B} >= -\frac{1}{\Delta t} \int\limits_{t}^{t+\Delta t} E_z(z,\tau) d\tau \frac{\partial}{\partial v_z} \tag{A.28}$$

In practice, it's easy to do so in Fourier Transformed space with respect to v_z-direction (p-space) since $\frac{\partial}{\partial v_z}$ becomes ip and Eq. (A.24)

$$\frac{\partial f_p}{\partial t} = \hat{B}_p(t) f, \qquad \hat{B}_p(t) = -E_z(z,t) ip. \tag{A.29}$$

Solving it we get

$$f_p(t+\Delta t) = e^{\Delta t < \hat{B}_p >} f_p(t) = e^{-i \int\limits_{t}^{t+\Delta t} E_z(z,\tau) d\tau p} f_p(t). \tag{A.30}$$

Matrix $e^{-i \int\limits_{t}^{t+\Delta t} E_z(z,\tau) d\tau p}$ is diagonal, corresponds to rotation of phase but can not be precomputed in advance due to time-dependent $E_z(z,t)$, requiring $C \times N_z \times N_{v_z}$ operations to compute exponential and $N_z \times N_{v_z}$ operations to apply. Also we need $2 \times O(N_{v_z} \log(N_{v_z})) \times N_z$ operations to do FFT and IFFT going to p-space and back.

Integral $\int\limits_{t}^{t+\Delta t} E_z(z,\tau) d\tau$ can be simplified. Recall $E_z(z,\tau) = E_z^{int}(z,\tau) + E_z^{ext}(z,\tau)$ and note that during "acceleration step" E_z^{int} is time-independent since $\rho(z,t) = \int f(z, v_z, t) dv_z$ doesn't change in time as particles are advected strictly along v_z-direction and do not change their position in z-direction so the integral for $\rho(z,t)$ will be the same at each point z and $\rho(z)$ will be time independent, so $\int\limits_{t}^{t+\Delta t} E_z^{int}(z,\tau)d\tau = E_z^{int}(z,t)\Delta t$. And we assume that $\int\limits_{t}^{t+\Delta t} E_z^{ext}(z,\tau)d\tau$ can be precomputed in advance analytically or numerically. So for solution (A.30) we get

$$f_p(t+\Delta t) = e^{-i(E_z^{int}(z,t)\Delta t + \int\limits_{t}^{t+\Delta t} E_z^{ext}(z,\tau)d\tau)p} f_p(t). \tag{A.31}$$

Constructing a 2nd order accurate scheme SS2 we can replace $\int\limits_{t}^{t+\Delta t} E_z^{ext}(z,\tau)d\tau \approx E_z^{ext}(z,t+\frac{\Delta t}{2})\Delta t$ using 2nd order midpoint integration rule (with $\mathcal{O}((\Delta t)^3)$ local error) which will not decrease overall order of the method, so $<\hat{B}> \approx \hat{B}(t+\frac{\Delta t}{2})$.

Following **SS2** scheme in (A.10) we schematically write

$$f^{SS2}(t+\Delta t) = e^{\frac{\Delta t}{2}\hat{A}} e^{\Delta t \hat{B}(t+\frac{\Delta t}{2})} e^{\frac{\Delta t}{2}\hat{A}} f(t). \tag{A.32}$$

Inserting Fourier Transform ($\mathcal{FT}$) and Inverse Fourier Transform ($\mathcal{IFT}$) operators for transforming corresponding spaces (z and v_z) where needed we get

$$f_k^{SS2}(t+\Delta t) = e^{\frac{\Delta t}{2}\hat{A}_k} \mathcal{FT}_z \mathcal{IFT}_{v_z} e^{\Delta t \hat{B}_p(t+\frac{\Delta t}{2})} \mathcal{FT}_{v_z} \mathcal{IFT}_z e^{\frac{\Delta t}{2}\hat{A}_k} f_k(t), \tag{A.33}$$

where we start and finish in k-space and $\hat{B}_p(t+\frac{\Delta t}{2}) = -ipE_z(z,t+\frac{\Delta t}{2})$, where $E_z(z,t+\frac{\Delta t}{2}) = E_z^{int}(z,t+\frac{\Delta t}{2}) + E_z^{ext}(z,t+\frac{\Delta t}{2})$, with $E_z^{int}(z,t+\frac{\Delta t}{2})$ being electrical field computed using the distribution function f^1 that we get after applying the first operator $e^{\frac{\Delta t}{2}\hat{A}_k}$, that is $f^1 = \mathcal{IFT}_z e^{\frac{\Delta t}{2}\hat{A}_k} f_k(t)$. Computation of $E_z^{int}(z,t+\frac{\Delta t}{2})$ takes only $O(N_z \log(N_z))$ operations needed to solve Poisson equation in k-space since $E_z^{int}(z)$ and $\Phi^{int}(z)$ depend only on one variable z, and $\rho(z)$ is known from 0th harmonic in p-space of current $f(z,v_z)$. This amount of operations is negligible compared to $O(N_z \log(N_z)) \times N_{v_z}$ that is needed for Fourier Transform of $f(z,v_z)$.

We chose operators in SS2 scheme above in this order (opposed to swapping $\hat{A}$ and $\hat{B}$) since $e^{\Delta t \hat{B}_p(t+\frac{\Delta t}{2})}$ needs to be computed separately at each time step whereas $e^{\frac{\Delta t}{2}\hat{A}_k}$ can be precomputed once at the beginning.

For one time step using SS2 method we need 4 FFT (2 FFT in z-direction and 2 FFT in v_z-direction) and total computational complexity is $\{3+C+2(O(\log(N_z))+O(\log(N_{v_z})))\}N_zN_{v_z}$. If we combine the last operator $e^{\frac{\Delta t}{2}\hat{A}_k}$ of one time step and the same operator of the next time step while doing several time-steps sequentially we can save $N_z \times N_{v_z}$ operations.

Similarly following **SS4** scheme in (A.14) we schematically write

$$f^{SS4}(t+\Delta t) = e^{\alpha_4\Delta t\hat{A}}e^{\beta_3\Delta t<\hat{B}>^3}e^{\alpha_3\Delta t\hat{A}}e^{\beta_2\Delta t<\hat{B}>^2}e^{\alpha_2\Delta t\hat{A}}e^{\beta_1\Delta t<\hat{B}>^1}e^{\alpha_1\Delta t\hat{A}}f(t), \tag{A.34}$$

or inserting Fourier Transform ($\mathcal{FT}$) and Inverse Fourier Transform ($\mathcal{IFT}$) operators for transforming corresponding spaces (z and v_z) where needed we get

$$\begin{aligned} f_k^{SS4}(t+\Delta t) = e^{\alpha_4\Delta t\hat{A}_k}&\mathcal{FT}_z\mathcal{IFT}_{v_z}e^{\beta_3\Delta t<\hat{B}_p>^3}\mathcal{FT}_{v_z}\mathcal{IFT}_z e^{\alpha_3\Delta t\hat{A}_k}\\ &\mathcal{FT}_z\mathcal{IFT}_{v_z}e^{\beta_2\Delta t<\hat{B}_p>^2}\mathcal{FT}_{v_z}\mathcal{IFT}_z e^{\alpha_2\Delta t\hat{A}_k}\\ &\mathcal{FT}_z\mathcal{IFT}_{v_z}e^{\beta_1\Delta t<\hat{B}_p>^1}\mathcal{FT}_{v_z}\mathcal{IFT}_z e^{\alpha_1\Delta t\hat{A}_k}f_k(t), \end{aligned} \tag{A.35}$$

where we start and finish in k-space and

$$< \hat{B}_p >^1 = -ip\left(E_z^{int1}(z) + \frac{1}{\beta_1\Delta t}\int\limits_{t}^{t+\beta_1\Delta t} E_z^{ext}(z,\tau)d\tau\right),$$

$$< \hat{B}_p >^2 = -ip\left(E_z^{int2}(z) + \frac{1}{\beta_2\Delta t}\int\limits_{t+\beta_1\Delta t}^{t+(\beta_1+\beta_2)\Delta t} E_z^{ext}(z,\tau)d\tau\right),$$

$$< \hat{B}_p >^3 = -ip\left(E_z^{int3}(z) + \frac{1}{\beta_3\Delta t}\int\limits_{t-\beta_3\Delta t}^{t+\Delta t} E_z^{ext}(z,\tau)d\tau\right),$$

with $E_z^{int1}(z)$ being electrical field computed using the distribution function $f^1 = \mathcal{IFT}_z e^{\alpha_1\Delta\hat{A}_k}f_k(t)$, $E_z^{int2}(z)$ being electrical field computed using the distribution function $f^2 = \mathcal{IFT}_z e^{\alpha_2\Delta\hat{A}_k}\mathcal{FT}_z\mathcal{IFT}_{v_z}e^{\beta_1\Delta t<\hat{B}_p>^1}\mathcal{FT}_{v_z}f^1$ and $E_z^{int3}(z)$ being electrical field computed using the distribution function
$f^3 = \mathcal{IFT}_z e^{\alpha_3\Delta\hat{A}_k}\mathcal{FT}_z\mathcal{IFT}_{v_z}e^{\beta_2\Delta t<\hat{B}_p>^2}\mathcal{FT}_{v_z}\mathcal{FT}_{v_z}f^2$.

For one time step using SS4 method we need 12 FFT (6 FFT in z-direction and 6 FFT in v_z-direction) and total computational complexity is $\{7+3C+6(O(\log(N_z))+O(\log(N_{v_z})))\}N_zN_{v_z}$. If we combine the last operator $e^{\alpha_4\Delta\hat{A}_k}$ of one time step and similar operator of the next time step while doing several time-steps sequentially we can save $N_z \times N_{v_z}$ operations.

Now, if we consider 1D+1V Vlasov equation with hyper-viscosity similar to (4.1)

$$\left\{\frac{\partial}{\partial t}+v_z\frac{\partial}{\partial z}+E_z\frac{\partial}{\partial v_z}\right\}f(z,v_z,t)=-D_{16v_z}\frac{\partial^{16}}{\partial v_z^{16}}\left(f-\frac{1}{L_z}\int_0^{L_z}fdz\right), \quad \text{(A.36)}$$

where D_{16v_z} is a small coefficient chosen as small as possible to provide enough decay (down to numerical roundoff levels) of solution spectrum tails in kp-space at all time of simulation.

We can split it 3-ways, adding hyper-viscosity step to Eqs. (A.23) and (A.24):

$$\frac{\partial f}{\partial t}=\hat{C}f=-D_{16v_z}\frac{\partial^{16}}{\partial v_z^{16}}\left(f-\frac{1}{L_z}\int_0^{L_z}fdz\right). \quad \text{(A.37)}$$

As before we can write formal solution of this equation as

$$f(t+\Delta t)=e^{\hat{C}\Delta t}f(t), \quad \text{(A.38)}$$

but this form is not practical.

Transforming Eq. (A.37) with Fourier Transform with respect to z and v_z directions (kp-space) we get

$$\frac{\partial f_{kp}}{\partial t}=\hat{C}_{kp}f_{kp}, \quad \hat{C}_{kp}=\left\{\begin{array}{r}-D_{16v_z}p^{16}, k\neq 0\\ 0, k=0\end{array}\right. =-D_{16v_z}p^{16}I[k], \quad \text{(A.39)}$$

where $I[k]=1, k\neq 0$ and $I[k]=0, k=0$.

Solving Eq. (A.39) we get

$$f_{kp}(t+\Delta t)=e^{-D_{16v_z}p^{16}I[k]\Delta t}f_{kp}(t), \quad \text{(A.40)}$$

which is more practical for computations. Matrix $e^{-D_{16v_z}p^{16}I[k]\Delta t}$ is diagonal, corresponds to damping of harmonics except for harmonics with $k = 0$ and can be precomputed in advance, requiring only $N_z \times N_{v_z}$ multiplication operations to apply in kp-space.

We have chosen to subtract $\frac{1}{L_z}\int_0^{L_z} f dz$ in hyper-viscosity term in Eq. (A.36) to make sure we don't damp anything in $k = 0$ harmonics, since these harmonics carry most of the kinetic energy. Turned out that in most cases this is only marginally different from subtracting $\frac{1}{L_z}\int_0^{L_z} f(z, v_z, t = 0)dz$ which in all of our simulations is Maxwellian distribution $f_0(z, v_z) = \frac{exp(-v_z^2/2)}{\sqrt{2\pi}}$ or not subtracting anything at all. In both of these cases hyper-viscosity term can be solved exactly together with acceleration term in p-space so there is no need for 3-way splitting (in the latter case we only need to replace $\hat{B}_p(t) = -iE_z(z, t)p$ by $\hat{B}_p(t) = -iE_z(z, t)p - D_{16v_z}p^{16}$). Anyway, we proceed with the chosen form of Eq. (A.36).

According to Eq. (A.18) we can schematically write **SS2** scheme:

$$f^{SS2}(t + \Delta t) = e^{\frac{\Delta t}{2}\hat{A}} e^{\frac{\Delta t}{2}\hat{C}} e^{\Delta t\hat{B}(t+\frac{\Delta t}{2})} e^{\frac{\Delta t}{2}\hat{C}} e^{\frac{\Delta t}{2}\hat{A}} f(t). \tag{A.41}$$

Inserting Fourier Transform ($\mathcal{FT}$) and Inverse Fourier Transform ($\mathcal{IFT}$) operators for transforming corresponding spaces (z and v_z) where needed we get

$$f_k^{SS2}(t + \Delta t) = e^{\frac{\Delta t}{2}\hat{A}_k} \mathcal{IFT}_{v_z} e^{\frac{\Delta t}{2}\hat{C}_{kp}} \mathcal{FT}_z e^{\Delta t\hat{B}_p(t+\frac{\Delta t}{2})} \mathcal{IFT}_z e^{\frac{\Delta t}{2}\hat{C}_{kp}} \mathcal{FT}_{v_z} e^{\frac{\Delta t}{2}\hat{A}_k} f_k(t), \tag{A.42}$$

where we start and finish in k-space and $\hat{B}_p(t + \frac{\Delta t}{2}) = -ipE_z(z, t + \frac{\Delta t}{2})$, where $E_z(z, t + \frac{\Delta t}{2}) = E_z^{int}(z, t + \frac{\Delta t}{2}) + E_z^{ext}(z, t + \frac{\Delta t}{2})$, with $E_z^{int}(z, t + \frac{\Delta t}{2})$ being electrical field computed using the distribution function $f_{kp}^1 = e^{\frac{\Delta t}{2}\hat{C}_{kp}} \mathcal{FT}_{v_z} e^{\frac{\Delta t}{2}\hat{A}_k} f_k(t)$ or $f_{kp}^{1\prime} = \mathcal{FT}_{v_z} e^{\frac{\Delta t}{2}\hat{A}_k} f_k(t)$ since operator $e^{\frac{\Delta t}{2}\hat{C}_{kp}}$ does not affect $\rho(z)$ and therefore does not affect $E_z^{int}(z)$.

Similarly to SS2 scheme (A.33), for one time step we need 4 FFT (2 FFT in z-direction and 2 FFT in v_z-direction) and total computational complexity is $\{5 + C +$

$2(O(\log(N_z)) + O(\log(N_{v_z})))\}N_zN_{v_z}$ with only additional $2N_zN_{v_z}$ operations needed to multiply by precomputed diagonal matrix $e^{\frac{\Delta t}{2}\hat{C}_{kp}}$ twice in (A.42). We can save $N_z \times N_{v_z}$ operations by combining the last operator of one time step with $\hat{A}_k$ and the same operator of the next time step while doing several time-steps sequentially.

To construct **SS4** method using 3-way splitting similar to (A.19) we schematically write

$$f^{SS4}(t+\Delta t) = e^{\alpha_4\Delta t\hat{A}}e^{\beta_3\Delta t(<\hat{B}>^3+\hat{C})}e^{\alpha_3\Delta t\hat{A}}e^{\beta_2\Delta t(<\hat{B}>^2+\hat{C})}e^{\alpha_2\Delta t\hat{A}}e^{\beta_1\Delta t(<\hat{B}>^1+\hat{C})}e^{\alpha_1\Delta t\hat{A}}f(t),$$

where in order to have 4th order method we must represent $e^{\beta_j\Delta t(<\hat{B}>^j+\hat{C})}$ for each $j = 1, 2, 3$ using 4th order splitting similar to (A.20) which will make the total number of substeps equal 25. Instead of that, in case when the coefficient D_{16v_z} in operator $\hat{C}$ is very small, we can represent $e^{\beta_j\Delta t(<\hat{B}>^j+\hat{C})} = e^{\frac{\beta_j}{2}\Delta t\hat{C}}e^{\beta_j\Delta t<\hat{B}>^j}e^{\frac{\beta_j}{2}\Delta t\hat{C}}$ using 2nd order splitting similar to (A.10) which will reduce the total number of operations (13 substeps vs. 25 substeps), will make implementation of the method easier, but will provide effectively 4th order method for all practical Δt (see results of numerical simulations below), so we get **SS4-2** method as follows:

$$\begin{aligned} f^{SS4-2}(t+\Delta t) = {} & e^{\alpha_4\Delta t\hat{A}}e^{\frac{\beta_3}{2}\Delta t\hat{C}}e^{\beta_3\Delta t<\hat{B}>^3}e^{\frac{\beta_3}{2}\Delta t\hat{C}} \\ & e^{\alpha_3\Delta t\hat{A}}e^{\frac{\beta_2}{2}\Delta t\hat{C}}e^{\beta_2\Delta t<\hat{B}>^2}e^{\frac{\beta_2}{2}\Delta t\hat{C}} \\ & e^{\alpha_2\Delta t\hat{A}}e^{\frac{\beta_1}{2}\Delta t\hat{C}}e^{\beta_1\Delta t<\hat{B}>^1}e^{\frac{\beta_1}{2}\Delta t\hat{C}}e^{\alpha_1\Delta t\hat{A}}f(t), \end{aligned} \tag{A.43}$$

or inserting Fourier Transform ($\mathcal{FT}$) and Inverse Fourier Transform ($\mathcal{IFT}$) operators for transforming corresponding spaces (z and v_z) where needed we get

$$\begin{aligned} f_k^{SS4-2}(t+\Delta t) = {} & e^{\alpha_4\Delta t\hat{A}_k}\mathcal{IFT}_{v_z}e^{\frac{\beta_3}{2}\Delta t\hat{C}_{kp}}\mathcal{FT}_z e^{\beta_3\Delta t<\hat{B}_p>^3}\mathcal{IFT}_z e^{\frac{\beta_3}{2}\Delta t\hat{C}_{kp}} \\ & \mathcal{FT}_{v_z}e^{\alpha_3\Delta t\hat{A}_k}\mathcal{IFT}_{v_z}e^{\frac{\beta_2}{2}\Delta t\hat{C}_{kp}}\mathcal{FT}_z e^{\beta_2\Delta t<\hat{B}_p>^2}\mathcal{IFT}_z e^{\frac{\beta_2}{2}\Delta t\hat{C}_{kp}} \\ & \mathcal{FT}_{v_z}e^{\alpha_2\Delta t\hat{A}_k}\mathcal{IFT}_{v_z}e^{\frac{\beta_1}{2}\Delta t\hat{C}_{kp}}\mathcal{FT}_z e^{\beta_1\Delta t<\hat{B}_p>^1}\mathcal{IFT}_z e^{\frac{\beta_1}{2}\Delta t\hat{C}_{kp}} \\ & \mathcal{FT}_{v_z}e^{\alpha_1\Delta t\hat{A}_k}f_k(t), \end{aligned} \tag{A.44}$$

where we start and finish in k-space and $<\hat{B}_p>^j$, $j = 1, 2, 3$ are as before

$$<\hat{B}_p>^1 = -ip\left(E_z^{int1}(z) + \frac{1}{\beta_1\Delta t}\int_{t}^{t+\beta_1\Delta t} E_z^{ext}(z,\tau)d\tau\right),$$

$$<\hat{B}_p>^2 = -ip\left(E_z^{int2}(z) + \frac{1}{\beta_2\Delta t}\int_{t+\beta_1\Delta t}^{t+(\beta_1+\beta_2)\Delta t} E_z^{ext}(z,\tau)d\tau\right),$$

$$<\hat{B}_p>^3 = -ip\left(E_z^{int3}(z) + \frac{1}{\beta_3\Delta t}\int_{t-\beta_3\Delta t}^{t+\Delta t} E_z^{ext}(z,\tau)d\tau\right),$$

with $E_z^{int1}(z)$ being electrical field computed using the distribution function $f_k^1 = e^{\alpha_1\Delta\hat{A}_k}f_k(t)$, $E_z^{int2}(z)$ being electrical field computed using the distribution function $f_k^2 = e^{\alpha_2\Delta t\hat{A}_k}\mathcal{IFT}_{v_z}e^{\frac{\beta_1}{2}\Delta t\hat{C}_{kp}}\mathcal{FT}_z e^{\beta_1\Delta t<\hat{B}_p>^1}\mathcal{IFT}_z e^{\frac{\beta_1}{2}\Delta t\hat{C}_{kp}}\mathcal{FT}_{v_z}f_k^1$ and $E_z^{int3}(z)$ being electrical field computed using the distribution function $f_k^3 = e^{\alpha_3\Delta t\hat{A}_k}\mathcal{IFT}_{v_z}e^{\frac{\beta_2}{2}\Delta t\hat{C}_{kp}}\mathcal{FT}_z e^{\beta_2\Delta t<\hat{B}_p>^2}\mathcal{IFT}_z e^{\frac{\beta_2}{2}\Delta t\hat{C}_{kp}}\mathcal{FT}_{v_z}f_k^2$.

For one time step using SS4-2 method we need 12 FFT (6 FFT in z-direction and 6 FFT in v_z-direction) and total computational complexity is $\{10+3C+6(O(\log(N_z))+O(\log(N_{v_z})))\}N_zN_{v_z}$.

Since SS4-2 method has "negative time steps" to make sure that harmonics of solution $f(z, v_z)$ don't grow to fast during time steps involving $e^{-\Delta t\hat{C}_{kp}}$ kind of operators we impose weak analog of CFL condition

$$e^{\Delta t D_{16v_z}p_{max}^{16}} < 10^p, \tag{A.45}$$

where p is approximately number of orders of magnitude that we allow numerical round-off errors to increase by due to instability of high p-harmonics. Rewriting (A.45) and using $p_{max} = \frac{\pi}{\Delta v_z}$ we get

$$\Delta t < \frac{p\log(10)}{D_{16v_z}}(\frac{\Delta v_z}{\pi})^{16} \tag{A.46}$$

We call it weak CFL condition since it's not sharp, and p in the right hand side of (A.45) and (A.46) can be chosen from 1 to 16 depending on what level of error is acceptable for us.

Now we compare SS2 and SS4-2 methods given by Eqs. (A.42) and (A.44) respectively by solving numerically Eqs. (A.36) and (A.22) until $t_{final} = 1$ with initial condition $f(z, v_z, t = 0) = (1 + 0.3\cos(k_z z))\frac{exp(-v_z^2/2)}{\sqrt{2\pi}}$ and periodic B.C. in z-direction with period $L_z = 2\pi/k$ with $k = 0.35$ and periodic B.C. in v_z-direction with $v_z^{max} = 12$ so that $f(z, v_z = v_z^{max}, t) < 10^{-16}$ for $0 \leqslant t \leqslant t_{final}$. We use N_z=256, $N_{v_z} = 512$ grid points, $D_{4v} = 10^{-6}$ (we used hyper-viscosity of 4th order for these tests, all the analysis is the same in this case) and various Δt ranging from 0.5 down to $5 \cdot 10^{-5}$. The analog of CFL condition for SS4-2 method similar to Eq. (A.46) with p=8 is $\Delta t < \frac{p\log(10)}{D_{4v_z}}(\frac{\Delta v_z}{\pi})^4 \approx 0.9$. We compare these results to numerical solutions of Eqs. (A.36) and (A.22) obtained by standard Runge-Kutta methods of
2nd order (**RK2**):

$$\begin{aligned}
&k_1 = \{\hat{A} + \hat{B}(t) + \hat{C}\}f(t),\\
&k_2 = \{\hat{A} + \hat{B}(t + \Delta t) + \hat{C}\}(f(t) + \Delta t k_1),\\
&f(t + \Delta t) = \frac{\Delta t}{2}(k_1 + k_2),
\end{aligned} \tag{A.47}$$

and 4th order (**RK4**):

$$\begin{aligned}
&k_1 = \{\hat{A} + \hat{B}(t) + \hat{C}\}f(t),\\
&k_2 = \{\hat{A} + \hat{B}(t + \frac{\Delta t}{2}) + \hat{C}\}(f(t) + \frac{\Delta t}{2}k_1),\\
&k_3 = \{\hat{A} + \hat{B}(t + \frac{\Delta t}{2}) + \hat{C}\}(f(t) + \frac{\Delta t}{2}k_2),\\
&k_4 = \{\hat{A} + \hat{B}(t + \Delta t) + \hat{C}\}(f(t) + \Delta t k_3),\\
&f(t + \Delta t) = \frac{\Delta t}{6}(k_1 + 2k_2 + 2k_3 + k_4).
\end{aligned} \tag{A.48}$$

Figures A.1 and A.2 show convergence of relative error of $\max_z \Phi(z, t = 1)$ vs. Δt, relative error of f in $L2$ and L_{inf} norms vs. Δt and relative error of $Evergy(t = 1)$

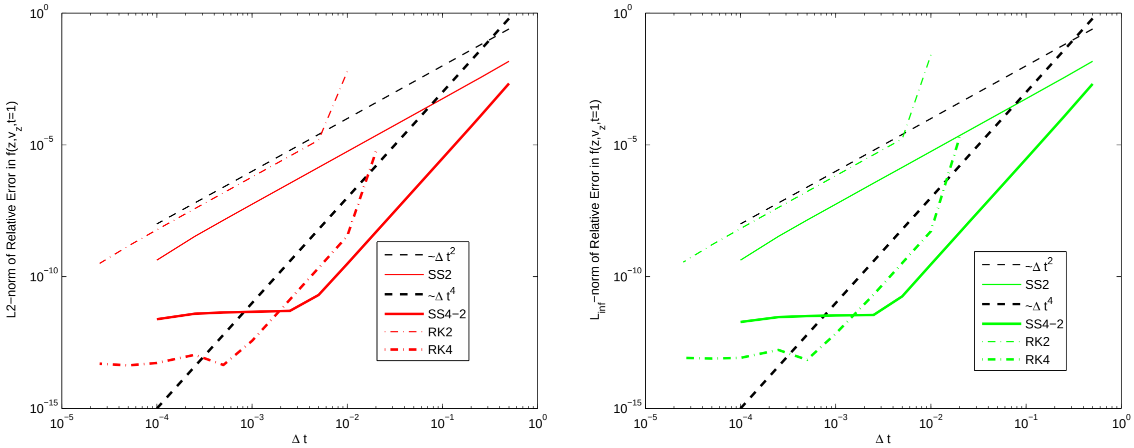

(a) $L2$ norm of relative error in $f(z, v_z, t = 1)$ vs. Δt

(b) L_{inf} norm of relative error in $f(z, v_z, t = 1)$ vs. Δt

Figure A.1: Convergence of relative error of $f(z, v_z, t = 1)$ vs. Δt.

vs. Δt, where $Energy(t) = \frac{1}{2}\int\int v_z^2 f(z, v_z, t)dv_z dz + \frac{1}{2}\int |E_z(z, t)|^2 dz$, for all four methods (SS2, SS4-2, RK2 and RK4). One can see from the graphs that SS2 method gives smaller error than RK2 method and SS4-2 method gives smaller error than RK4

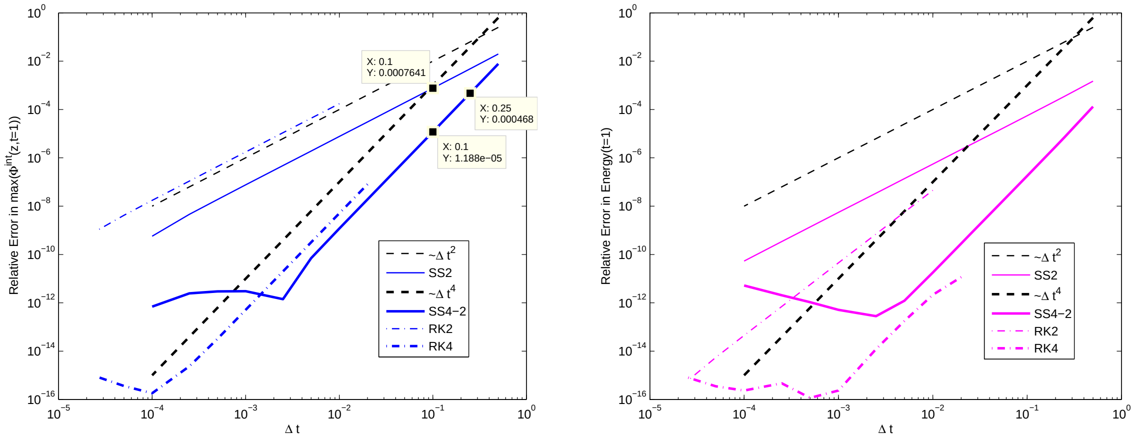

(a) Relative error in $\max_{z} \Phi(z, t = 1)$ vs. Δt

(b) Relative error in $Evergy(t = 1)$ vs. Δt

Figure A.2: Convergence of relative errors vs. Δt.

method everywhere except for errors in $Energy(t)$. Also notice that RK2 and RK4 methods starting from small values of Δt represent their restrictive CFL condition on Δt for stability, $\Delta t \lesssim \frac{dz}{v_z^{max}} \approx 0.023$.

RK4 method needs 4 FFTs for every calculation of the right hand side of Es. (A.36) or 16 FFTs total for every time step. Similarly, RK2 method needs 8 FFTs total for every time step. Experiments confirmed that SS4-2 method (A.44) (with 12 FFTs per time step) turned out to be approximately ×1.5 faster than RK4 method (A.48), while SS2 method (A.42)(with 4 FFTs per time step) approximately ×3 faster than SS4 method, which was expected from FFT count. Figure A.2(a) shows relative error in $\max\limits_z \Phi(z, t = 1)$ for $\Delta t = 0.25$ selected for SS4 and $\Delta t = 0.1$ selected for SS2 showing similar errors for these two cases while computational time was about the same for both of these simulations. This level of error in time integration for SS2 with $\Delta t = 0.1$ was satisfactory for most of our simulation in Chapters 4 and 6, so we chose SS2 for 2D+2V simulations since SS2 method was easier to implement and is unconditionally stable. If one needed much lower error in time integration SS4 method would probably be a better choice then.

There are many conservation laws in Vlasov equation with periodic B.C. in z and v_z (alternatively decaying B.C. in v_z). In fact, any function of f integrated over the whole phase space is a conserved quantity. One of such conserved quantities is the total number of particles $N_{total} = \int\int f(z, v_z, t) dz dv_z$. It is conserved in the original system (A.21) with periodic B.C. in z and v_z (alternatively decaying B.C. in v_z):

$$\frac{\partial N_{total}}{\partial t} = \int\int \frac{\partial f}{\partial t} dz dv_z = -\int\int v_z \frac{\partial f}{\partial z} dz dv_z - \int\int E(z) \frac{\partial f}{\partial v_z} dz dv_z = 0, \quad (A.49)$$

where we integrated by parts with respect to z in the first integral, integrated by parts with respect to v_z in the second integral and used corresponding B.C. The same is true for Eq. (A.36) with additional hyper-viscosity term with periodic B.C.

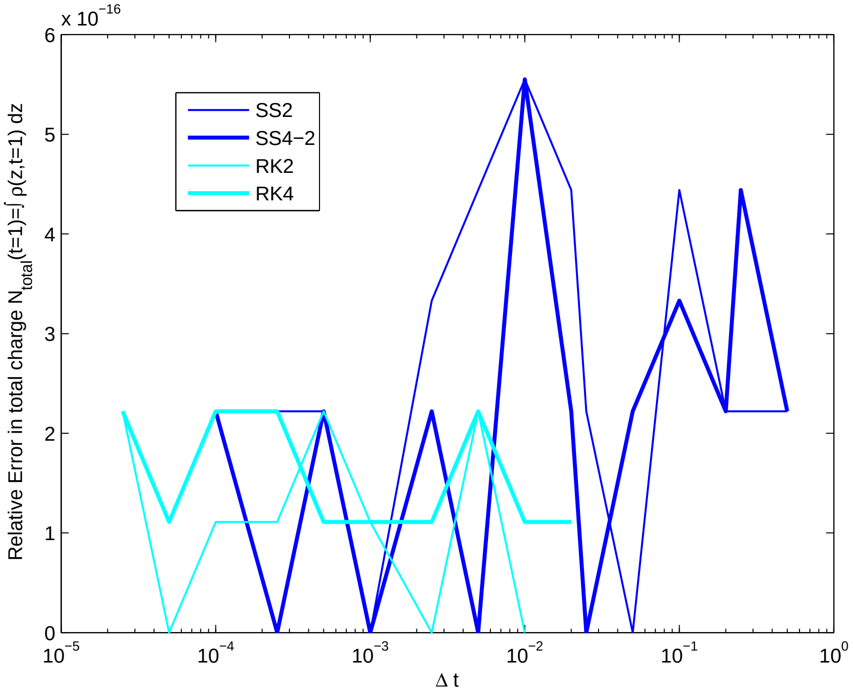

Figure A.3: Relative error in total charge $N_{total}(t=1) = \int \rho(z,t=1)dz$ vs. Δt.

in z and v_z (alternatively decaying B.C. in v_z), since

$$\int\int \frac{\partial^{16}}{\partial v_z^{16}}\left(f - \frac{1}{L_z}\int_0^{L_z} f dz\right) dz dv_z = \int \frac{\partial^{15}}{\partial v_z^{15}}\left(f - \frac{1}{L_z}\int_0^{L_z} f dz\right) dz \Big|_{v_z=-v_z^{max}}^{v_z=v_z^{max}} = 0. \tag{A.50}$$

The total number of particles is also conserved when one of the splitting schemes is used since each substep of the numerical scheme solves Eqs. (A.23),(A.24) or (A.37) each of which preserves the total number of particles. This is demonstrated in Fig. A.3.

A.3 Split-Step for 2D+2V Vlasov-Poisson System

Consider 2D+2V Vlasov equation as in Eq. (4.1)

$$\begin{aligned}\left\{\frac{\partial}{\partial t}+v_z\frac{\partial}{\partial z}+v_x\frac{\partial}{\partial x}+E_z(z,x,t)\frac{\partial}{\partial v_z}+E_x(z,x,t)\frac{\partial}{\partial v_x}\right\}f(z,v_z,x,v_x,t) &= \\ -D_{16v_z}\frac{\partial^{16}}{\partial v_z^{16}}\left(f-\frac{1}{L_z}\int_0^{L_z}f dz\right), &\end{aligned} \tag{A.51}$$

together with Eqs.(2.2)-(2.5) for computing E_z and E_x from f.

Utilizing 5-way splitting and solving each equation in the corresponding Fourier space we get:

$$\frac{\partial f}{\partial t}=-v_x\frac{\partial}{\partial x}f \quad\longrightarrow\quad f_{k_x}(t+\Delta t)=e^{\Delta t\hat{A}1_{k_x}}f_{k_x}(t),\quad \hat{A}1_{k_x}=-v_z ik_x, \tag{A.52}$$

$$\frac{\partial f}{\partial t}=-v_z\frac{\partial}{\partial z}f \quad\longrightarrow\quad f_{k_z}(t+\Delta t)=e^{\Delta t\hat{A}2_{k_z}}f_{k_z}(t),\quad \hat{A}2_{k_z}=-v_z ik_z, \tag{A.53}$$

$$\frac{\partial f}{\partial t}=-E_x(z,x,t)\frac{\partial}{\partial v_x}f\longrightarrow f_{p_x}(t+\Delta t)=e^{\Delta t\hat{B}1_{p_x}}f_{p_x}(t),\quad \hat{B}1_{p_x}=-v_x ip_x, \tag{A.54}$$

$$\frac{\partial f}{\partial t}=-E_z(z,x,t)\frac{\partial}{\partial v_z}f\longrightarrow f_{p_z}(t+\Delta t)=e^{\Delta t\hat{B}2_{p_z}}f_{p_z}(t),\quad \hat{B}2_{p_z}=-v_z ip_z, \tag{A.55}$$

$$\begin{aligned}&\frac{\partial f}{\partial t}=-D_{16v_z}\frac{\partial^{16}}{\partial v_z^{16}}\left(f-\frac{1}{L_z}\int_0^{L_z}f dz\right) \quad\longrightarrow\quad f_{k_zp_z}(t+\Delta t)=e^{\Delta t\hat{C}_{k_zp_z}}f_{k_zp_z}(t),\\ &\hat{C}_{k_zp_z}=\left\{\begin{array}{r}-D_{16v_z}p_z^{16},k_z\neq 0\\ 0,k_z=0\end{array}\right.=-D_{16v_z}p_z^{16}I[k_z],\quad I[k]=\left\{\begin{array}{l}1,k\neq 0\\ 0,k=0\end{array}\right..\end{aligned} \tag{A.56}$$

Generalizing Eq. (A.42) we can schematically write **SS2** scheme:

$$f^{SS2}(t+\Delta t)=e^{\frac{\Delta t}{2}\hat{A}1}e^{\frac{\Delta t}{2}\hat{A}2}e^{\frac{\Delta t}{2}\hat{C}}e^{\frac{\Delta t}{2}\hat{B}1(t+\frac{3}{4}\Delta t)}e^{\Delta t\hat{B}2(t+\frac{\Delta t}{2})}e^{\frac{\Delta t}{2}\hat{B}1(t+\frac{1}{4}\Delta t)}e^{\frac{\Delta t}{2}\hat{C}}e^{\frac{\Delta t}{2}\hat{A}2}e^{\frac{\Delta t}{2}\hat{A}1}f(t). \tag{A.57}$$

Inserting Fourier Transform ($\mathcal{FT}$) and Inverse Fourier Transform ($\mathcal{IFT}$) operators for transforming corresponding spaces (z,x,v_z and v_x) where needed we get

$$\begin{aligned} f^{SS2}_{k_zk_x}(t+\Delta t) =& e^{\frac{\Delta t}{2}\hat{A}1_{k_x}} e^{\frac{\Delta t}{2}\hat{A}2_{k_z}} \mathcal{FT}_x \mathcal{IFT}_{v_z} e^{\frac{\Delta t}{2}\hat{C}_{k_zp_z}} \mathcal{IFT}_{v_x} e^{\frac{\Delta t}{2}\hat{B}1_{p_x}(t+\frac{3}{4}\Delta t)} \\ & \mathcal{FT}_z e^{\Delta t\hat{B}2_{p_z}(t+\frac{\Delta t}{2})} \mathcal{IFT}_z \qquad (A.58) \\ & e^{\frac{\Delta t}{2}\hat{B}1_{p_x}(t+\frac{1}{4}\Delta t)} \mathcal{FT}_{v_x} e^{\frac{\Delta t}{2}\hat{C}_{k_zp_z}} \mathcal{FT}_{v_z} \mathcal{IFT}_x e^{\frac{\Delta t}{2}\hat{A}2_{k_z}} e^{\frac{\Delta t}{2}\hat{A}1_{k_x}} f_{k_zk_x}(t). \end{aligned}$$

where we start and finish in k_zk_x-space and

$$\begin{aligned} \hat{B}1_{p_x}(t+\frac{3}{4}\Delta t) &= -ip_x(E^{int}_x(z,t+\frac{\Delta t}{2}) + E^{ext}_x(z,t+\frac{3}{4}\Delta t)), \\ \hat{B}2_{p_z}(t+\frac{\Delta t}{2}) &= -ip_z(E^{int}_z(z,t+\frac{\Delta t}{2}) + E^{ext}_z(z,t+\frac{\Delta t}{2})), \\ \hat{B}1_{p_x}(t+\frac{1}{4}\Delta t) &= -ip_x(E^{int}_x(z,t+\frac{\Delta t}{2}) + E^{ext}_x(z,t+\frac{1}{4}\Delta t)), \end{aligned}$$

with $E^{int}_z(z,t+\frac{\Delta t}{2})$ being electrical field computed using the distribution function $f^1_{k_zk_x} = e^{\frac{\Delta t}{2}\hat{A}2_{k_z}} e^{\frac{\Delta t}{2}\hat{A}1_{k_x}} f_{k_zk_x}(t)$. Operators with $\hat{C}$, $\hat{B}1$ or $\hat{B}2$ do not affect $\rho(z,x)$ and therefore do not affect E^{int}_z and E^{int}_x, this is why $E^{int}_z(z,t+\frac{\Delta t}{2})$ in $B2_{p_z}(t+\frac{1}{2}\Delta t)$ and $E^{int}_x(z,t+\frac{\Delta t}{2})$ in $B1_{p_x}(t+\frac{1}{4}\Delta t)$ and $B1_{p_x}(t+\frac{3}{4}\Delta t)$ are computed from the same distribution function $f^1_{k_zk_x}$.

For one time step of SS2 scheme in (A.58) we need 8 FFT (2 FFT in x-direction,2 FFT in z-direction, 2 FFT in v_x-direction and 2 FFT in v_z-direction) and total computational complexity is $\{9+3C+2(O(\log(N_z))+O(\log(N_x))+O(\log(N_{v_z}))+O(\log(N_{v_x})))\}N_zN_xN_{v_z}N_{v_x}$.

The numerical scheme described here was used for simulations in Chapter 4 and Chapter 6.

Part II

STOKES WAVE IN HYDRODYNAMICS WITH FREE SURFACE

Chapter 1

Introduction

The problem of hydrodynamics with free surface is a classical problem in fluid dynamics and has been a subject of extensive study for long time. Naturally, applications of this model are often associated with water waves in ocean, water wave turbulence and etc. There are plenty variations of this problem considered in the corresponding literature. Here we focus on one quite particular case of it - Stokes wave, the nonlinear periodic travelling wave on the surface of ideal fluid.

Any ODE/PDE solution can be analyzed form a standpoint of its singularities when it's extended from the real line to the complex plane. While analyzing all possible singularities and scenarios of their evolution in fluid dynamics is a daunting task we start with detailed analysis of Stokes wave singularity and developing tools for such analysis. Therefore this work should be regarded as a first step in a long journey.

Our approach to this problem is largely based on the framework established in the works [68, 69] as well as numerous references focused directly on Stokes waves [70, 71, 8, 72, 73, 74, 75, 76, 77] and general numerical methods described in [78, 79].

This work is immediate continuation of the work started in papers [80, 81, 82] where Stokes wave in two-dimensional potential flow of an ideal incompressible fluid is studied using a conformal mapping of a complex lower half-plane $\mathbb{C}^{-}$ into a domain occupied by fluid. We look at the whole range of Stokes waves, from almost linear to highly nonlinear when nonlinear effects dominate. An advancement is made via use of another conformal map and the main results are published in [83]. Using this improved technique allowed us to numerically obtain Stokes waves extremely close to the limiting Stokes wave, verify parameter oscillations in waves of extreme steepness and improve the estimates for the limiting Stokes wave parameters (steepness and speed) even further. We were also able to capture the position of leading singularity, identify it as a branch cut and study it in detail. Parameter (steepness and speed) oscillations for Stokes wave family as functions of each other and singularity position were obtained and compared to the prediction in [15] as the solutions approached the limiting Stokes wave. A great attention was given to analysis of singularities of the solutions in an efforts to come up with a theoretical foundation and numerical tools for analysis of singularities in hydrodynamics and other problems.

This part of the dissertation is organized as follows. In Chapter 2 most of the relevant well-established theory is given (including equations of motion, conformal mapping, Hamiltonian framework and Stokes wave equation). Chapter 3 describes numerical methods used for calculating Stokes waves. Then in Chapter 4 we describe the earlier results [80, 81, 82] obtained by our group regarding Stokes wave and its singularities. We then describe an improved approach and the new conformal map with details of its implementation (including modifications to Stokes wave equation and numerical method) in Chapter 5.

In Chapter 6 we demonstrate the high efficiency of the new conformal map and analyze new results obtained using this approach. Finally, in Chapter 7 we make conclusions, provide some discussion on future work.

Chapter 2

Derivation of Dynamic and Stokes Wave Equations

2.1 Equations of Motion

In this problem we consider an incompressible 2−dimensional fluid of depth h (and later infinitely deep) that is acted upon by a force of gravity. In physical coordinates

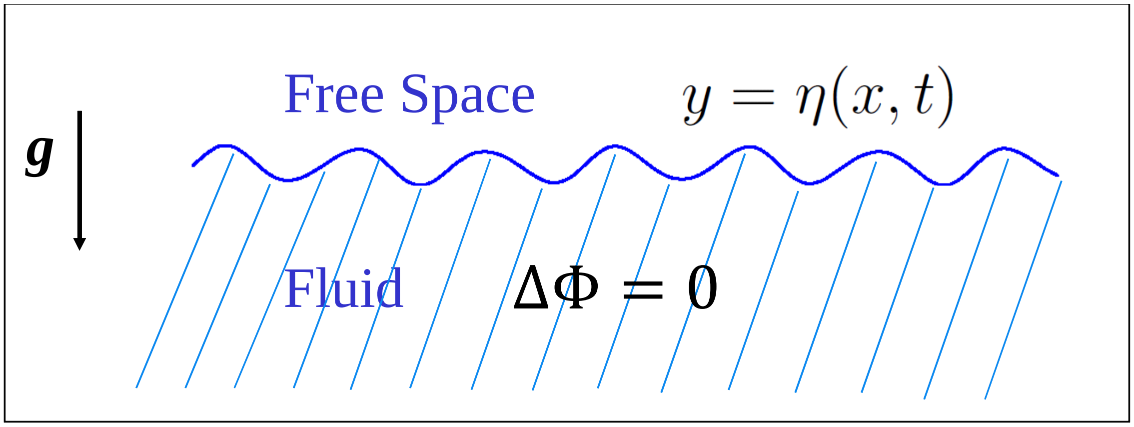

Figure 2.1: Illustration of 2D fluid with free surface.

(x, y) the surface of the fluid, $y = \eta(x,t)$, is a 1-dimensional curve that separates the fluid below and the air above. Here we neglect the pressure of the air on the surface. The flow is assumed to be potential, i.e. the velocity field $\mathbf{v}(x, y, t)$ can be written as a gradient of potential $\Phi(x, y, t)$, $\mathbf{v} = \nabla\Phi$. The incompressibility condition, $\nabla\cdot\mathbf{v} = 0$, then requires $\Delta\Phi = 0$. The tricky part is that the region occupied by fluid as well as boundary conditions are varying in time.

The boundary conditions at the surface $y = \eta(x,t)$ consist of two equations - the statement of the fact that surface is moving with the fluid (kinematic B.C.)

$$\frac{\partial\eta}{\partial t} = \left(-\frac{\partial\eta}{\partial x}\frac{\partial\Phi}{\partial x} + \frac{\partial\Phi}{\partial y}\right)\Big|_{y=\eta(x,t)}, \tag{2.1}$$

and Bernoulli equation, stating the balance of forces at the surface (dynamic B.C.):

$$\frac{\partial\Phi}{\partial t}\Big|_{y=\eta(x,t)} = -\frac{1}{2}\left(\nabla\Phi\right)^2\Big|_{y=\eta(x,t)} - g\eta. \tag{2.2}$$

The boundary condition at the bottom is $\partial_y\Phi|_{y=-h} = 0$ or if the fluid is considered infinitely deep then we use $\Phi|_{y=-\infty} = 0$.

Note, that in order to integrate equations for Φ and η in time one needs the value of normal derivative of Φ at the surface. For that we utilize Dirichlet-Neuman operator that provides the normal derivative $(\nabla\Phi\cdot\mathbf{n})$ given the value of Φ at the surface. The difficulty of the problem is that this operator is nonlocal.

2.2 Conformal Variables and Dirichlet-Neumann Operator

Suppose that the fluid occupies a region that is λ-periodic in x with finite depth h in y direction (similar derivation can be made for infinite domain in x direction).

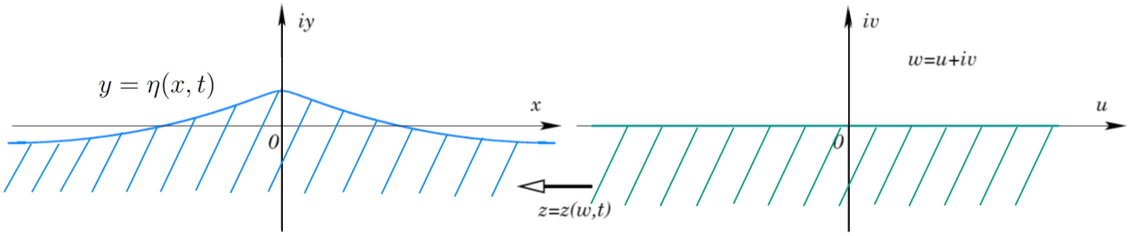

Figure 2.2: Conformal mapping of the lower half-plane $\mathbb{C}^-$ in $w = u + iv$ variables to the region occupied by fluid in physical variables $z(w,t) = x(w,t) + iy(w,t)$.

We introduce a conformal map of the rectangular domain $w = u + iv$, $w \in [-\pi, \pi] \times [-h, 0]$ to the region occupied by fluid $z = x + iy$ [84, 85, 86, 87, 69, 88], $z \in [-\frac{\lambda}{2}, \frac{\lambda}{2}] \times [-h, \eta]$ as on figure 2.2. Because the surface of the fluid η is time-dependent, so is the conformal map $z = z(w,t) = x(w,t) + iy(w,t)$.

The potential $\Phi(z)$ is harmonic $\nabla^2_{x,y}\Phi = 0$ in (x,y) coordinates and since $z(w)$ is conformal, so is $\Phi(z(w))$ in (u,v) coordinates. For notation brevity we redefine $\Phi(w) \equiv \Phi(z(w))$ and

$$\nabla^2_{u,v}\Phi = \partial^2_u\Phi + \partial^2_v\Phi = 0.$$

Suppose we know the potential at the surface $\Phi(x,y,t)|_{y=\eta(x,t)} \equiv \psi(x,t)$ and $\partial_y\Phi|_{y=-h} = 0$. Since the domain in (u,v) coordinates is rectangular we can now solve Laplace equation for $\Phi(u,v)$ with boundary conditions $\Phi(u,v,t)|_{v=0} = \psi(u,t) \equiv \psi(x(u),t)$ and $\partial_v\Phi|_{v=-h} = 0$ much easier than in original coordinates (x,y). Omit the dependance of Φ and ψ on t for a moment.

Since $\Phi(u,v)$ and $\psi(u,v)$ are 2π-periodic function in u direction let's represent them through their Fourier series:

$$\Phi(u,v) = \sum_k \phi_k(v)\exp(iku), \qquad \psi(u) = \sum_k \hat{\psi}_k \exp(iku).$$

Then solving

$$\nabla^2\Phi = \sum_k (\phi_k^{''} - k^2\phi_k)\exp(iku) = 0 \qquad \text{with} \qquad \phi_k(0) = \hat{\psi}_k$$

gives

$$\phi_k(v) = a_k\cosh(kv) + b_k\sinh(kv).$$

But $\partial_v\phi_k = 0$ at $v = -h$, then

$$-ka_k\sinh(kh) + kb_k\cosh(kh) = 0 \qquad \text{or} \qquad b_k = a_k\tanh(kh).$$

So we have:

$$\Phi(u,v) = \sum_k \hat{\psi}_k\left(\cosh(kv) + \tanh(kh)\sinh(kv)\right)\exp(iku). \tag{2.3}$$

Now lets find the harmonic conjugate(stream function) for $\Phi(w)$ and denote it by $\Theta(w)$. By Cauchy-Riemann conditions

$$\Phi_u = \Theta_v,$$
$$\Phi_v = -\Theta_u,$$

we get

$$\Theta(u,v) = \int \Phi_u dv = i\sum_k \hat{\psi}_k(\sinh(kv) + \tanh(kh)\cosh(kv))\exp(iku).$$

At the free surface $v = 0$ this reduces to:

$$\Phi(u,0) = \sum_k \hat{\psi}_k\exp(iku),$$
$$\Theta(u,0) = \sum_k i\tanh(kh)\hat{\psi}_k\exp(iku),$$
$$\Pi(u,0) = \Phi(u,0) + i\left[i\tanh(kh)\right]\Phi(u,0) = \psi + i\hat{R}\psi,$$

where $\hat{R}$ is an operator that multiplies Fourier coefficients by $i\tanh(kh)$ and Π is complex velocity potential.

The problem of finding the appropriate relation between normal derivative $\frac{\partial\Phi}{\partial v}\big|_{v=0}$ and ψ is the essence of Dirichlet-Neumann problem. Here this is done as follows:

$$\left.\frac{\partial\Phi}{\partial v}\right|_{v=0} = -\left.\frac{\partial\Theta}{\partial u}\right|_{v=0} = -\hat{R}\psi_u, \tag{2.4}$$

where operator $-\hat{R}\partial_u$ is the Hilbert-Neumann operator.

Note that in order for any function $f(w)$ to be analytic in $w \in [-\pi,\pi]\times[-h,0]$, the following relation between the real and imaginary parts of f at $v = 0$ has to be satisfied:

$$\begin{aligned} &\mathrm{Im}[f|_{v=0}] = \hat{R}\,\mathrm{Re}[f|_{v=0}],\\ &\qquad\text{or}\\ &\quad f|_{v=0} = \mathrm{Re}[f|_{v=0}] + i\,\mathrm{Im}[f|_{v=0}] = (1+i\hat{R})\mathrm{Re}[f|_{v=0}]. \end{aligned}$$

This statement is a consequence of the uniqueness of solution to the boundary value problem for Laplace equation. Operator inverse to $\hat{R}$ is denoted $\hat{T}$ and is also defined as multiplication in Fourier space. Here we denote Fourier coefficients of a periodic function $f(u)$ as f_k. Then the following relations follow:

$$\begin{aligned} \mathcal{FT}[\hat{R}f] &= R_k f_k = i\tanh(kh) f_k,\\ \mathcal{FT}[\hat{T}f] &= T_k f_k = -i\coth(kh) f_k,\\ \mathcal{FT}[\hat{T}\hat{R}f] &= \mathcal{FT}[\hat{R}\hat{T}f] = f_k, \end{aligned}$$

here $\mathcal{FT}$ denotes Fourier transform. Note that in order for the above relations to work, one has to add an extra restriction on the 0-th Fourier coefficient:

$$f_k = 0 \quad \text{for } k = 0$$

otherwise inverse operator $\hat{T}$ is singular for 0-th Fourier mode.

2.3 Hamiltonian Framework

One of the large advances in this area was made in 1968 by Zakharov [68] who discovered the Hamiltonian structure for free surface hydrodynamics. Here following the works [89, 69] we obtain equations of motion from Hamilton's principle, reformulate our problem in terms of surface variables only and later in terms of the conformal map.

Consider an inviscid potential flow in the presence of gravity, then in physical variables Hamiltonian is simply a sum of kinetic energy and gravity-induced potential energy:

$$H = T + P = \frac{1}{2}\int_{-\lambda/2}^{\lambda/2} dx \int_{-h}^{\eta(x,t)} (\nabla\Phi)^2 dy + \frac{g}{2}\int \eta^2 dx, \tag{2.5}$$

where g is free fall acceleration. The potential energy P is defined by the surface and poses no obstacle to further analysis. But kinetic energy on the other hand involves velocity field in the entire region $D = [-\frac{\lambda}{2}, \frac{\lambda}{2}] \times [-h, \eta]$ occupied by fluid.

It's impossible to express H explicitly in terms of η and ψ, where $\psi(x,t) \equiv \Phi(x, \eta(x,t), t)$ - potential on the free surface of the fluid. But, as it was shown in Ref. [68], the system in hamiltonian one with canonical variables η and ψ and the boundary conditions (2.1)-(2.2) are equivalent to the canonical equations

$$\begin{aligned} \frac{\partial\eta}{\partial t} &= \frac{\delta H}{\delta\psi}, \\ \frac{\partial\psi}{\partial t} &= -\frac{\delta H}{\delta\eta}. \end{aligned}$$

Since we want equations of motion only to involve quantities at the free surface we can rewrite kinetic energy using Green's identity and the fact that $\Delta\Phi = 0$ in D:

$$\begin{aligned}
T &= \frac{1}{2}\iint\limits_{D} (\nabla\Phi)^2 dx\, dy \\
&= \frac{1}{2}\int\limits_{\partial D} \Phi(\nabla\Phi \cdot d\Gamma) - \frac{1}{2}\iint\limits_{D} \Phi\nabla^2\Phi dx\, dy \\
&= \frac{1}{2}\int\limits_{-\lambda/2}^{\lambda/2} \left.(\Phi\Phi_y)\right|_{y=-h} dx + \frac{1}{2}\int\limits_{-h}^{\eta(\lambda/2)} \left.(\Phi\Phi_x)\right|_{x=\lambda/2} dy + \\
&+ \frac{1}{2}\int\limits_{surface} \psi \left.(\nabla\Phi \cdot \mathbf{n})\right|_{y=\eta(x)} d\mathbf{l} - \frac{1}{2}\int\limits_{-h}^{\eta(-\lambda/2)} \left.(\Phi\Phi_x)\right|_{x=-\lambda/2} dy
\end{aligned}$$

The first term is equal to 0 due to the boundary condition at $v = -h$, $\Phi_y|_{y=-h} = 0$, the second and fourth terms cancel out due to periodicity at $x = \pm\frac{\lambda}{2}$ so we get:

$$T = \frac{1}{2}\int\limits_{surface} \left.\psi(\Phi_x dy - \Phi_y dx)\right|_{y=\eta(x)} = \frac{1}{2}\int\limits_{-\pi}^{\pi} \left.\psi(\Phi_x y_u - \Phi_y x_u)\right|_{v=0} du.$$

Expressing Φ_x, Φ_y in terms of Φ_u and Φ_v we find that:

$$T = \frac{1}{2}\int\limits_{-\pi}^{\pi} \psi\Phi_v|_{v=0} du = -\frac{1}{2}\int\limits_{-\pi}^{\pi} \psi\hat{R}\psi_u du$$

by virtue of (2.4), also see Reference [89]. Hence hamiltonian can be written in conformal variables as:

$$H = T + U = -\frac{1}{2}\int \psi\hat{R}\psi_u du + \frac{g}{2}\int y^2 x_u du \tag{2.6}$$

Here we denote $y = y(u,t)$ and $x = u\frac{\lambda}{2\pi} + \tilde{x}(u,t)$ defined by the conformal map such that $\tilde{x}(u,t), y(u,t)$ and correspondingly $\tilde{z}(u,t) = \tilde{x}(u,t) + iy(u,t)$ are 2π - periodic functions with $\tilde{x}(-\pi) = \tilde{x}(\pi) = 0$ while $x(-\pi) = -\frac{\lambda}{2}, x(\pi) = \frac{\lambda}{2}$.

2.4 Deep Water Equations

Now let's take the limit $h \to \infty$. In this limit we consider waves with surface elevations that are much smaller than the depth of domain. This implies that the previously introduced operator $\hat{R}$ and its inverse $\hat{T}$ in Fourier space become:

$$R_k = i \tanh kh \to i \,\mathrm{sign}\, k = H_k, \tag{2.7}$$

$$T_k = i \coth kh \to -i \,\mathrm{sign}\, k = -H_k. \tag{2.8}$$

Here H_k is Fourier transform of the operator $\hat{H}$, a circular Hilbert transform for 2π-periodic function defined as follows:

$$\hat{H} f(u) = \frac{1}{2\pi} \mathrm{p.v.} \int_{-\pi}^{\pi} f(u') \cot\left(\frac{u' - u}{2}\right) du', \tag{2.9}$$

with p.v. designating a Cauchy principal value of integral and that can be easily computed using Fourier transform as $[\hat{H} f]_k = H_k f_k$ using (2.7). The analyticity of $z = x + iy$ and $\tilde{z} = z - u\frac{\lambda}{2\pi} = \tilde{x} + iy$ (periodic part of z) in $\mathbb{C}^-$ implies (see a derivation of Eq. (5.21) e.g. in Ref. [81]) that:

$$y = \hat{H} x \quad \text{and} \quad \tilde{x} = -\hat{H} y. \tag{2.10}$$

The system (2.1)-(2.2) was originally recast into the conformal variables in Ref. [84] and later independently in Ref. [69] taking the following form [69]:

$$y_t x_u - x_t y_u + \hat{H} \psi_u = 0 \tag{2.11}$$

for the kinematic boundary condition and

$$\psi_t y_u - \psi_u y_t + g y y_u = -\hat{H}\left(\psi_t x_u - \psi_u x_t + g y x_u\right) \tag{2.12}$$

for the dynamic boundary condition.

The same equations of motion can also be obtained [69] from extremizing the action

$$S = \int L dt,$$

with the Lagrangian

$$L = \int \psi \frac{\partial \eta}{\partial t} dx - H.$$

As shown in Ref. [69] these equations can be rewritten as evolution equations for complex $z = x + iy$ and ψ:

$$z_t = z_u(\hat{H} - i)\frac{\hat{H}\psi_u}{|z_u|^2}, \tag{2.13a}$$

$$\psi_t + gy = -\frac{(\psi_u + i\hat{H}\psi_u)^2}{2|z_u|^2}. \tag{2.13b}$$

2.5 Stokes Wave Equation

As we mentioned before, a Stokes wave is a periodic nonlinear solution of 2D hydrodynamics equations that propagates with a constant velocity c, i.e.

$$y = \eta(x,t) \equiv \eta(x - ct).$$

The height of Stokes wave is the difference between the surface elevation at the crest and at the trough, however it is more convenient to use a non-dimensionalized parameter H/λ that is a height of Stokes wave H scaled by its wavelength λ. As the scaled wave height H/λ increases from the linear limit $H/\lambda = 0$ to the critical value H_{max}/λ we go from almost linear waves to a strongly nonlinear limiting Stokes wave.

The equation for Stokes wave is found by assuming constant speed of propagation in (2.13):

$$\tilde{z}(u,t) = \tilde{z}(u - ct), \tag{2.14}$$

$$\psi(u,t) = \psi(u - ct), \tag{2.15}$$

where both ψ and $\tilde{z}$ are the periodic functions of their argument. Since $\tilde{z}$ and ψ in (2.14) are both function of $u - ct$ then $\partial_t = c\partial_u$ for them:

$$\partial_t \tilde{x} = c\ \partial_u \tilde{x}, \quad \partial_t y = c\ \partial_u y, \quad \partial_t \psi = c\ \partial_u \psi. \tag{2.16}$$

We transform into the moving frame of reference, $u - ct \to u$, and assume that the crest of the Stokes wave is located at $u = 0$ as in Fig. 2.2. The Stokes solution requires $y(u)$ to be an even function while $\tilde{x}(u)$ needs to be an odd function. Taking into account the periodicity of $\tilde{x}(u)$ in (2.14) it implies that $\tilde{x}(\pm\pi) = 0$.

We make our physical quantities x and y dimensionless by the scaling transform $x = x_{physical}\ 2\pi/\lambda$ and $y = y_{physical}\ 2\pi/\lambda$, then the spatial period of the Stokes solution becomes the same 2π both in x variable (i.e. for $\eta(x - ct)$) and u variable (i.e. for (2.14)), plus

$$x(u,t) = u + \tilde{x}(u,t) \text{ and } z(u,t) = u + \tilde{z}(u,t). \tag{2.17}$$

Replacing x with $u + \tilde{x}$ in (2.11) and using (2.16) with (2.10) we get that $\psi = -c\hat{H}y = -c\tilde{x}$. Excluding ψ from (2.12) we obtain Stokes wave equation

$$-c^2 y_u + gyy_u + g\hat{H}[y(1 + \tilde{x}_u)] = 0. \tag{2.18}$$

Now we apply operator $\hat{H}$ to (2.18) and using (2.10) we obtain a closed expression for y. Introducing operator $\hat{k} \equiv -\partial_u \hat{H} = \sqrt{-\nabla^2}$ we arrive to the following expression

$$\hat{L}y \equiv \left(\frac{c^2}{g}\hat{k} - 1\right) y - \left(\frac{\hat{k}y^2}{2} + y\hat{k}y\right) = 0, \tag{2.19}$$

where $c = c_{physical}\sqrt{\frac{2\pi}{\lambda}}$ is the phase speed of wave and $c_0 = \sqrt{g}$ is the phase speed of linear gravity wave with $k = 2\pi/\lambda$. From here on we will use $g = 1$ for simplicity, so $c_0 = 1$ and $c = c_{physical}\sqrt{\frac{2\pi}{\lambda g_{physical}}}$.

Using (2.13a) and (2.13b) we can also arrive to an alternative form of Stokes wave equation

$$\frac{c^2}{2g}\left(1 - \frac{1}{|z_u|^2}\right) = y. \tag{2.20}$$

Equation (2.18) can be further simplified (see derivation in Ref. [82]) if we introduce the projector operator $\hat{P} = \frac{1+i\hat{H}}{2}$ (it projects an arbitrary function to a function analytic in $\mathbb{C}^-$) and supplementing the real part to (2.18) we get a nicer form of the equation for Stokes wave:

$$z_u = 1 + \frac{2g}{c^2}\hat{P}[yz_u] \tag{2.21}$$

or

$$\tilde{z}_u = \frac{2g}{c^2}\hat{P}[\mathrm{Im}[\tilde{z}](1+\tilde{z}_u)]. \tag{2.22}$$

Here operator $\hat{P}$ can be easily applied on Fourier side using $\hat{P} = \frac{1+i\hat{H}}{2}$ and (2.7) as

$$P_k = \frac{1+iH_k}{2} = \frac{1-\operatorname{sign} k}{2} = \begin{cases} 1, k<0 \\ \frac{1}{2}, k=0 \\ 0, k>0 \end{cases} \tag{2.23}$$

Chapter 3

Numerical Methods

We used three numerical methods to solve (2.19) and (2.22) numerically. Two numerical methods (Generalized Petiashvili and Newton Conjugate Gradient) we implemented as described in Ref. [80] to solve (2.19). We also implemented Petiashvili method as well as Newton Conjugate Gradient to solve Eq. (2.22) for additional confirmation of our results. Petiashvili and Generalized Petiashvili methods work well for weakly nonlinear to moderately nonlinear Stokes waves whereas Newton Conjugate Gradient one is more beneficial for highly nonlinear Stokes waves of steepness $H/\lambda > 0.1388$.

3.1 Petviashvili Method (PM)

The first method is a Petviashvili method [90] which was originally proposed to find solitons in nonlinear Schrodinger equation (NLSE) as well as it was adapted for nonlocal NLS-type equations, see e.g.[91].

Applying Petviashvili method to solve Eq. (2.22) we get the following iterative scheme:

$$\begin{aligned}
\tilde{z}_u^{(n+1)} &= RHS^{(n)}M^p, \\
RHS^{(n)} &= \frac{2g}{c^2}\hat{P}[\mathrm{Im}(\tilde{z}^{(n)})(1+\tilde{z}_u^{(n)})], \\
M &= \frac{\langle \tilde{z}_k^{(n)}, ik\tilde{z}_k^{(n)}\rangle}{\langle \tilde{z}_k^{(n)}, RHS_k^{(n)}\rangle},
\end{aligned}$$

where $RHS^{(n)}$ is right hand side of Eq. (2.22) on n-th interation, M is Petviashvili multiplier, and $\tilde{z}_k^{(n)}$ and $RHS_k^{(n)}$ denote Fourier transforms of $\tilde{z}^{(n)}$ and of $RHS^{(n)}$ respectively. Upper index n denotes the iteration number, $\langle\ .\ ,\ .\ \rangle$ denotes complex dot product.

To compute $RHS^{(n)}$ we apply operator $\hat{P}$ in Fourier space using (2.23):

$$RHS_k^{(n)} = \frac{2g}{c^2}P_k\mathcal{FT}[\mathrm{Im}(\tilde{z}^{(n)})(1+\tilde{z}_u^{(n)})].$$

And then we compute $\tilde{z}^{(n+1)}$ on the Fourier side as:

$$\begin{aligned}
\tilde{z}_k^{(n+1)} &= \frac{RHS_k^{(n)}M^p}{ik}, k \neq 0, \\
\tilde{z}_{k=0}^{(n+1)} &= \frac{1}{2}\sum_{k<0} i|k||\tilde{z}_{k=0}^{(n+1)}|^2, k = 0,
\end{aligned}$$

where 0^{th} harmonic of $\tilde{z}$ is treated separately to satisfy zero mean level condition for the fluid (it follows from Eq. (2.22) if one considers 0^{th} harmonic of the left and right hand side):

$$\int y(x)dx = \int y(u)x_u du = \int y(u)(1+\tilde{x}_u)du = 0.$$

So $\tilde{z}_{k=0} = iy_{k=0}$, where

$$y_{k=0} = \frac{\int y(u)du}{2\pi} = -\frac{\int y(u)\tilde{x}_u du}{2\pi} = -\sum_k y_k ik\tilde{x}_k = 2\sum_{k<0} i|k|y_k\tilde{x}_k = \frac{1}{2}\sum_{k<0}|k||\tilde{z}_k|^2,$$

since $\tilde{z}_k = \tilde{x}_k + iy_k$, with $y_k = y_{-k}$ - purely real, $\tilde{x}_k = -\tilde{x}_{-k}$ - purely imaginary and $y_k = i\,\mathrm{sign}(k)\tilde{x}_k$, so $\tilde{x}_k = iy_k = \tilde{z}_k/2$ for $k > 0$ and $\tilde{x}_k = -iy_k = -\tilde{z}_k/2$ for $k < 0$.

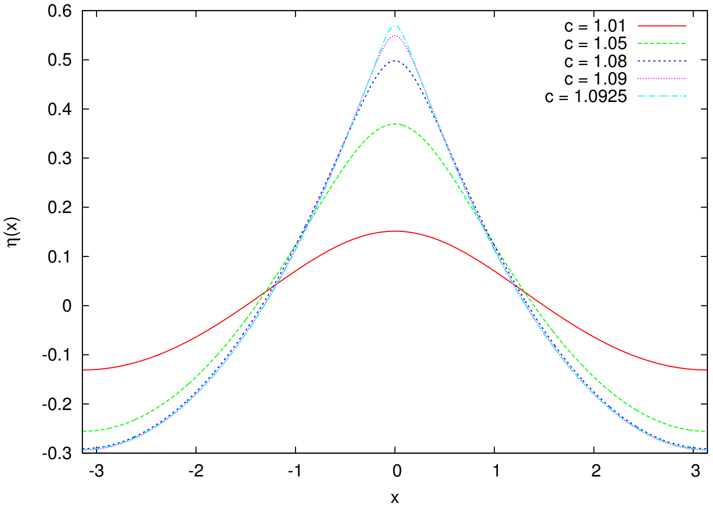

Figure 3.1: Stokes wave computed with Petviashvili method with various values of c.

The power $p > 1$ can be adjusted to improve convergence of iteration depending on the solution, typically we used $\frac{3}{2} \le p \le 6$. Convergence of iterative process can be controlled by the value of Petviashvili multiplier, i.e. the proximity of M to 1 is an effective indicator of convergence.

If the initial profile of $\tilde{z}^{(0)}$ is be taken in such a way, that amplitudes of all Fourier modes $\tilde{z}_k^{(0)}$ are purely imaginary, this will lead to a Stokes wave solution located at the center of periodic interval with $\tilde{z}_k$ being purely imaginary. Initially we choose $\tilde{z}^{(0)} = \frac{i}{10}(Exp[-\frac{2}{5}u^2] - \frac{1}{2})$ for values of c slightly above 1 and later as we increase c we use previous solution as an initial guess.

Several Stokes wave constructed numerically by this algorithm assuming $g = 1$ are shown on Fig. 3.1. Convergence of this method significantly slows down as we approach $H/\lambda \approx 0.138$ or $c \approx 1.0925$.

3.2 Generalized Petiashvili Method (GPM)

The second method we consider is a generalized Petviashvili method (GPM) [92] designed to solve the general equation $\hat{L}y \equiv -\hat{M}y + \hat{N}y = 0$ for the unknown function $y(u)$, where $\hat{L}$ is the general operator which includes a linear part $-\hat{M}$ and a nonlinear part $\hat{N}$. For our particular form of $\hat{L}_0$ in (2.19) we have that:

$$\hat{M} = 1 - \frac{c^2}{g}\hat{k},$$
$$\hat{N}y = -\left(\frac{\hat{k}y^2}{2} + y\hat{k}y\right).$$

Numerically operators $\hat{M}$ and $\hat{N}$ can be applied on Fourier side using

$$[\hat{k}y]_k = [-\partial_u \hat{H}y]_k = |k|y_k, \quad \text{so then} \tag{3.1}$$
$$M_k = 1 - \frac{c^2}{g}|k|. \tag{3.2}$$

$\hat{M}$ is invertible on the space of 2π-periodic functions because Stokes wave requires $1 < c^2/g < 1.1$[93]. The convergence of GPM[92] is determined by the smallest negative eigenvalue of the operator $\hat{M}^{-1}\hat{L}_{lin}$. Here $\hat{L}_{lin}$ is the linearization operator of $\hat{L}$ about the solution y of (2.19):

$$\hat{L}_{lin}\delta y = -\hat{M}\delta y - \left(\hat{k}(y\delta y) + y\hat{k}\delta y + \delta y\hat{k}y\right).$$

It is assumed that $\hat{M}^{-1}\hat{L}_{lin}$ has only a single positive eigenvalue 1 determined by $\hat{L}_{lin}y = \hat{M}y$. GPM iterations [92] are given by:

$$y^{(n+1)} - y^{(n)} = \left(\hat{M}^{-1}Ly^{(n)} - \gamma\frac{\langle y^{(n)}, \hat{L}y^{(n)}\rangle}{\langle y^{(n)}, \hat{M}y^{(n)}\rangle}y^{(n)}\right)\Delta\tau, \tag{3.3}$$

where $\Delta\tau > 0$ is the parameter that controls a convergence speed of iterations and $\gamma = 1 + \frac{1}{\Delta\tau}$ is chosen to project iterations into the subspace orthogonal to y (the only eigenfunction y with the positive eigenvalue).

In practice this method allowed us to find high precision solutions up to $H/\lambda < 0.1388$ as GPM requires significant decrease of $\Delta\tau$ with the growth of H/λ to have convergence.

3.3 Newton Conjugate Gradient Method (Newton-CG)

The last method, Newton-CG [78, 94], is a combination of linearization process and Conjugate Gradient (CG) method for solving the resulting linear system.

To solve (2.19) using Newton-CG method we first linearize (2.19) about the current approximation $y^{(n)}$:

$$\hat{L}y^{(n)} + \hat{L}_{lin}\delta y = 0, \tag{3.4}$$

where

$$\hat{L}_{lin}\delta y = -\hat{M}\delta y - \left(\hat{k}(y^{(n)}\delta y) + y^{(n)}\hat{k}\delta y + \delta y\hat{k}y^{(n)}\right),$$

is a linearization of $\hat{L}$ for the current approximation $y^{(n)}$ and $\hat{M} = 1 - \dfrac{c^2}{g}\hat{k}$.

As a second step, we solve the resulting linear system (3.4) for δy using CG method to obtain next approximation

$$y^{(n+1)} = y^{(n)} + \delta y.$$

Similarly, to solve (2.22) using Newton-CG method we first linearize (2.22) about the current approximation $z^{(n)}$:

$$\hat{L}\tilde{z}^{(n)} + \hat{L}_{lin}\delta\tilde{z} = 0, \tag{3.5}$$

where

$$\hat{L}\tilde{z} = \frac{c^2}{g}\tilde{z}_u - 2\hat{P}[\mathrm{Im}[\tilde{z}](1+\tilde{z}_u)],$$
$$\hat{L}_{lin}\delta\tilde{z} = \frac{c^2}{g}\delta\tilde{z}_u - 2\hat{P}[\mathrm{Im}[\delta\tilde{z}](1+\tilde{z}_u) + \mathrm{Im}[\tilde{z}]\delta\tilde{z}_u],$$

or equivalently for $\delta\tilde{z}$ with only negative ($k < 0$) Fourier modes ($\delta\tilde{z}$ analytic in $\mathbb{C}^-$) that can be enforced without loss of generality (since we are looking for solution $\tilde{z}$ with the same properties)

$$\hat{L}_{lin}\delta\tilde{z} = i\hat{M}\delta\tilde{z} - 2\hat{P}[\mathrm{Im}[\delta\tilde{z}]\tilde{z}_u + \mathrm{Im}[\tilde{z}]\delta\tilde{z}_u].$$

And we solve the resulting linear system (3.5) for $\delta\tilde{z}$ using CG method to obtain next approximation

$$\tilde{z}^{(n+1)} = \tilde{z}^{(n)} + \delta\tilde{z}.$$

It should be noted that monotonic convergence of CG method is proven only for positive definite operators, while in our both cases $\hat{L}_{lin}$ is indefinite. Nevertheless, it was always converging to the solution, and convergence was much faster compared to GPM method.

Newton-CG method can be written in either in physical space or Fourier space. In physical space it requires 6 Fast Fourier transforms (FFTs) per CG step for (3.4) and 4 FFTs for (3.5), while if written in Fourier space requires it requires only 4 FFTs for (3.4) and 3 FFTs for (3.5). In addition, the ordering of these FFTs is such, that they can be performed in parallel on 2 computing threads reducing the computation time down to the time of computation of two serial FFTs.

In simulations using (2.19) we expand $y(u)$ in cosine Fourier series using FFT to speed up simulations. After we solved for $y(u)$ we can immediately recover $\tilde{z}(u)$ via (2.10). While solving (2.22) we have to expand $\tilde{z}(u)$ in a complex Fourier series that is a little bit more computationally demanding for the same size of FFT, the memory requirements are the same since $\tilde{z}_k$ has only negative ($k < 0$) Fourier harmonics (due to analyticity of $\tilde{z}(u)$ in $\mathbb{C}^-$) that are purely imaginary (due to $\tilde{x}(u)$ being odd and $y(u)$ even).

Additional performance improvement can be achieved by using a preconditioner matrix. We used a diagonal preconditioner $\hat{M}$ for both (3.4) and (3.5) based on the linear part of the operator $\hat{L}$.

We found the region of convergence of the Newton-CG method to be quite narrow that requires an initial guess $y^{(0)}$ or $\tilde{z}^{(0)}$ to be quite close to the exact solution for highly nonlinear waves. In practice we first obtain solutions using PM and GPM methods for parameter c slightly above 1 and use Newton-CG method to get highly nonlinear solutions by varying velocity parameter c by small amounts at a time.

3.4 Simulation Challenges

3.4.1 Code Performance

Stokes wave equations (2.19) and (2.22) as we discussed in the previous section can be efficiently solved with a spectral method since operators $\hat{k}$ in Eq. (2.19) and $\hat{P}$ in Eq. (2.22) can be easily computed on the Fourier side for $\mathcal{O}(N)$ operations, where N is the number of sampling points on u-axis. So the total cost of finding $\hat{k}y$ or $\hat{P}y$ is $\mathcal{O}\left(N \log N\right)$ taking into account Fourier transform and Inverse Fourier transform as opposed to $\mathcal{O}\left(N^2\right)$ for finite difference method.

In our simulations we observed that in order to resolve Stoke wave solutions with a given precision (say 10^{-16} in double precision arithmetic or 10^{-32} in quadruple precision arithmetic) as we go to more and more steeper (nonlinear) waves we need

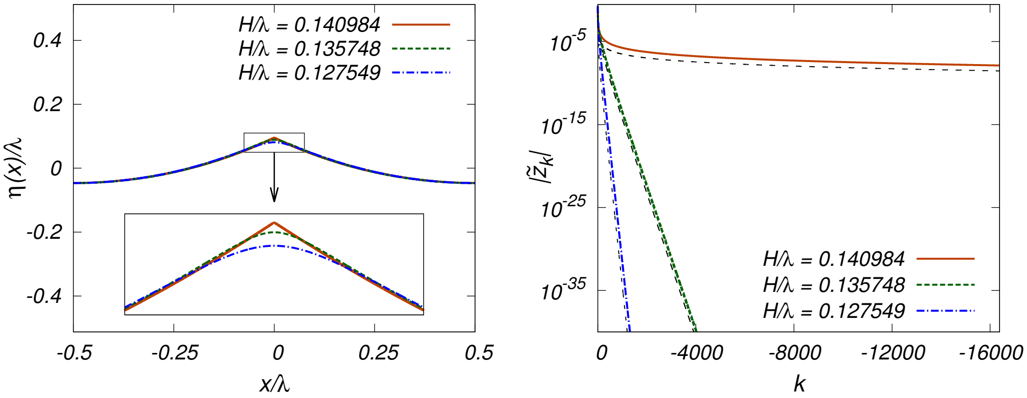

Figure 3.2: Stokes waves(left) and their spectra(right) computed with Newton-CG method. Simulations with $c = 1.0825$ (blue), $c = 1.0915$ (green) and $c = 1.0922795$ (orange) with $N = 2048$, $N = 4096$ and $N = 4194304$ Fourier modes respectively. Black dashed lines are asymptotic decay predicted by theory.

more and more Fourier modes N (see Fig. 3.2) as the tail of Fourier Spectrum of the solutions decays as $\propto e^{-|k|v_c}$ and $v_c \to 0$ as we approach the limiting Stokes wave. Turns out this is due to a singularity at a distance v_c from a real line that the solution has (further discussed in next section). This means that finding solutions near the limiting Stokes wave (with very small v_c) becomes increasingly difficult since we roughly need $N \propto 1/v_c$. We try to overcome this using nonuniform grid in u space described by another conformal map in Chapter 5.

It is also worth mentioning that as we go to highly nonlinear Stokes wave the total number of CG iterations in Newton-CG method required for convergence slowly goes up with N, roughly $\propto Log(N)$. So the total computation time scales like $\propto NLog(N)^2 \propto \frac{1}{v_c}Log(\frac{1}{v_c})^2$.

3.4.2 Stokes Wave Singularity

It is a well known fact that a limiting Stokes wave forms a 120° degree angle at the crest, which corresponds to:

$$\tilde{z}(w) \simeq (iw)^{2/3},$$

and hence a branch-cut type of singularity touching the real line. At the same time according to Ref. [75], the type of singularity for any nonlimiting Stokes wave is a square-root type branch-cut type:

$$\tilde{z}(w) \simeq (iw + v_c)^{1/2} \tag{3.6}$$

that start at a branching point $w = iv_c$. In Ref. [81] it was shown that there are not more singularities anywhere in the complex plane beyond the branch points at iv_c and infinity at $+i\infty$. Since there is a freedom how we draw a branch cut between two branching points we customary choose a vertical branch cut along the imaginary axis. In this case our function $\tilde{z}(w)$ can be represented as an integral along the branch cut

$$\tilde{z}(\zeta) = z_0 + \int\limits_{\chi_c}^{1} \frac{\rho(\chi)d\chi}{\zeta - i\chi} \tag{3.7}$$

in auxiliary space $\zeta = \tan(\frac{w}{2})$, where $\rho(\chi)$ is the density along branch cut and $z_0 = \tilde{z}(\zeta \to \infty) = \tilde{z}(u = \pm\pi)$. The convenience of the space ζ is that in there we have a single finite interval branch cut from $i\chi_c = \tan(\frac{iv_c}{2}) = i\tanh(\frac{v_c}{2})$ to i, whereas in space w we have periodic branch cuts from every $w_c = 2\pi n + iv_c$ to infinity. The jump of $\tilde{z}(\zeta)$ at branch cut is $2\pi\rho(\chi)$ when crossing the branch cut at $\zeta = i\chi$ in clockwise direction [81].

From a numerical point of view a branch cut can be represented as a collection of pole-type singularities along the cut. If the function is analytic everywhere except

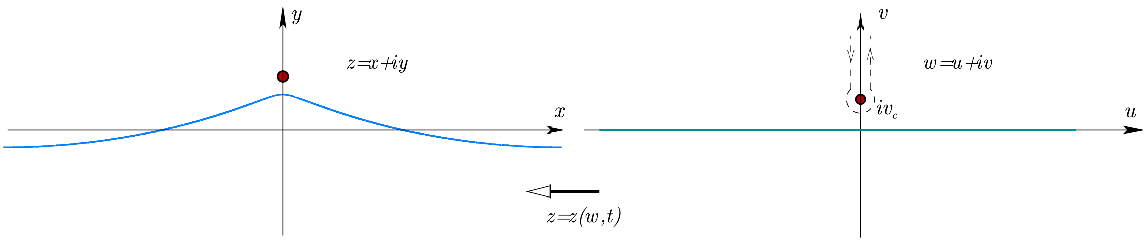

Figure 3.3: Conformal mapping of the lower half-plane $\mathbb{C}^-$ in $w = u + iv$ variables to the region occupied by fluid in physical variables $z(w,t) = x(w,t) + iy(w,t)$ showing singularities above the fluid in both spaces w and z.

for that branch cut one can obtain the positions and residues of these poles from constructing a Padé approximation of that function at the real line $w = u + i0$. In Ref. [81] such reconstruction was done using Alpert-Greengard-Hagström (AGH) algorithm in order to find v_c or χ_c and analyze the branch cut. Using AGH algorithm and quad precision data it was confirmed in Ref. [81] and later in Ref. [82] using a different more accurate method that at $\chi = \chi_c = \tanh(v_c)$ the function $\rho(\chi)$ has a square root singularity as given by

$$\rho(\chi) = A\sqrt{\chi - \chi_c}.$$

Although AGH algorithm is quite general and applicable in many scenarios it doesn't allow one to find the branching point iv_c with high accuracy. Another way to analyze the branch cut is through Fourier series.

Assume that a singularity of $\tilde{z}$ closest to real axis in w complex plane is a root-type branching point

$$\tilde{z} \simeq c_1(w - iv_c)^{\beta}, \tag{3.8}$$

as $w \to iv_c$, where c_1 is the complex constant, $v_c > 0$ and β are real constants. By periodicity of $\tilde{z}(u)$, similar branch points are located at $w = iv_c + 2\pi n$, $n = \pm1, \pm2, \ldots$

We expand $\tilde{z}(u)$ in Fourier series:

$$\tilde{z}(u) = \sum_{k=-\infty}^{0} \hat{\tilde{z}}_k \exp[iku], \tag{3.9}$$

$$\hat{\tilde{z}}_k = \frac{1}{2\pi}\int\limits_{-\pi}^{\pi} \tilde{z}(u)e^{-iku}\, du, \tag{3.10}$$

where $\hat{\tilde{z}}_k$ are Fourier coefficients and the sum is taken over nonpositive integers k which ensures both 2π-periodicity of $\tilde{z}(u)$ and analyticity of $\tilde{z}(w)$ in $\mathbb{C}^-$. We evaluate (3.9) in the limit $k \to -\infty$ by moving the integration contour from $-\pi < u < \pi$ into $\mathbb{C}^+$ until it hits the lowest branch point of (3.8) at iv_c so it goes around branch point and continues straight upwards about both side of the corresponding branch cut as shown by the dashed line in right panel of Fig. 3.3. Here we assume that branch cut is a straight line connecting $w = iv_c$ and $+i\infty$. Then the asymptotic of $|\hat{\tilde{z}}_k|, k \to -\infty$ is given by

$$\begin{aligned}\hat{\tilde{z}}_k &\simeq \frac{1}{2\pi}\int\limits_{-\pi}^{\pi} c_1(w - iv_c)^{\beta}e^{-iku}\, du = \frac{-2c_1}{2\pi}\int\limits_{v_c}^{\infty} (i(v - v_c))^{\beta}e^{kv}\, dv \\ &= \frac{-c_1 i^{\beta}}{\pi}e^{-|k|v_c}\int\limits_{0}^{\infty} v^{\beta}e^{-|k|v}\, dv = \frac{-c_1 i^{\beta}\Gamma(\beta+1)}{\pi}\,\frac{e^{-|k|v_c}}{|k|^{\beta+1}},\end{aligned}$$

$$\text{so} \quad |\hat{\tilde{z}}_k| \propto \frac{e^{-|k|v_c}}{|k|^{\beta+1}} \quad \text{as} \quad k \to -\infty. \tag{3.11}$$

Now since for nonlimiting Stokes waves $\beta = 1/2$ according to (3.6) we get

$$|\hat{\tilde{z}}_k| \propto \frac{e^{-|k|v_c}}{|k|^{3/2}} \quad \text{as} \quad k \to -\infty. \tag{3.12}$$

This scaling of Fourier coefficients on the tail can be used for finding v_c with 2-3 digits of precision.

3.4.3 Approximation of a Nearly Singular Profile

An approximation of a function f with a singular derivative with Fourier series requires many modes N because the decay of Fourier coefficients is only algebraic:

$$|\hat{f}_k| \propto \frac{1}{|k|^{\alpha}}, \alpha > 1 \quad \text{as} \quad |k| \to \infty,$$

and if we want $|\hat{f}_{k=k_{max}}|/|\hat{f}_{k=0}| = 10^{-16}$ we need $N = 2k_{max} = 2 \times 10^{\frac{16}{\alpha}}$.

In fact in our simulations when we approach the limiting Stokes wave ($v_c \to 0$)

$$|\hat{z}_k| \propto \frac{1}{|k|^{\alpha}}, \frac{3}{2} < \alpha < \frac{5}{3} \quad \text{as} \quad k \to -\infty, \tag{3.13}$$

so we can expect $10^{10} \lesssim N \lesssim 10^{11}$ while trying to approximate the limiting Stokes wave in double precision arithmetic.

As a result it becomes essential that the singularities of nonlimiting Stokes waves are always at a finite distance $v_c > 0$ from the real line (though v_c might be small) and hence provide additional exponential decay of the Fourier spectrum tail as in (3.12).

In our simulations using the numerical methods described in Chapter 3 we were able to reach Stokes waves with $v_c \approx 6 \cdot 10^{-7}$, using up to $N = 128 \times 2^{20} \approx 134 \times 10^{6}$ Fourier modes for the steepest waves. But the widening spectrum as $v_c \to 0$ presents a major obstacle for finding solutions with a singularity closer to the real axis. We try to overcome this by solving our problem in a different space q where the singularity of a solution is located at $\tilde{v}_c \gg v_c$ in the complex plane of a new space q related to the u space via another conformal map described in Chapter 5.

3.4.4 Non-Unique dependence on Velocity Parameter

Another difficulty is that the parameter c that appears in the equations (2.19) or (2.22) turns out to be not a monotonic function of steepness H/λ see Fig. 3.4.

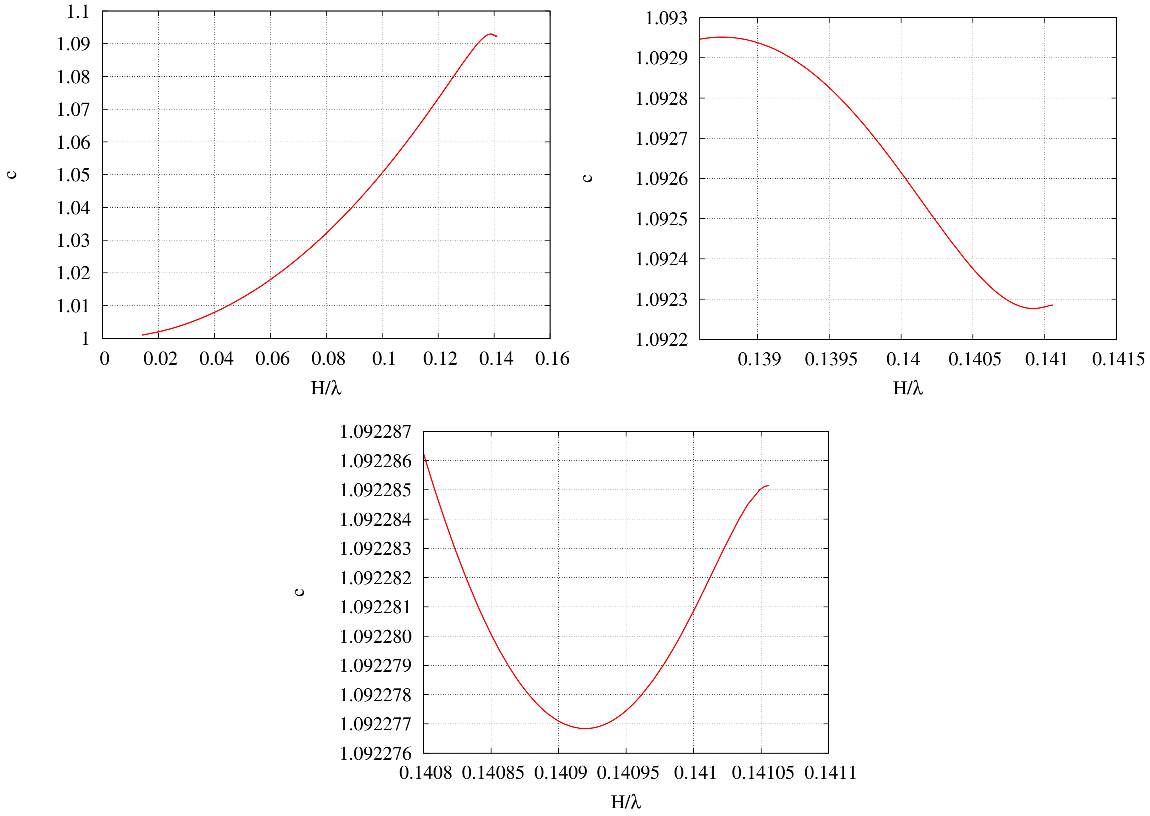

Figure 3.4: Oscillations of dimensionless velocity c of Stokes' wave propagation as a function of steepness H/λ.

Thus in some range of velocities c, for a single value of c there exists several distinct solutions. Therefore having found one of the solutions, we need to have means of reaching the other solutions.

It can be done in the following way: find a solution for a value of c in monotonic region, then go along the curve $c(H/\lambda)$ in small steps in c while using the existing solution as an initial guess for the iterative process in finding the solution for the next value of c. When the extremum on $c(H/\lambda)$ curve is almost reached, use the data for this existing c, but perturb its Fourier coefficients in the following way:

$$\hat{\hat{z}}^*_k = \hat{\hat{z}}_k e^{|k|\delta},$$

where $\hat{\tilde{z}}_k$ is the Fourier coefficients of an already computed Stokes wave near the extremum of $c(H/\lambda)$ and $\hat{\tilde{z}}^*_k$ is Fourier coefficients of a new initial guess. This way we get a function $\hat{\tilde{z}}^*$ that has a singularity at a lower level $\hat{\tilde{z}}^*_c < v_c$ and is a good initial guess of a steeper Stokes wave. A good choice of δ that we typically used in our simulations is $\delta \approx 0.1 v_c$, where v_c is the distance to singularity of $\hat{\tilde{z}}$ solution. See a detailed discussion on how to recover v_c from the solution in the following section.

3.5 Finding Singularity Position

Suppose we found numerical solution $\tilde{z}(u)$. How do we find the distance v_c to the singularity described in Section 3.4.2?

As we discussed previously, Alpert-Greengard-Hagström (AGH) algorithm or fitting Fourier spectrum tails on (3.12) allows one to find v_c only with low accuracy. Here we discuss three methods that actually allow to find v_c with high accuracy.

3.5.1 Finding Singularity from Fourier Spectrum

The first method uses the same idea as in Section 3.4.2 of fitting Fourier spectrum to an asymptotic. To obtain the location of the branch point $w = i v_c$ with good precision one has to go beyond the leading order asymptotic (3.12). Next order corrections to $\hat{\tilde{z}}_k$ have the following form:

$$|\hat{\tilde{z}}_k| \simeq \left(\frac{c_1}{|k|^{3/2}} + \frac{c_2}{|k|^{5/2}} + \frac{c_3}{|k|^{7/2}} + \dots\right) e^{-|k| v_c} = \sum_{n=1}^{\infty} \frac{c_n}{|k|^{n+\frac{1}{2}}} e^{-|k| v_c}, \quad k \to -\infty \tag{3.14}$$

where we took into account the expansion of $\tilde{z}(w)$ around $w = iv_c$ in half-integer powers of $(w - iv_c)$ beyond the leading order term (3.6)

$$\hat{\tilde{z}}(w) \simeq \sum_{n=1}^{\infty} a_n (w - iv_c)^{n+\frac{1}{2}}. \tag{3.15}$$

The numerically obtained spectrum $\hat{\tilde{z}}_k$ of Stokes wave was fitted to the expansion (3.14) in order to find v_c and coefficients $c_1, c_2, c_3, \ldots$. The highest accuracy in recovering v_c was achieved when a window around the middle of spectrum $k \backsim k_{max}/2$ was used for that fit, typically $0.4\, k_{max} \lesssim k \lesssim 0.6\, k_{max}$, where k_{max} is the number of Fourier harmonic for which spectrum hits numerical noise level (decayed 16 orders relative to the 1^{st} Fourier harmonic if we are working in double precision arithmetic). $k_{max}/2$ represent a compromise between the highest desired values of k_{max} to be as close as possible to asymptotic regime $k \to \infty$ and the loss of numerical precision near $k = k_{max}$. We estimated the accuracy of the fit by varying values of k used for fitting as well as changing the number of terms in the expansion (3.14).

This method allows one to obtain v_c with the absolute accuracy about $10^{-9}-10^{-11}$ in double precision (DP) using 7-12 terms in the series (3.14).

3.5.2 Finding Singularity from Fit in Space u

Consider the formal series

$$\hat{\tilde{z}}(\zeta) \simeq \sum_{n=0}^{\infty} ib_n (i\zeta + \chi_c)^{\frac{n}{2}} \tag{3.16}$$

in the neighborhood of the branch point $\zeta = i\chi_c$ in auxiliary space $\zeta = \tan(\frac{w}{2})$. We used $(i\zeta + \chi_c)$ instead of $(\zeta - i\chi_c)$ to make sure that the branch cut is vertical and pointing upwards considering the standard convention of $(\zeta)^{1/2}$ having a branch cut horizontal and pointing to $\zeta \to -\infty$. The term i in front of the coefficients b_n is factored for convenience to ensure that coefficients b_n take real values. One can use the nonlinear fit of numerical simulations data to the series (3.16) to determine the unknowns χ_c (and consequently $v_c = 2\,\mathrm{arctanh}(\chi_c)$) and b_n.

Initially we use $M = 1 - 2$ terms in the series (3.16) and several data points $(u_n, \tilde{z}(u_n))$ closest to $u = 0$ to get a rough estimate of χ_c. After that we increase M by 1 at a time all the way to $M \sim 20 - 30$ until the error of the nonlinear fit becomes minimal possible (typically $\sim 10^{-14} - 10^{-16}$). At these later steps we use the data points $(u_n, \tilde{z}(u_n))$ that are inside the disk of convergence $|u_n - i\chi_c| < 2\chi_c$ of the series (3.16), or $|u_n| < \sqrt{2}\chi_c$, since the radius of convergence of that series is $2\chi_c$ as discussed in Ref. [82]. Here values of $\tilde{z}(u_n)$ are taken from simulations with u_n being the numerical grid points closest to $u = 0$.

While the accuracy of the nonlinear fit typically reaches $\sim 10^{-14} - 10^{-16}$ the absolute accuracy of the found value v_c is about $10^{-9} - 10^{-11}$ in double precision (DP) as in the previous method.

3.5.3 Finding Singularity from Compatibility Condition

This method is described in Section 6.1 a of Ref. [82] and based on the compatibility of the series expansions at points $\zeta = \pm i\chi_c$ in the axillary space $\zeta = \tan(\frac{w}{2})$ with the equation (2.20) of Stokes wave. In contrast, the previous two methods use numerical values of $(u_n, \tilde{z}(u_n))$ and do not use the equation (2.20) directly.

Current realization of this algorithm also requires Pade approximation of the solution in the axillary space ζ (described in Section 4 of Ref. [81]) for calculation of coefficients of series expansion at the point $\zeta = -i\chi_c$. This method is so far the most accurate but requires $\mathcal{O}(N \times N_d)$ operations (N_d is the number of poles) for finding Pade approximation of a solution thus slow for large N. We typically used that method for $N > 10^5$, where the small value of v_c required us to use quadruple (quad) precision with 32 digits accuracy both to obtain $\tilde{z}$ and recover v_c. The absolute accuracy for v_c in this method was and $\sim$ 10−10 in double precision (DP) and $\sim$ 10−26 in quad precision (QP).

Chapter 4

Summary of Previous Results on Stokes Wave

Summarizing the results of papers [80, 81] and [82] our research group calculated Stokes waves $\tilde{z}(u)$ with high accuracy for different values of H/λ using computations in double(16 digits), quad (32 digits) and multiple (we used 200 digits) precision, recovered position of the singularity position iv_c with high precision and analyzed the structure of the branch cut using methods described below in Section 3.5. Figure 3.2 shows the spatial profiles of Stokes waves for several values of H/λ in physical variables (x, y). The Stokes wave quickly approaches the profile of limiting wave except a small neighborhood of the crest.

The oscillatory behaviour of Stokes wave speed c as a function of steepness H/λ is shown in Figure 3.4. This function is nonmonotonic which is in agreement with previous simulations [73, 95, 96] and theoretical analysis [14, 15] which predicted an infinite number of oscillations. We were able to resolve 1.5 oscillations (two maxima and one minimum) using double precision arithmetic and 2 oscillations (two maxima and two minima) using quadruple precision arithmetic on this graph.

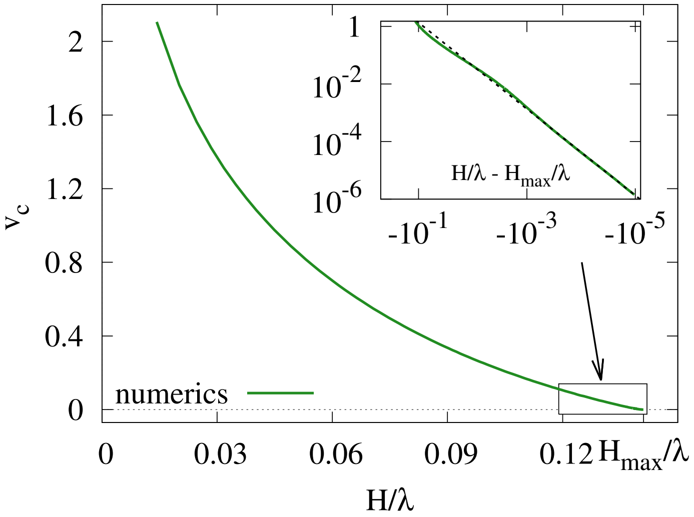

Figure 4.1: Distance v_c to the closest singularity of $\tilde{z}(w)$ as a function of H/λ. Insert shows zoom-in for $(H - H_{max})/\lambda \ll 1$ with $H_{max} = 0.1410633$ being an estimate of the height of the limiting Stokes wave and dashed line is the power law $v_c \propto (H - H_{max})^{3/2}$.

The highest wave obtained [81] using quadruple precision and $N = 2^{27} \approx 134\times10^6$ Fourier modes had $c = 1.0922851405$, $H^{max}_{num}/\lambda = 0.141057778854883208164928602 2$ and $v_c = 5.93824419892803271779 \times 10^7$. These numbers are the moderate extension of the previous work [80] by pushing down a lowest value of v_c about two times. Further decrease of the numerical values of v_c was not possible due to extreme computational cost of simulations with $N > 10^8$.

For each of the solutions we found a distance to the closest singularity v_c. Figure 4.1 taken from Ref. [80] shows a dependence of v_c as a function of H/λ. Back in [80] v_c was calculated with low accuracy using Alpert-Greengard-Hagström (AGH) and fitting of Fourier spectrum to (3.12). Now we have more accurate v_c data computed with more advances methods as described in Section 3.5 which allows for more accurate analysis.

Before Dyachenko et al. (2014) work [80], the numerical estimates of steepness of the limiting Stokes wave H_{max} were found by Williams (1985) as $H_{max}^{Williams}/\lambda = 0.141063$ and Gandzha & Lukomsky (2007) $H_{max}^{GL}/\lambda = 0.14106348398$. The other commonly used but less precise estimate is $H_{max}^{Schwartz}/\lambda = 0.1412$ (Schwartz 1974). It was shown in Dyachenko et al. (2014) [80] that numerical values of v_c in the limit $(H - H_{max})/\lambda \ll 1$ fit quite well to the scaling law $v_c \propto (H - H_{max})^{3/2}$ with $H_{max}/\lambda = 0.1410633 \pm 4 \times 10^{-7}$ It suggested that the previous estimate $H_{max}^{Williams}$ is more accurate than $H_{max}^{Schwartz}$. Also H_{max}^{GL} is within the accuracy of Dyachenko et al. (2014) [80] estimate.

Chapter 5

New Conformal Map

Conformal mappings can be used for improving efficiency of simulations for the general periodic 1D system defined on the real line if such system allows analytic continuation to the strip containing the real axis (see e.g. [97] for review). Assume that v_c is the vertical distance from the real line to the complex singularity closest to the real line. Thus v_c defines the thickness of the strip of analyticity in the direction where the singularity is nearest to the real line (Stokes wave is a special case because the thickness of strip is determined by the distance v_c in the upper complex half-plane $w \in \mathbb{C}^+$ while the thickness is infinite below the real line). Then the spectrum of the solution scales as

$$\hat{\tilde{z}}_k \propto e^{-v_c|k|} \quad \text{for} \quad k \gg 1. \tag{5.1}$$

The idea is to find a conformal transformation from w to the new complex variable q which makes the strip of analyticity thicker, i.e. to push all complex singularities of the system to the distance $\tilde{v}_c > v_c$ from the real line. Then spectrum of the solution in the new conformal variable scales as $\propto e^{-\tilde{v}_c|k|}$ for $k \gg 1$, i.e. decays faster than in (5.1) speeding up numerical convergence. A similar idea can be applied to the nonperiodic systems holomorphic in a closed ellipse around the segment of the real line (with foci corresponding to the two ends of that segment) with e.g. rational spectral interpolants used instead of Fourier series [98]. In all such cases the spectral numerical methods are highly efficient and typically having exponential convergence with the number of grid points N used for the spectral collocation. However exploiting such idea for the dynamics of the ideal fluid with free surface on infinite depth has previously met with obstacles because the water waves dynamics requires to work with function holomorphic in the entire lower complex half plane instead of the strip. In other words, only singularities in the upper complex half-plane $w \in \mathbb{C}^+$ are allowed for the dynamics of the ideal fluid. Here we overcome that obstacle by the proper choice of the conformal map.

As we discussed in Section 3.4 approaching the limiting Stokes wave is a challenging numerical problem since the distance v_c from the closest singularity in the upper half-plane to the real line goes to zero as we approach the wave with maximum hight H_{max}/λ, which is responsible for the widening of the solution's Fourier spectrum.

In this Chapter we introduce an auxiliary conformal mapping which moves this singularity further away from the real line increasing v_c while being consistent with the fluid dynamics and thus dramatically speeding up numerical convergence. The advantages of this conformal mapping become especially evident as we approach the limiting Stokes wave (the wave of the greatest height).

5.1 New Conformal Map and a Non-Uniform Grid

Consider a new conformal map

$$q = 2\arctan\left[\frac{1}{L}\tan\frac{w}{2}\right], \tag{5.2}$$

where q is the new complex coordinate and L is the arbitrary positive constant which we adjust to optimize performance of simulations. This conformal transformation is

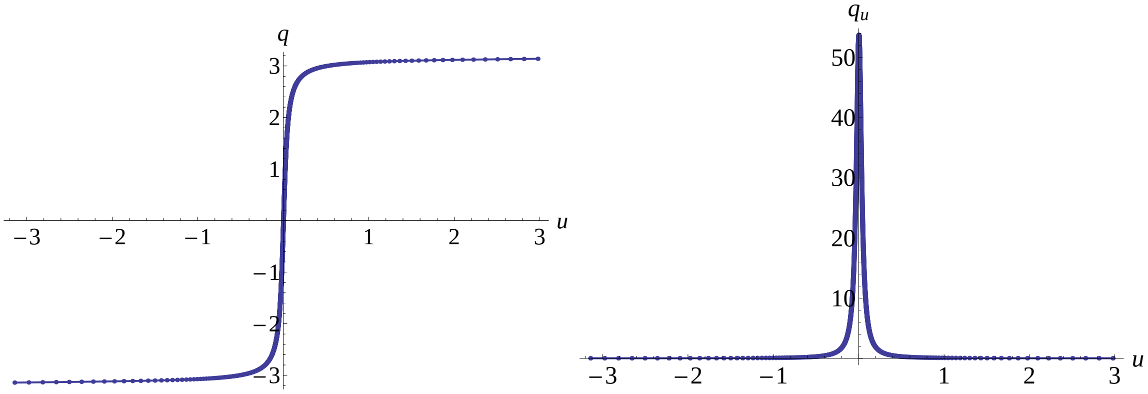

Figure 5.1: The conformal map $q(u)$ given by equation (5.2) (left panel) and the Jacobian $q_u(u)$ given by equation (5.6) (right panel) with $L = 0.0186...$. The dots represent $N_q = 1024$ points which are uniformly spaced at the interval $-\pi \leq q < \pi$ the variable q while being strongly concentrated near $u = 0$ in the variable u.

2π-periodic in w and maps the real line $w = u$ into the real line $q = Re(q)$.

Inverting equation (5.2) at the real line $u = w$, we obtain that

$$u = 2\arctan\left[L\tan\frac{q}{2}\right] \tag{5.3}$$

which is 2π-periodic in q. Recalling that we assume 2π periodicity of Stokes wave solution $\tilde{z}(u)$, we conclude that it is sufficient to consider the conformal transformations (5.2) and (5.3) between half-strip $-\pi \leq u \leq \pi$, $-\infty < v \leq 0$ and $-\pi \leq Re(q) \leq \pi$, $-\infty < Im(q) \leq 0$ in w and q, respectively. Here 2π-periodicity is ensured by the limits $q \to \pm\pi$ for $u \to \pm\pi$.

If we assume that $|u| \ll L$ then equation (5.2) is reduced to

$$q \approx \frac{u}{L} \tag{5.4}$$

which implies that taking numerical step $\Delta q \sim 1$ in q space for q near 0 is equivalent to taking the numerical step $\Delta u \sim L \ll 1$ in u space. It ensures that the uniform grid in q space is highly concentrated near $u = 0$ in u space, with a "density" of grid points $q_u \sim 1/L$ near $u = 0$. It allows to use much less grid points on the uniform

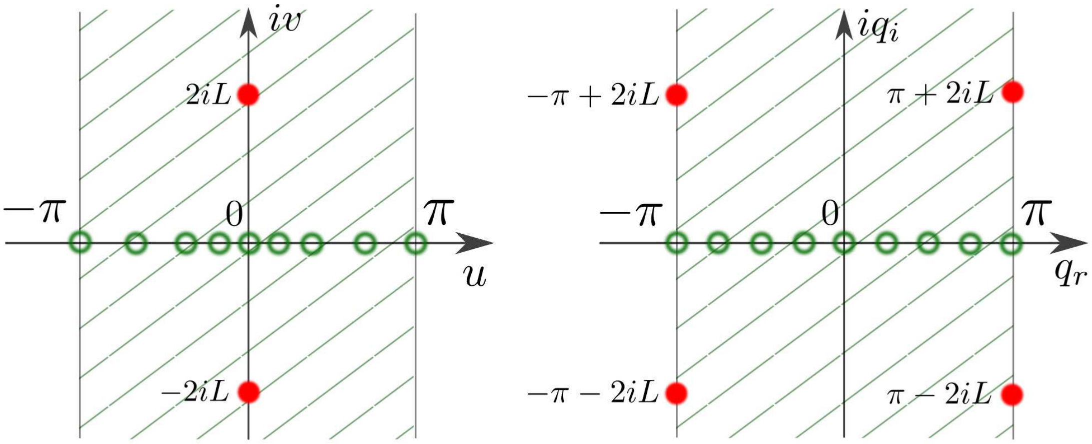

Figure 5.2: A schematic of the conformal map (5.2) from the strip $-\pi \le Re(w) < \pi$ of the complex variable $w \equiv u + \mathrm{i}v$ (left panel) into the strip $-\pi \le Re(q) < \pi$ of the complex variable $q \equiv q_r + \mathrm{i}q_i$ (right panel). The only exceptions are the singularities of the conformal map at $w = \pm 2\arctan(\mathrm{i}L) + 2\pi n = \pm 2\mathrm{i}L + 2\pi n + O(\mathrm{i}L^3)$, $n = 0, \pm 1., \pm 2, \ldots$ (shown by filled red circles at left panel) which are mapped to the complex infinity in q. In a similar way, the inverse conformal map from q to w is singular at points $q_\pm = \pm 2\arctan(\mathrm{i}/L) + \pi(2n+1) = \pm 2\mathrm{i}L + \pi(2n+1) + O(\mathrm{i}L^3)$, $n = 0, \pm 1., \pm 2, \ldots$ (shown by filled red circles at right panel) which are mapped to the complex infinity in w. Open circles schematically show that the uniform grid (uniformly spaced points) at the real line $q = Re(q)$ is mapped into the nonuniform grid at the real line $w = Re(w)$. The nonuniform grid is denser near $w = 0$ which allows to adaptively resolve the complex singularity (branch point) of Stokes wave located at the imaginary axis $w = \mathrm{i}v_c$.

grid in q space in comparison with the uniform grid in u space (the uniform grid was used previously in many simulations, see e.g. Refs. [88, 11, 80, 81]) to achieve the same precision of a numerical solution. To make these arguments precise we use the Jacobian q_u of the transformation (5.2) is given by

$$\begin{aligned} q_u = \frac{1}{u_q} = \frac{1}{L\cos^2\frac{u}{2}\left(1 + \frac{1}{L^2}\tan^2\frac{u}{2}\right)} &= \frac{\cos^2\frac{q}{2}\left(1 + L^2\tan^2\frac{q}{2}\right)}{L} \\ &= \frac{1 + L^2 + (1 - L^2)\cos q}{2L}. \end{aligned} \tag{5.5}$$

Then for a general value of q, the steps Δq and Δu are related as

$$\Delta q = q_u \Delta u + O(\Delta u^2) = \frac{1 + L^2 + (1 - L^2)\cos q}{2L}\Delta u + O(\Delta u^2). \tag{5.6}$$

Fig. 5.1 shows $q(u)$ and q_u for $L = 0.0186\ldots$ with dots representing $N_q = 1024$ points of discrete grids both in u and q spaces separated by Δu and Δq, respectively.

Figs. 5.1 and 5.2 show schematically that the new conformal map (5.2) zooms at the real line into the neighborhood of $w = 0$ which is the closest point (among all points on the real line $w = Re(w)$) to the lowest singularity of the strongly nonlinear Stokes wave which is located at $w = \mathrm{i}v_c,\ v_c \ll 1$. Then the uniform grid in the new variable q corresponds to the highly nonuniform grid in space u and in the physical coordinates (x, y) with the grid points concentrating at the neighborhood of the singularity as seen in Fig. 5.1.

The branch point singularity of Stokes wave, located at $w = \mathrm{i}v_c$ in w plane which, in accordance with the Eq. (5.2), corresponds to $q = \mathrm{i}q_c$ in q plane, where

$$q_c = 2\,\mathrm{arctanh}\left[\frac{1}{L}\tanh\frac{v_c}{2}\right] \tag{5.7}$$

which implies that

$$q_c = \frac{v_c}{L} + O\left(\frac{v_c^3}{L^3}\right) \simeq \frac{v_c}{L} \quad \text{for} \quad v_c \ll L \tag{5.8}$$

as schematically shown in Fig. 5.3. It means that the free parameter L of the transformation (5.2) allows to change the position of the singularity in the complex q plane. Here it is assumed that $v_c/L \ll 1$. Then the spectrum of a solution in q variable decays as

$$\hat{\tilde{z}}_k \propto e^{-(v_c/L)|k|} \quad \text{for} \quad k \gg 1 \tag{5.9}$$

which is much faster than (5.1) for $L \ll 1$. It makes the new conformal map (5.2) highly efficient.

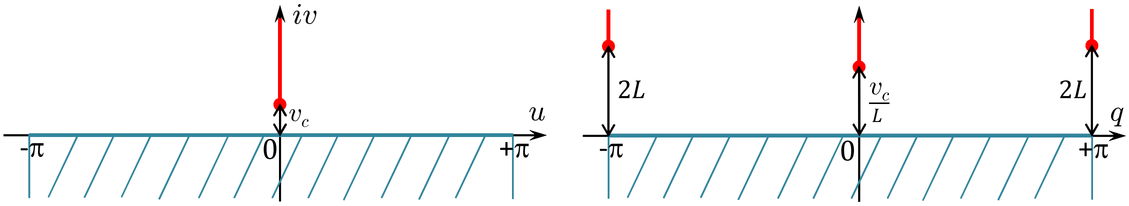

Figure 5.3: Dots schematically show the singularity at $w = \mathrm{i}v_c$ of Stokes wave in the variable $w = u+\mathrm{i}v$ (left panel) and the same singularity at $\mathrm{i}q_c = \mathrm{i}v_c/L+O(\mathrm{i}v_c^3/L^3) \simeq \mathrm{i}v_c/L$ together with the new singularities due to the inverse of the conformal map (5.2) at $q = \pm\pi + 2\mathrm{i}L + O(\mathrm{i}L^3) \simeq \pm\pi + 2\mathrm{i}L$ in the new variable q (right panel). The line extended upwards to $\mathrm{i}\infty$ on the left panel corresponds to branch cut of the Stokes wave. That branch cut is mapped by (5.2) into three branch cuts extending upwards to $\mathrm{i}\infty$ from three dots on right panel with $\mathrm{i}\infty$ from w plane mapped into both $q = \pm\pi + 2\mathrm{i}L + O(\mathrm{i}L^3)$ by 2π periodicity. See the text for more details on that. Shaded areas on both panels correspond to the area occupied by fluid.

However, the asymptotic (5.9) is valid provided $q = \mathrm{i}q_c$ is closer to the real axis than the other parts of the mapping of the Stokes wave branch cut $w \in [\mathrm{i}v_c, \mathrm{i}\infty)$ into q plane. In particular, a one part $w \in [\mathrm{i}v_c, 2\mathrm{i}L + O(\mathrm{i}L^3))$ of Stokes wave branch cut is mapped into $q \in [\mathrm{i}q_c, \mathrm{i}\infty)$ and another part $w \in (2\mathrm{i}L + O(\mathrm{i}L^3), \mathrm{i}\infty)$ is mapped into two branch cuts $q \in (\pm\pi + \mathrm{i}\infty, \pm\pi + 2\mathrm{i}L + O(\mathrm{i}L^3))$ by 2π periodicity in q as sketched by vertical lines in Fig. 5.3. Here the branch points $\pm\pi + 2\mathrm{i}L + O(\mathrm{i}L^3)$ correspond to the singularities of the conformal map (5.3) in q space.

These singularities are obtained from the Jacobian (5.5) which is nonsingular for any value $q \in \mathbb{C}$ but reaches zero (i.e. the singularity of u_q) at

$$q \; = q_\pm := \pm 2 \arctan \frac{\mathrm{i}}{L} + 2n\pi, \quad n = 0, \pm1, \pm2, \ldots. \tag{5.10}$$

For $L \ll 1$ Eq. (5.10) reduces in the strip $-\pi \leq Re(q) \leq \pi$ to

$$q_\pm = \pm\pi \pm 2\mathrm{i}L + O(\mathrm{i}L^3). \tag{5.11}$$

The locations q_+ and $\mathrm{i}q_c$ of Stokes wave singularities in q space are shown schematically in Fig. 5.3.

We note that the singularities $q_- = \pm\pi - 2\mathrm{i}L + O(\mathrm{i}L^3)$ are located in $q \in \mathbb{C}^-$ but they are invisible for any function $f(q)$ which is 2π periodic because the jumps at the corresponding branch cut $q \in (\pm\pi - 2\mathrm{i}L + O(\mathrm{i}L^3), \pm\pi - \mathrm{i}\infty)$ are identically zero, see also Refs. [81, 82] for somewhat similar discussion. Because of that we show points q_- by filled circles for the transformation in right panel of Fig. 5.2 but do not show q_- in right panel of Fig. 5.3. If instead of a Stokes wave one would consider a function $\tilde{z}(w)$ with the branch cut of finite extent then the end point of the mapping of that branch cut into q plane would be not q_+ but other point located higher above the real axis. However we do not consider such functions in here.

The singularity q_+ dominates the asymptotic of Stokes wave Fourier Transform (FT) in q variable for small values L provided $|Im(q_+)| < q_c$. Thus the best convergence of FT (fastest decays of Fourier harmonics at large k) occurs for $|Im(q_+)| = q_c$ which together with Eqs. (5.8) and (5.11) give the optimal choice of the parameter L given by

$$L_{optimal} \simeq \left(\frac{v_c}{2}\right)^{1/2} \tag{5.12}$$

which is valid for $v_c \ll 1$.

For $L = L_{optimal}$ both singularities of Stokes wave are located at a distance $\approx (2v_c)^{1/2}$ from the real axis in q space ensuring the fastest possible convergence of Fourier modes as

$$\hat{\tilde{z}}_k \propto e^{-(2v_c)^{1/2}|k|} \quad \text{for} \quad k \gg 1. \tag{5.13}$$

E.g., the simulation of Ref. [81] with $N = 2^{27} \simeq 1.3 \cdot 10^8$ and $v_c \simeq 5.9 \cdot 10^{-7}$ required running 64 cores computer cluster for ~ 3 months. In contrast, the simulations described in Chapter 6 (with the use the new conformal map (5.2)) allowed to achieve the same precision for the numerical grid with $N_q \simeq 4.2 \cdot 10^4$ Fourier modes which takes a few minutes on the desktop computer. Respectively, by increasing N_q (according to equation (5.13), one has to choose $N_q \sim N^{1/2}$ to reach the same precision as on the uniform grid) we were able to study Stokes waves with significantly smaller values of v_c (down to $\sim 10^{-11}$) than in Ref. [81].

The new conformal map (5.2) and its inverse (5.3) provide the mapping between half-strips in w and q lower complex planes as shown in Fig. 5.3 by shaded areas. These areas extend all the way down in the complex planes and correspond to the area occupied by fluid with the exception of the singularity points of the conformal map. These exceptional points result in the extra constant terms found in Section 5.3 to ensure the exact solution of Euler equation through the conformal map.

5.2 Stokes Wave Equation in the New Space

Here we start from Stokes equation (2.19) in u space and derive the corresponding equation for q space. For clarity we introduce subscript $_u$ for operators in u space and subscript $_q$ for operators in q space and provide Eq. (2.19) here one more time with new notation:

$$\left(c^2\hat{k}_u - 1\right) y - \left(\frac{\hat{k}_u y^2}{2} + y\hat{k}_u y\right) = 0, \tag{5.14}$$

where $\hat{k}_u$ is the positive-definite linear operator defined by

$$\hat{k}_u := -\frac{\partial}{\partial u}\hat{H}_u = \sqrt{-\frac{\partial^2}{\partial u^2}}, \tag{5.15}$$

and $\hat{H}_u$ is the Hilbert transform

$$\hat{H}_u f(u) = \frac{1}{\pi}\text{p.v.}\int\limits_{-\infty}^{+\infty} \frac{f(u')}{u' - u}\mathrm{d}u', \tag{5.16}$$

which for 2π-periodic function $f(u)$ becomes (2.9):

$$\hat{H}_u f(u) = \sum_{n=-\infty}^{n=\infty} \frac{1}{\pi}\text{p.v.}\int\limits_{-\pi}^{\pi} \frac{f(u')}{u' - u + 2\pi n}\mathrm{d}u' = \frac{1}{2\pi}\text{p.v.}\int\limits_{-\pi}^{\pi} \frac{f(u')}{\tan(\frac{u'-u}{2})}\mathrm{d}u'. \tag{5.17}$$

For 2π-periodic function $f(u)$ the Hilbert operator $\hat{H}_u$ is a multiplication operator on the Fourier coefficients:

$$(\hat{H}_u f)_k = \mathrm{i}\,\mathrm{sign}(k)\, f_k, \tag{5.18}$$

where

$$\mathrm{sign}(k) = \begin{cases} -1, & k < 0 \\ \frac{1}{2}, & k = 0 \\ 1, & k > 0 \end{cases},$$

and f_k are the Fourier coefficients (harmonics)

$$f_k = \frac{1}{2\pi} \int\limits_{-\pi}^{\pi} f(u) \exp\left(-\mathrm{i}ku\right) \mathrm{d}u, \tag{5.19}$$

of the function $f(u)$ represented through the Fourier series

$$f(u) = \sum_{k=-\infty}^{\infty} f_k \exp\left(\mathrm{i}ku\right). \tag{5.20}$$

After solving Eq. (5.14) numerically as described in Chapter 3, we recover the real part $x(u)$ of solution $z(u) = x(u) + \mathrm{i}y(u)$ from $y(u)$ according to Eq. (2.10) as

$$x = u - \hat{H}_u y. \tag{5.21}$$

Then Stokes wave solution is represented in parametric form $(x(u), y(u))$.

Eq. (5.14) was derived in Ref. [80] under the assumption that

$$\int\limits_{-\pi}^{\pi} \eta(x)\mathrm{d}x = \int\limits_{-\pi}^{\pi} y(u)x_u(u)\mathrm{d}u = \int\limits_{-\pi}^{\pi} y(u)[1 + \tilde{x}_u(u)]\mathrm{d}u = 0, \tag{5.22}$$

meaning that the mean elevation of the free surface is set to zero. Equation (5.22) reflects a conservation of the total mass of fluid.

Here instead of solving Eq. (5.14) in u-variable, we transform it into q-variable using (5.3). Then we solve the resulting equation numerically in a more efficient way using the procedure described in Section 5.4. We express u through q as given by Eq. (5.3), and obtain from Eqs. (5.14) and (5.5) that

$$\left(c^2 q_u \hat{k}_q - 1\right) y - \left(q_u \frac{\hat{k}_q y^2}{2} + q_u y \hat{k}_q y\right) = 0, \tag{5.23}$$

where the operators

$$\hat{k}_q := -\frac{\partial}{\partial q}\hat{H}_q = -\frac{\partial}{\partial q}(\hat{H}_q + const) \tag{5.24}$$

and

$$\hat{H}_q f(q) = \frac{1}{\pi}\text{p.v.}\int\limits_{-\infty}^{+\infty} \frac{f(q')}{q'-q}\mathrm{d}q' = \frac{1}{2\pi}\text{p.v.}\int\limits_{-\pi}^{\pi} \frac{f(q')}{\tan(\frac{q'-q}{2})}\mathrm{d}q' \tag{5.25}$$

now act in q space with q_u given by Eq. (5.5). Here and below we abuse notation and use the same symbol y for both functions of u and q (in other words, we assume that $\tilde{y}(q) = y(u(q))$ and remove $\tilde{}$ sign). The comparison of Eqs. (5.14) and (5.23) together with Eqs. (5.16) and (5.25) reveals that we simply replaced $\hat{H}_u$ by $\hat{H}_q + const$, where the explicit expression for a constant is not important for solving Eq. (5.23) because it includes derivatives over q thus removing this constant. The justification of the validity of this nontrivial replacement is provided in Section 5.3. We also note by comparison of the definitions of $\hat{k}_u$ and $\hat{k}_q$ above in this Section that FT of $\hat{k}_q$ has the same meaning of the multiplication on $|k|$ but this time in Fourier space of q.

Because the Jacobian q_u is nonzero for any real values $q \in [-\pi, \pi]$, one immediately obtains from equation (5.23) a more compact expression

$$\left(c^2 \hat{k}_q - \frac{2L}{1 + L^2 + (1 - L^2)\cos q}\right) y - \left(\frac{\hat{k}_q y^2}{2} + y \hat{k}_q y\right) = 0, \tag{5.26}$$

which we use for simulations.

The mean level zero condition (5.22) is transformed to

$$\int\limits_{-\pi}^{\pi} y(q)[u_q + \tilde{x}_q(q)]dq = 0 \tag{5.27}$$

in the q variable.

5.3 Projectors and Hilbert Transformation in q Variable

In this Section we justify the use of the operator $\hat{k}_q$ in Eqs. (5.23) and (5.26). It is convenient to introduce the operators

$$\hat{P}_u^- = \frac{1}{2}(1 + \mathrm{i}\hat{H}_u) \quad \text{and} \quad \hat{P}_u^+ = \frac{1}{2}(1 - \mathrm{i}\hat{H}_u) \tag{5.28}$$

which are the projector operators of a general periodic function into a functions analytic in $w \in \mathbb{C}^-$ and $w \in \mathbb{C}^+$ correspondingly. To understand the action of these projector operators, we introduce the splitting of a general 2π periodic function $f(u)$ with the Fourier series (5.20) as

$$f(u) = f^+(u) + f^-(u) + f_{0,u}, \tag{5.29}$$

where

$$f^+(u) = \sum_{k=1}^{\infty} f_k \exp(\mathrm{i}ku) \tag{5.30}$$

is the analytical (holomorphic) function in $\mathbb{C}^+$ and

$$f^-(u) = \sum_{k=-\infty}^{-1} f_k \exp(\mathrm{i}ku) \tag{5.31}$$

is the analytical function in $\mathbb{C}^-$ as well as $f_{0,u}$ is the zero Fourier harmonic defined through Eq. (5.19) as $f_{0,u} = f_k|_{k=0} = \frac{1}{2\pi}\int\limits_{-\pi}^{\pi} f(u)du$. Together with the property

$$\hat{H}_u f = \mathrm{i}[f^+(u) - f^-(u)] \tag{5.32}$$

which follows from Eq. (5.18) we obtain that

$$\hat{P}_u^- f = \frac{f_{0,u}}{2} + f^-(u) \quad \text{and} \quad \hat{P}_u^+ f = \frac{f_{0,u}}{2} + f^+(u), \tag{5.33}$$

i.e. the functions which are holomorphic in $\mathbb{C}^-$ and $\mathbb{C}^+$, respectively.

Here we use the notation $\hat{P}_u^-$, $\hat{P}_u^+$ and $\hat{H}_u$ for the projectors and Hilbert transform in u space. Similarly, we introduce projector operators $\hat{P}_q^-$, $\hat{P}_q^+$ and Hilbert transform $\hat{H}_q$ in the q-variable. We can use two approaches to determine the form of projectors $\hat{P}_u^-$, $\hat{P}_u^+$ in the q space. The first approach is to analyze how Fourier series transforms as we make a change of variables from u to q. The second approach is to use definition of these operators through complex contour integrals and see how these integrals transform as we make a change of variables from u to q. In this work we focus on the second approach as well as we provide the expressions only for $\hat{P}_q^-$ and $\hat{H}_q$. The expression for $\hat{P}_q^+$ can be derived in a similar way but it is not need for the computation of Stokes wave.

Using the Sokhotskii-Plemelj theorem (see e.g. [99, 100])

$$\int\limits_{-\infty}^{\infty} \frac{f(u')du'}{u' - u + \mathrm{i}0} = \text{p.v.} \int\limits_{-\infty}^{\infty} \frac{f(u')du'}{u' - u} - \mathrm{i}\pi f(u), \tag{5.34}$$

where i0 means $\mathrm{i}\epsilon$, $\epsilon \to 0^+$, we rewrite Eq. (5.28) as follows

$$\hat{P}_u^- f = \frac{1}{2}(\mathrm{i}\hat{H}_u + 1) f = -\frac{1}{2\pi\mathrm{i}} \text{p.v.} \int\limits_{-\infty}^{\infty} \frac{f(u')du'}{u' - u} + \frac{1}{2} f(u) = -\frac{1}{2\pi\mathrm{i}} \int\limits_{-\infty}^{\infty} \frac{f(u')du'}{u' - u + \mathrm{i}0}. \tag{5.35}$$

We now use 2π periodicity of $f(u)$ to reduce Eq. (5.35) into the integral over one period

$$\hat{P}_u^- f = -\frac{1}{2\pi\mathrm{i}} \sum_{n=-\infty}^{\infty} \int\limits_{-\pi}^{\pi} \frac{f(u')du'}{u' - u + \mathrm{i}0 + 2\pi n} = -\frac{1}{4\pi\mathrm{i}} \int\limits_{-\pi}^{\pi} \frac{f(u')du'}{\tan \frac{u' - u + \mathrm{i}0}{2}}. \tag{5.36}$$

Using equations (5.3) and (5.5) we transform Eq. (5.36) to q-variable as follows

$$\begin{aligned}\hat{P}_u^- f &= -\frac{1}{4\pi\mathrm{i}}\int\limits_{-\pi}^{\pi}\frac{f(q')dq'}{\tan\frac{u'-u+\mathrm{i}0}{2}}u_{q'}dq'\\ &= -\frac{1}{4\pi\mathrm{i}}\int\limits_{-\pi}^{\pi}\frac{f(q')\left[1+L^2\tan\frac{q'+\mathrm{i}0}{2}\tan\frac{q}{2}\right]dq'}{\tan\frac{q'+\mathrm{i}0}{2}-\tan\frac{q}{2}}\frac{1}{\cos^2\frac{q'}{2}\left(1+L^2\tan^2\frac{q'}{2}\right)}.\end{aligned}\tag{5.37}$$

Similar to Eq. (5.29) we write $f(q)$ in q space as follows

$$f(u)\equiv f(q)=f^{+,q}(q)+f^{-,q}(q)+f_{0,q},\tag{5.38}$$

where

$$f^{+,q}(q)=\sum_{k=1}^{\infty}f_k\exp\left(\mathrm{i}kq\right)\tag{5.39}$$

is analytic function in $\mathbb{C}^+$ and

$$f^{-,q}(q)=\sum_{k=-\infty}^{-1}f_k\exp\left(\mathrm{i}kq\right)\tag{5.40}$$

is the analytical function in $\mathbb{C}^-$ and $f_{0,q}$ is the zero Fourier harmonic $f_{0,q}=\frac{1}{2\pi}\int\limits_{-\pi}^{\pi}f(q)dq$.

We evaluate integrals in Eq. (5.37) using (5.38) by closing complex contours in $q\in\mathbb{C}^+$ for $f^+(q)$ and $q\in\mathbb{C}^-$ for $f^-(q)$, respectively as shown in Fig. 5.4. For $f_{0,q}$ it can be done in both ways giving the same result. The zeros of the denominator are located at $q'=q-\mathrm{i}0$ and $q'=\pm2\arctan\frac{\mathrm{i}}{L}$. We calculate the residues to obtain:

$$\begin{aligned}\hat{P}_u^- f^{+,q}(q) &= -\frac{2\pi\mathrm{i}}{4\pi\mathrm{i}}\frac{f^{+,q}(2\arctan\frac{\mathrm{i}}{L})\left[1+L^2\frac{\mathrm{i}}{L}\tan\frac{q}{2}\right]}{\frac{\mathrm{i}}{L}-\tan\frac{q}{2}}\frac{1}{\mathrm{i}L}=\frac{1}{2}f^{+,q}\left(2\arctan\frac{\mathrm{i}}{L}\right),\\ \hat{P}_u^- f^{-,q}(q) &= \frac{2\pi\mathrm{i}}{4\pi\mathrm{i}}\frac{f^{-,q}(q)\left[1+L^2\tan\frac{q}{2}\tan\frac{q}{2}\right]}{\frac{1}{2\cos^2\frac{q}{2}}}\frac{1}{\cos^2\frac{q}{2}\left(1+L^2\tan^2\frac{q}{2}\right)}\\ &+\frac{2\pi\mathrm{i}}{4\pi\mathrm{i}}\frac{f^{-,q}(-2\arctan\frac{\mathrm{i}}{L})\left[1+L^2\frac{-\mathrm{i}}{L}\tan\frac{q}{2}\right]}{\frac{-\mathrm{i}}{L}-\tan\frac{q}{2}}\frac{1}{-\mathrm{i}L}=f^{-,q}(q)-\frac{1}{2}f^{-,q}\left(-2\arctan\frac{\mathrm{i}}{L}\right),\\ \hat{P}_u^- f_{0,q} &= \frac{1}{2}f_{0,q}.\end{aligned}$$

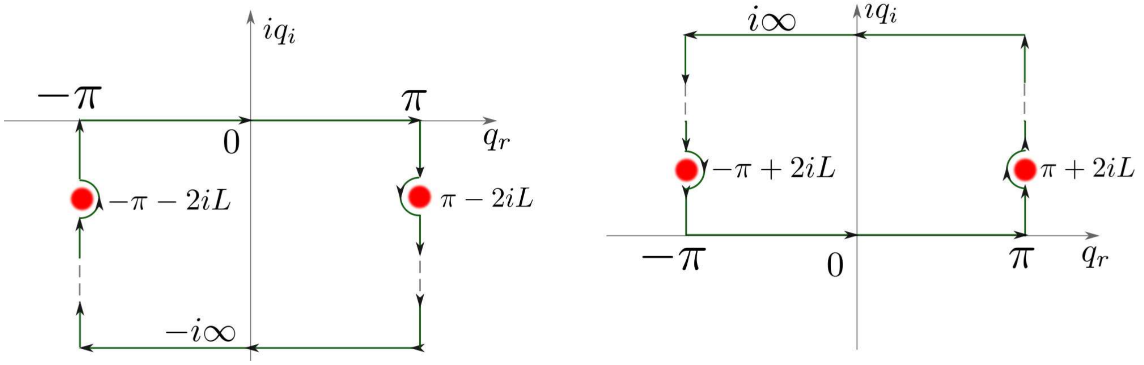

Figure 5.4: A schematic of the integration contours in $q \in \mathbb{C}^-$ (left panel) and $q \in \mathbb{C}^+$ (right panel) used for evaluating different parts of the integral in Eq. (5.37). These contours bypass from inside (by pairs of infinitesimal half-circles) the singularities (5.10) of the conformal map (5.3) at points $q = \pm 2 \arctan(\mathrm{i}/L) \pm \pi = \pm 2\mathrm{i}L \pm \pi + O(\mathrm{i}L^3)$ (shown by filled circles). Vertical parts of contours are canceled out during integration by the periodicity of the integrand.

(5.41)

Using equations (5.38) and (5.41) yields:

$$\hat{P}_u^- f(q) = \frac{f_{0,q}}{2} + f^{-,q}(q) - \frac{1}{2} f^{-,q}\left(-2\arctan\frac{\mathrm{i}}{L}\right) + \frac{1}{2} f^{+,q}\left(2\arctan\frac{\mathrm{i}}{L}\right). \tag{5.42}$$

Defining the projector $\hat{P}_q^-$ in q space similar to Eq. (5.33) as

$$\hat{P}_q^- f = \frac{f_{0,q}}{2} + f^-(q), \tag{5.43}$$

we obtain from Eq. (5.42) that

$$\hat{P}_u^- f(q) = \hat{P}_q^- f + c_{shift}, \tag{5.44}$$

where

$$c_{shift} := -\frac{1}{2} f^{-,q}\left(-2\arctan\frac{\mathrm{i}}{L}\right) + \frac{1}{2} f^{+,q}\left(2\arctan\frac{\mathrm{i}}{L}\right) \tag{5.45}$$

is the constant. We define $\hat{H}_q$ through a relation similar to Eq. (5.28) in q space

$$\hat{P}_q^- = \frac{1}{2}(1 + \mathrm{i}\hat{H}_q), \tag{5.46}$$

and we obtain from Eq. (5.44) and (5.46) that

$$\hat{H}_u^- f(q) = \hat{H}_q^- f - 2\mathrm{i}c_{shift}. \tag{5.47}$$

Thus the operators $\hat{P}^-$ and $\hat{H}$ in u and q spaces are the same except for the shift by a constant c_{shift} and $-2\mathrm{i}c_{shift}$ respectively. These constants result from the singularities (5.10) of the conformal map (5.3). The explicit expression for c_{shift} is calculated from the values of $f^{-,q}(q)$ as follows. We notice that for Stokes wave $y(u)$ is an even real function, $y(u) = y(-u) \in \mathbb{R}$, which implies that $y(q) = y(-q) \in \mathbb{R}$ in q variable. By taking $f(q) = y(q)$ we obtain that $f^{+,q}(q) = f^{-,q}(-q)$. The analytical continuation of $f^{-,q}(q)$ from the real line $q = Re(q)$ into the complex value $q = -2\arctan\frac{\mathrm{i}}{L}$ is trivially done by plugging the complex value of q into the series (5.40) reducing Eq. (5.45) to

$$c_{shift} = 0 \tag{5.48}$$

for the even real function $y(q)$. For more general non-even solution of Eq. (5.26) (corresponds to higher order progressive waves, which have more than one different peaks per 2π spatial period [101]) we generally obtain nonzero value of c_{shift} by a similar procedure as follows. We recover $f^{+,q}(q)$ from $f^{-,q}(q)$ using the identity

$$f^{+,q}(q) = \bar{f}^{-,q}(-q), \tag{5.49}$$

which follows from the condition that $f(u)$ is the real-valued function. Here $\bar{f}(q)$ means the complex conjugation of the function $f(q)$ for real values of q, i.e. $\bar{f}(q) \equiv \overline{f(\bar{q})}$ for complex values of q. For Eq. (5.40) it implies that $\bar{f}^{-,q}(q) = \sum\limits_{k=-\infty}^{-1} \bar{f}_k \exp(-\mathrm{i}kq)$. Then c_{shift} results from the analytical continuation of $f^{-,q}(q)$ and $\bar{f}^{-,q}(q)$ from the real line into $q = -2\arctan\frac{\mathrm{i}}{L}$ together with Eqs. (5.45) and (5.49).

Note that we do not need the explicit value for c_{shift} to solve Eqs. (5.23) and (5.26) because they both include derivatives over q which removes c_{shift}. However, to obtain $x(u)$ one generally needs the value of c_{shift} (which produces only a trivial shift in the horizontal direction). Using Eqs. (5.3), (5.47), (5.45), we transform Eq. (5.21) into the variable q as follows

$$x = u(q) - \hat{H}_u y = u(q) - \hat{H}_q y - 2\mathrm{i}c_{shift}. \tag{5.50}$$

We conclude that this section has justified the derivation of Eqs. (5.23) and (5.26) from Eq. (5.14).

5.4 Numerical Algorithm for Computing Stokes Wave in q Variable

We solve Eq. (5.26) numerically using the generalized Petviashvili method (GPM) and the Newton Conjugate Gradient method similar to solving Eq. (5.14) described in Chapter 3. For both methods $y(q)$ is expanded in cosine Fourier series and the operator $\hat{k}_q$ (5.24) is evaluated numerically using Fast Fourier Transform (FFT) on the uniform grid with N_q points discretization of the interval $-\pi \le q < \pi$.

As alternative to solving Eq. (5.26), we also numerically solved the equivalent equation

$$c^2 \tilde{z}_q = 2\hat{P}_q^-[\mathrm{Im}[\tilde{z}](u_q + \tilde{z}_q)], \tag{5.51}$$

which is the analog of equation (2.22) given here one more time (we put g=1 here):

$$c^2 \tilde{z}_u = 2\hat{P}_u^-[\mathrm{Im}[\tilde{z}](1 + \tilde{z}_u)], \tag{5.52}$$

Eq. (5.52) is equivalent to Eq. (5.14) and is obtained by applying the projector operator $\hat{P}_u^-$ (5.28) to equation (5.14) together with the condition (5.22).

In a similar way. Eq. (5.51) is obtained by applying the projector operator $\hat{P}_q^-$ (5.46) to equation (5.26) together with the condition (5.27).

Solving Eq. (5.51) numerically instead of Eq. (5.26) typically provides 1-2 extra digits of accuracy in Stokes wave height H as well as in the accuracy of the solution spectrum and v_c. The extra cost is however that we have to solve Eq. (5.51) for the complex-valued function $\tilde{z}(q)$ instead of the real valued function $y(q)$ in Eq. (5.26) which doubles the number of numerical operations.

After we obtain a numerical solution for $z(q)$, we use it to determine the value of v_c via one of three numerical methods:

(i) The first method uses a least squares fit of Fourier spectrum of a solution $\tilde{z}$ to the asymptotic series described in Section 3.5.1. Working in u variable this method allows one to obtain v_c with the absolute accuracy about $10^{-10} - 10^{-11}$ in double precision (DP) using 7-12 terms in the series of Eq. (3.14). While working in q variable, the second singularity (5.10) located at $q = q_+ = \pm\pi + 2\mathrm{i}L + O(\mathrm{i}L^3)$ introduces a contribution to the Fourier spectrum of the same order as the main singularity (5.7) (located at $q = \mathrm{i}q_c \simeq \mathrm{i}v_c/L$) if the parameter L is chosen close to $L_{optimal} \simeq (v_c/2)^{1/2}$ (5.12), so we typically can get only 1-2 digits of precision in v_c. In order to obtain v_c with higher accuracy one needs to remap the solution via Fourier interpolation to a uniform grid for the new variable $\tilde{q}$ with the larger value of the parameter $\tilde{L}$ (we found that a factor 8 or 16 is typically enough to obtain v_c with maximum possible accuracy in DP). This pushes the second singularity much further away from the real line compared to the first one so that the main contribution to the tail of Fourier spectrum in $\tilde{q}$ space comes from the first singularity (at a distance $\simeq v_c/\tilde{L}$ from the real line) which will allow us to find $v_c/\tilde{L}$ (and consequently v_c) using the same fitting procedure as in u space. Using this approach for solutions in q space we were able to recover v_c with absolute accuracy about $10^{-9} - 10^{-10}$ in DP. We typically used it for solution with $N_q < 10^5$ Fourier harmonics since Fourier interpolation procedure uses $O(N_q^2)$ operations and becomes slow for larger N_q.

(ii) The second method is described in Section 3.5.3 or Section 6.1 of Ref. [82] and based on the compatibility of the series expansions at points $\zeta = \pm \mathrm{i}\chi_c$ in the axillary space $\zeta = \tan[\frac{w}{2}]$ (which implies that $\chi_c = \tanh[\frac{v_c}{2}]$) with the equation (5.14) of Stokes wave. Current realization of this algorithm also requires Padé approximation of the solution in the axillary space ζ (described in Section 4 of Ref. [81]) for calculation of coefficients of series expansion at the point $\zeta = -\mathrm{i}\chi_c = -\tan[\frac{\mathrm{i}v_c}{2}]$. This method is so far the most accurate but requires $O(N_q \times N_d)$ operations (N_d is the number of poles) for finding Padé approximation of a solution thus slow for large N_q. We typically used that method for $N_q > 10^5$, where the small value of v_c required us to use quad precision with 32 digits accuracy both to obtain $\tilde{z}$ and recover v_c. The absolute accuracy for v_c in this method was $\sim 10^{-26}$.

(iii) The third method was described in Section 3.5.2 and uses nonlinear fit of the crest of a solution to a series expansion. One can work in either q space to find v_c/L or u space to find directly v_c. The method was used as the substitute to method (ii) for the smallest values $v_c \lesssim 10^{-10}$ we achieved, where Padé approximation become computationally challenging taking more computer time than the calculation of $\tilde{z}$ itself. The absolute accuracy of that method for v_c is $\sim 10^{-20}$ in quad precision (QP).

To summarize, we used the first two methods for finding v_c for solution with $v_c > 10^{-8}$ in double precision (DP) and quad precision (QP), the second method for solutions with $v_c \gtrsim 10^{-10}$ in QP and the third method for solution with $v_c \lesssim 10^{-10}$ (with $N_q \gtrsim 10^6$) in QP. We also performed a multiprecision simulations with a variable precision arithmetics with ~ 200 digits for selected values of parameters as described in the next Section.

Chapter 6

New Results on Stokes Wave

Previous results summarized in Fig. 2 of Ref. [81] (they are also reproduced in the left part of the curve of Fig. 6.1) showed a nontrivial dependence of the Stokes wave speed c on the height H with H monotonically approaching the maximum value H_{max} and c approaching a finite value non-monotonically while oscillating with an amplitude that decreases approximately two orders in magnitude every half of such oscillation. Computing Stokes wave solutions in u space as in Ref. [81] allowed to resolve about 1.5 of such oscillations (see Fig. 6.1) while implementing the approach described in here (solving in q space) allowed to resolve about 3.5 of such oscillations.

One example of the numerical solution (corresponds to the most extreme wave of Ref. [81]) is given in the Chapter 4. Another example of a less steep wave solution for $c = 1.0924$ computed using double precision resulting in $H/\lambda = 0.1404429731116977$ and $v_c = 0.0006925714\ldots$ is given in Fig. 6.2 in variables u (left panel) and q (right panel) with the corresponding spectra of $\tilde{z}(u)$ and $\tilde{z}(q)$ showed in Fig. 6.3 (both spectra have only negative components of k since both $\tilde{z}(w)$ and $\tilde{z}(q)$ are holomorphic in $\mathbb{C}^{-}$). Here $N = 64536$ on a uniform grid and $N_q = 1024$ on a nonuniform grid with $L = 0.018608751114420542$. It demonstrates that for this particular case one

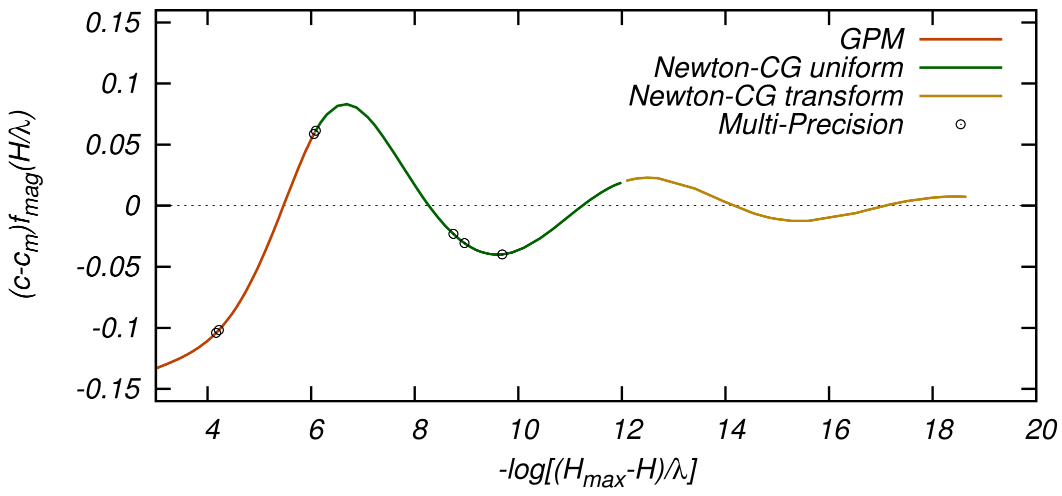

Figure 6.1: Illustration of performance of the numerical methods applied to Eq. (5.26): (red) waves accessible by means of Generalized Petviashvili method (GPM), (green) waves accessible via Newton–Conjugate Gradient method (Newton-CG) on a uniform grid u, and (gold) waves accessible via Newton-CG method on nonuniform grid with the new conformal map (5.2). Open circles mark positions of selected Stokes waves separately computed in multiprecision (200 digits) using *Wolfram Mathematica* software. The plot is scaled by a magnification function $f_{mag}(H/\lambda) = 1/(30(H_{max} - H)/\lambda)^{1.15} + 1$ to show all simulation data in a single graph while stressing obtained oscillations.

needs 64 times less Fourier harmonics in q space compared to the u space in order to resolve the solution up to DP round-off error. The speed up factor could be roughly estimated as $1/L = (v_c/2)^{1/2}$ that becomes significant as we go to lower values of v_c.

High precision and range of our simulation parameters allow to reveal the asymptotic behavior of Stokes wave as it approaches the limiting form as well as make a comparison with the theory of Stokes wave. We start by analyzing the dependencies of wave speed c and height H on the parameter χ_c for the obtained family of Stokes waves, where

$$\chi_c = \tanh[\frac{v_c}{2}] \tag{6.1}$$

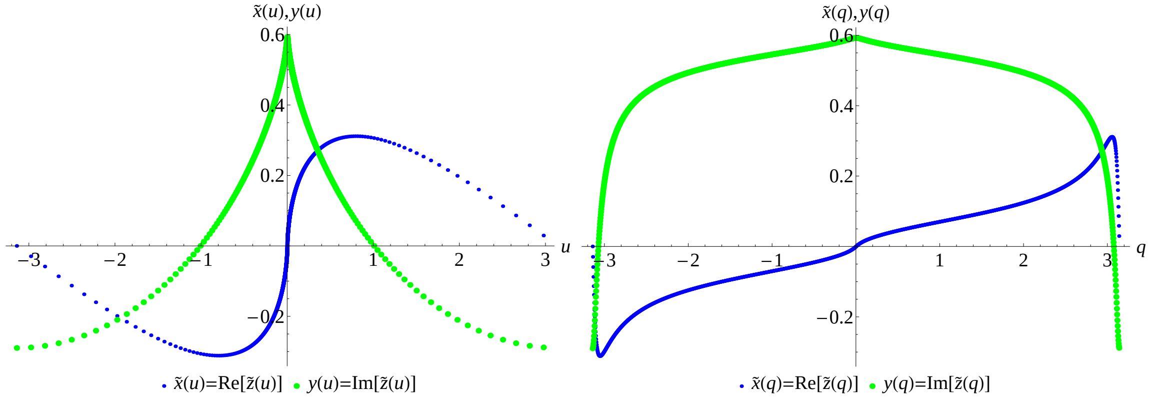

Figure 6.2: Real and imaginary parts of the Stokes wave solution $\tilde{z} = \tilde{x} + iy$ for $H/\lambda = 0.1404429731116977$ and $c = 1.0924$ in u (left) and q (right) variables. It is seen that the gradients of $\tilde{z}$ are significantly reduced in q variable.

is the distance to the singularity of a Stokes wave solution to the real line in the axillary space $\zeta = \tan[\frac{w}{2}]$. Notice, that for the highly nonlinear Stokes waves $v_c \to 0$ and $\chi_c \simeq v_c/2$, while for the almost linear Stokes waves $v_c \to \infty$ and $\chi_c \to 1$. Fig. 6.4 shows $|c_{lim} - c|$ and $(H_{max} - H)/\lambda$ vs. χ_c for computed Stokes waves in the log-log scale together with the corresponding fitting curves. Here c_{lim} and H_{max}/λ are the speed and the scaled height of the limiting Stokes waves, respectively. We

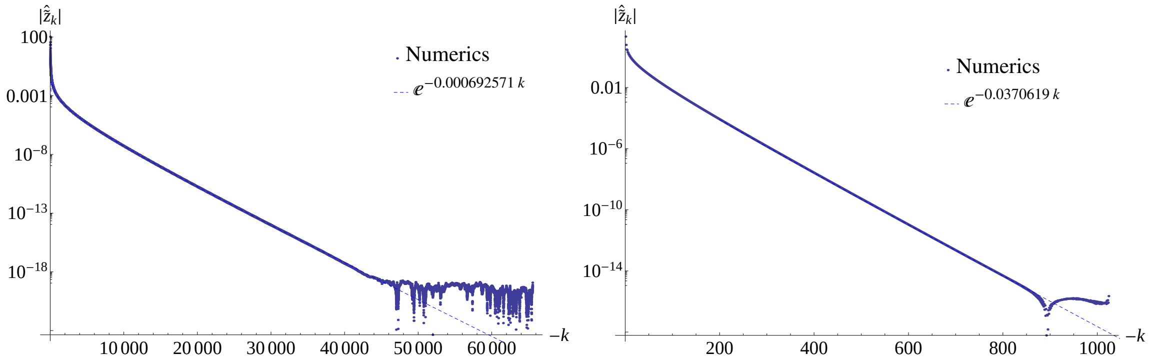

Figure 6.3: Spectra of the Stokes wave for $\tilde{z} = \tilde{x} + iy$ with $H/\lambda = 0.1404429731116977$, $c = 1.0924$ in w (left) and q (right) variables calculated in DP.

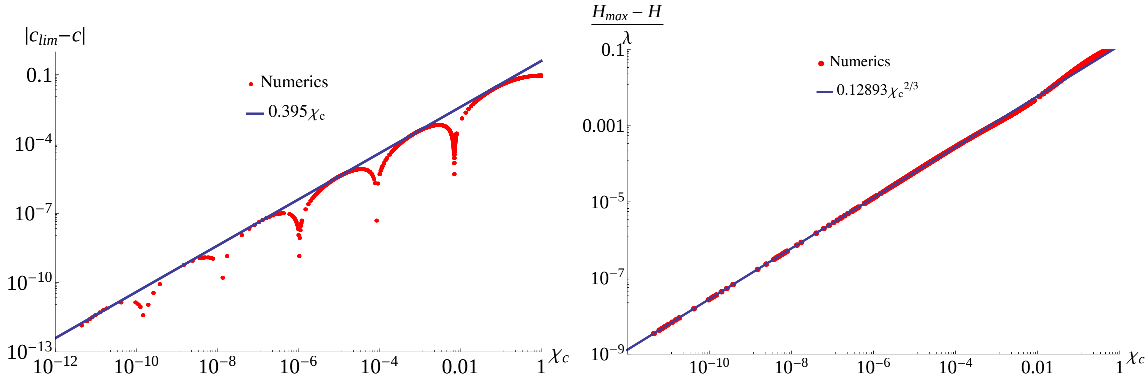

Figure 6.4: Dependencies of $|c_{lim} - c|$ (left panel) and $\frac{H_{max}-H}{\lambda}$ (right panel) as functions of the parameter χ_c, where $|c_{lim} - c|$ is deviation of the velocity c of the Stokes wave from the velocity of the limiting Stokes wave c_{lim} and $\frac{H_{max}-H}{\lambda}$ is the deviation of the Stokes wave height H the height H_{max} of the limiting Stokes wave. The red dots are simulation data while the solid lines are their corresponding fits.

use the numerical values $c_{lim}^{GL} = 1.0922850485861$ and $H_{max}^{GL}/\lambda = 0.1410634839798$ found by I.S. Gandzha and V. P. Lukomsky in Ref. [102] with the claimed accuracy of 11 digits. Comparable accuracy was also achieved in Ref. [103]. It is seen from Fig. 6.4 (left) that $|c_{lim} - c|$ experiences oscillations with their envelope being the excellent fit to the linear law

$$Envelope(c_{lim} - c) \propto \chi_c. \tag{6.2}$$

Fig. 6.4 (right) shows that the dependence of $H_{max} - H$ on χ_c at the leading order fits well to the the power law

$$H_{max} - H \propto \chi_c^{2/3} \tag{6.3}$$

while experiencing small oscillations with the vanishing amplitude as $\chi_c \to 0$. The scaling (6.3) was proposed in Ref. [80] from simulations and can be extracted at the leading order from the analytical Stokes wave solution of Section 8 of Ref. [82]. Using the scaling (6.3) we fit the simulation data into the model

$$H_{max}^{GL} + \Delta H_{max} - H = \lambda A \chi_c^{2/3}, \tag{6.4}$$

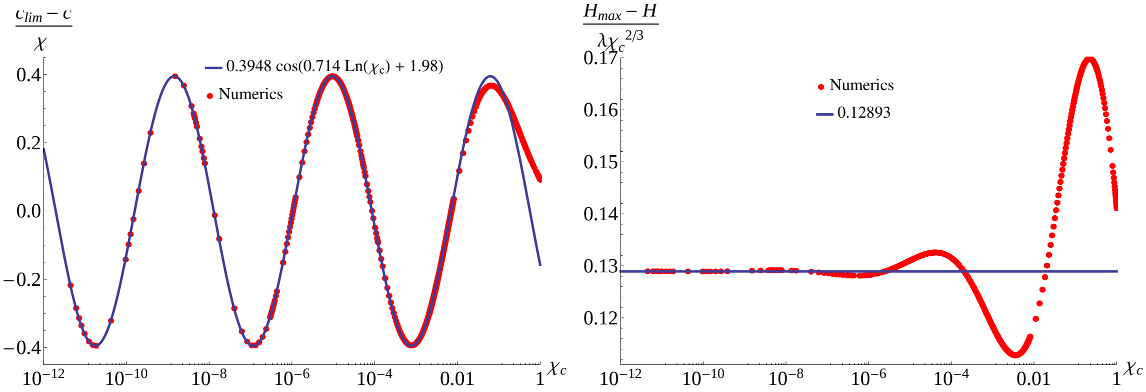

Figure 6.5: Dependencies $\frac{c_{lim}-c}{\chi_c}$ (left panel) and $\frac{H_{max}-H}{\lambda\chi_c^{2/3}}$ (right panel) for Stokes wave as a function of the parameter χ_c. The red dots are simulation data while the solid curves are their corresponding fits.

where the constant ΔH_{max} accounts for the accuracy in the numerical value of H_{max}^{GL} and A is the another fitting parameter. Using the smallest values of $\chi_c \lesssim 10^{-11}$ achieved in simulations, we obtained from that fit the estimate $H_{max}^{fit}/\lambda = (H_{max}^{GL} + \Delta H_{max})/\lambda = 0.141063483980 \pm 10^{-12}$ and $A = 0.12893 \pm 5 \cdot 10^{-5}$, i.e. $\Delta H_{max}/\lambda = 2 \cdot 10^{-13}$ which is consistent with 11 digits accuracy of H_{max}^{GL} (although our precision is higher). The highest wave that we computed in QP has $H_{max}^{lowerbound}/\lambda = 0.1410634805062790\ldots$ (for $c = 1.09228504858750000$) which provides the best lower bound H_{max}/λ from our simulations. That lower bound is within $\simeq 3.5 \times 10^{-9}$ from H_{max}^{fit}/λ which is more than 3 orders in magnitude of improvement compared with the simulations of Ref. [81].

To focus on the corrections beyond the leading order scalings (6.2) and (6.3), we plot $|c_{lim} - c|/\chi_c$ and $(H_{max} - H)/(\lambda\chi_c^{2/3})$ vs. χ_c in Fig. 6.5. It seen on left panel that the simulation data for $(c_{lim} - c)/\chi_c$ are well fit onto the cos-log model

$$\frac{c_{lim} - c}{\chi_c} \simeq \alpha \cos[\omega_1 \ln(\chi_c) + \varphi_1]. \tag{6.5}$$

with $\alpha = 0.394794 \pm 10^{-6}$, $\omega_1 = 0.71430 \pm 10^{-5}$, $\varphi_1 = 1.98059 \pm 2 \cdot 10^{-5}$ and $c_{lim}^{fit} = 1.0922850485865375 \pm 10^{-16}$. This value of c_{lim} is consistent with 11 digits accuracy of c_{lim}^{GL} (and again our precision is higher). Here we used 4-point "sliding" window along our data points (c, χ_c) to solve for $c_{lim}, \alpha, \omega_1$ and φ_1 while decreasing χ_c and tracking when the maximum number of digits in these parameters stabilize (typically it occurs half of an oscillation before the steepest waves computed (see left panel of Fig. 6.5) due to the larger round-off error for the smallest χ_c data). For a robust estimate of an error we then slide this 4-point window back into larger χ_c for a half of an oscillation to track the error. One can also do the least square fit of $c_{lim}, \alpha, \omega_1$ and φ_1 into the data points from the left-most ~ 1.5 oscillations which gives 1-2 orders less accurate values than described above.

One can compare Eq. (6.5) with the expression

$$c^2 = 1.1931 - 1.18\epsilon^3 \cos(\kappa \ln \epsilon + 2.22) \tag{6.6}$$

which was obtained by M.S. Longuet-Higgins and M.J.H. Fox in Ref. [15] by matched asymptotic expansions, where $\kappa = 2.142906948499\ldots$ is the solution of the transcendental Eq. $(\kappa\pi/6)\tanh[(\kappa\pi)/6] = \pi/(2\sqrt{3})$ with Ref. [15] used less accurate value $\kappa \simeq 2.143$. Here $\epsilon := 2^{-1/2}q$ and q is the particle speed at the wave crest in a frame of reference moving with the phase speed c. To find q we notice that the complex velocity $V := v_x - \mathrm{i}v_y$ is given by $V = \Pi_u/z_u$, where v_x and v_y are the horizonal and vertical velocities in physical coordinates in the rest frame and Π is complex potential which for Stokes wave is given by $\Pi = c(z - w)$ (see e.g. the Appendix B of Ref.[82]). It implies using the analytic solution of Section 8 of Ref. [82] that $\epsilon = 2^{-1/2}q = 2^{-1/2}|V|_{w=0} - c| = 2^{-1/2}c|(z_u - 1)/z_u - 1||_{w=0} = cP\chi_c^{1/3} + O(\chi_c^{2/3})$, where $P \sim 1$ is the constant. Then it is seen that Eqs. (6.5) and (6.6) are consistent if we additionally notice that $2.143 \ln \epsilon \simeq 0.714 \ln \chi_c + const$ which is within the accuracy of the numerical value $\omega_1 = 0.71430$ in the parameter fit of Eq. (6.5). In addition, the coefficient 1.1931 in right-hand side of Eq. (6.6) is the numerical approximation of Ref. [15] for c_{lim}^2. Thus Fig. 6.5 reproduces 3 oscillations of Eq. (6.6). More oscillations can be obtained by increasing the numerical precision with the total number of oscillation being infinite as follows from Ref. [15], see also Refs. [104] and [105] for the another examples of the bifurcation diagram with an infinite number of oscillations. Notice that motivated by Eq. (6.6) we can replace Eq. (6.5) fit by the fit to Eq. $(c_{lim} - c)/\chi_c = \alpha \cos[(\kappa/3)\ln(\chi_c) + \varphi_1]$ (i.e. replace ω_1 by the exact value $\kappa/3$) and use 3-point sliding window on our data (c, χ_c) to find a new fit $\varphi_1 = 1.980587 \pm 10^{-6}$, $\alpha = 0.394794 \pm 10^{-6}$, $c_{lim}^{fit} = 1.0922850485865375 \pm 10^{-16}$, which is one extra digit accuracy improvement for φ_1 compared with 4-point window.

The definition of the Stokes wave height is $H = y(0) - y_b$, where $y_b := y(\pm\pi)$. Then the analytical Stokes wave solution of Section 8 of Ref. [82] implies that the next correction beyond the leading order model (6.4) is given by

$$H_{max}^{GL} + \Delta H_{max} - H - \lambda A \chi_c^{2/3} = \frac{\left(c_{lim}^{GL}\right)^2 - c^2}{2} - (y_{b,lim} - y_b), \tag{6.7}$$

where $y_{b,lim} \simeq y_{b,lim} = -0.28978469623945005 \pm 5 \cdot 10^{-17}$ is the value of y_b for the limiting Stokes wave (we approximate $y_{b,lim}$ by a fit of Eq. $y_b(\chi_c) = y_{b,lim} + A_b \chi_c \cos[(\kappa/3)\ln\chi_c + \varphi_b]$ into our numerical data for (y_b, χ_c) for the most extreme waves with numerical fitting values $A_b = 0.4509134 \pm 10^{-7}$ and $\varphi_b = 0.779081 \pm 10^{-6}$). To check the accuracy of Eq. (6.7) we divided it by $\lambda\chi_c$ and compared the right-hand side with the left-hand side on right panel of Fig. 6.6 showing excellent agreement. Oscillations both in $c^2(\chi_c)$ (as seen on left panel of Fig. 6.5) and in $y_b(\chi_c)$ are comparable in amplitude both contributing to that agreement. Inspired by the model (6.5), we fit the data $H(\chi_c)$ to the following model $H_{max}^{GL} + \Delta H_{max} - H(\chi_c) - A\chi_c^{2/3} \simeq B\chi_c \cos[\omega_2 \ln(\chi_c) + \varphi_2]$, where $\Delta H_{max}, A, B, \omega_2, \varphi_2$ are unknown constants. Using 5-point sliding window technique similar to the one above, we obtained that $\Delta H_{max}/\lambda = -1.3 \times 10^{-13} \pm 10^{-14}$, $A = 0.128959 \pm 10^{-6}$, $B = 0.1158 \pm 10^{-4}$, $\omega_2 = 0.714 \pm 10^{-3}$, $\varphi_2 = 1.36 \pm 0.01$. This model fit is shown on right panel of Fig. 6.6 by the solid curve. Notice, that $|\omega_1| \approx |\omega_2|$. We expect that if the suggested models are correct then $|\omega_1|$ should be equal to $|\omega_2|$ as $\chi_c \to 0$. Notice that if use the exact value $\omega_2 = \kappa/3$ then $\Delta H_{max}/\lambda = -1.3 \cdot 10^{-13} \pm 10^{-14}$, $A = 0.1289596 \pm 10^{-7}$,

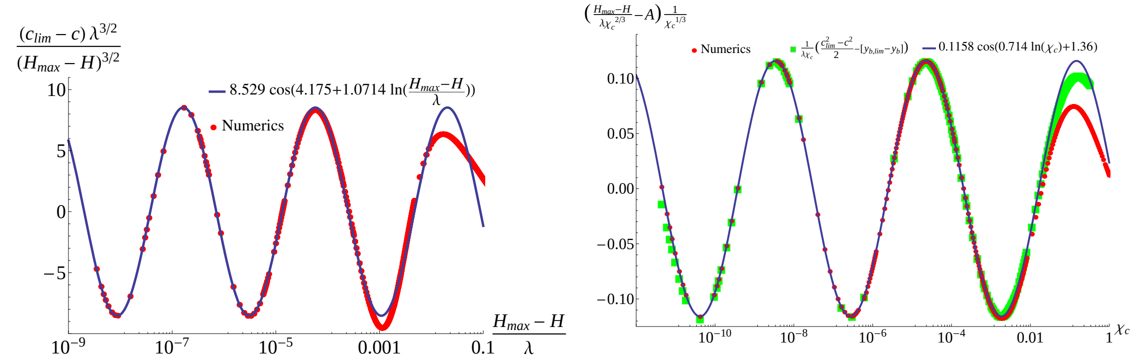

Figure 6.6: Dependencies $\frac{(c_{lim}-c)\lambda}{(H_{max}-H)^{3/2}}$ vs. $\frac{H_{max}-H}{\lambda}$ (left panel) and $\left(\frac{H_{max}-H}{\lambda\chi_c^{2/3}}-A\right)\frac{1}{\chi_c^{1/3}}$ vs. χ_c (right panel) with $A = 0.128959$. The red dots are data points obtained from Stokes wave simulations while the solid curves are their corresponding fits.

$B = 0.11583 \pm 2\cdot 10^{-5}$ and $\varphi_2 = 1.3645 \pm 10^{-4}$ which results in the improved estimate $H_{max}^{fit_2}/\lambda = 0.14106348397993 \pm 10^{-14}$ compared with H_{max}^{fit}/λ.

It is also instructive to relate the physical variables $H_{max} - H$ and $c_{lim} - c$ directly bypassing the use of χ_c. Via Eq. (6.4) we approximate χ_c at the leading order through $H_{max}^{GL} - H$. We plug in that approximation into Eq. (6.5) to obtain at the leading order that

$$\begin{aligned}&(c_{lim}-c)\lambda^{3/2}/(H_{max}-H)^{3/2}\\&\simeq \alpha A^{-3/2}\cos\left[(3\omega_1/2)\ln[(H_{max}^{fit_2}-H)/\lambda]-(3\omega_1/2)\ln A+\varphi_1\right].\end{aligned} \tag{6.8}$$

Left panel of Fig. 6.6 shows $(c_{lim}^{fit}-c)\lambda^{3/2}/(H_{max}^{fit_2}-H)^{3/2}$ vs. $(H_{max}^{fit_2}-H)/\lambda$ together with the model $(c_{lim}^{fit}-c)\lambda^{3/2}/(H_{max}-H)^{3/2} \simeq D\cos\left(\omega_3\ln[(H_{max}^{fit_2}-H)/\lambda]+\varphi_3\right)$. The fitting constants of the model are $D = 8.53 \pm 0.01$, $\omega_3 = 1.071 \pm 10^{-3}$ and $\varphi_3 = 4.17 \pm 0.01$ being consistent with the leading order expression (6.8). Assuming additionally that $\omega_3 = \kappa/2$ in our fit, we obtain the improved estimate $D = 8.529 \pm 0.005$ and $\varphi_3 = 4.175 \pm 10^{-3}$.

From the obtained above Stokes solutions we also found the maximum of the absolute value of the slope $\eta_{max} \equiv \max_x|\eta_x| = \max_u|y_u/x_u|$. For the most extreme wave in our calculation we found $\arctan(\eta_{max}) = 30.3787030817^\circ \ldots$ which is consistent with the slope value 30.3787032466° of Ref. [106] (obtained based of the Nekrasov's integral equation [107]).

Chapter 7

Conclusions and Discussion

This work was continuation of the previous work done by our research group. We found a new transformation (5.2) which allows to move the lowest complex singularity $w = \mathrm{i}v_c$ of the function $f(u)$ away from the real line to $q = \mathrm{i}\sqrt{2v_c}$ thus greatly improving the efficiency of Fourier series representation of that function in the new variable q. Number of Fourier modes needed to reach the same precision of approximation of the Stokes wave solution in q variable is reduced by the factor $\sim {v_c}^{-1/2}$ for $v_c \ll 1$ compared to Fourier series in u. We showed that the new transformation (5.2) is consistent with the dynamics of two dimensional Euler equation with free surface. We demonstrated the efficiency of Eq. (5.2) for simulations of Stokes wave by improving the numerical performance by many orders of magnitude. It allowed us to reveal the details of the oscillatory behaviour of the parameters of Stokes wave as it approaches the limiting wave. In particular, we were able to recover 3 oscillation in such dependencies as wave speed c vs. wave steepness H/λ, as well as c vs. v_c and H/λ vs. v_c.

We hope that this approach of analysing problems of hydrodynamics from standpoint of complex singularities of their solutions can be beneficial to further advance the understanding of the problems in this area as well as developing efficient numerical methods that are used to solve them. Similar approach and numerical techniques can be used to resolve solutions with multiple singularities or singularities of different types in other problems of hydrodynamics and in other areas of computational mathematics.

The obtained high precision Stokes wave can be used to study stability of Stokes waves beyond less extreme waves used in Ref. [108].

We were also able to analyze Stokes wave branch cut density $\rho(\chi)$ using different approaches. One of the future areas of research might be finding an effective numerical method for solving a closed set of Stokes wave equations in terms of $\rho(\chi)$ or in terms of Pade approximants.

We are planning on continuing to develop numerical tools for analysis of solutions with singularities as well as developing adaptive non-uniform grids (or conformal maps) tailored to solutions with specific singularities.

References

[1] M. V. Goldman and D. F. Du Bois. Stimulated incoherent scattering of light from plasmas. *Physics of Fluids*, 8(7):1404–1405, 1965.

[2] Harvey A. Rose and David A. Russell. A self-consistent trapping model of driven electron plasma waves and limits on stimulated raman scatter. *Physics of Plasmas*, 8(11):4784–4799, 2001.

[3] Ira B. Bernstein, John M. Greene, and Martin D. Kruskal. Exact nonlinear plasma oscillations. *Phys. Rev.*, 108:546–550, Nov 1957.

[4] Harvey A. Rose. Langmuir wave self-focusing versus decay instability. *Physics of Plasmas*, 12(1):012318, 2005.

[5] Denis A. Silantyev, Pavel M. Lushnikov, and Harvey A. Rose. Langmuir wave filamentation in the kinetic regime. I. Transverse instability of Bernstein-Greene-Kruskal modes and multidimensional Vlasov simulations. *Physics of Plasmas*, 24(4):042104, 2017.

[6] Denis A. Silantyev, Pavel M. Lushnikov, and Harvey A. Rose. Langmuir wave filamentation in the kinetic regime. II. Weak and strong pumping of nonlinear electron plasma waves as the route to filamentation. *Physics of Plasmas*, 24(4):042105, 2017.

[7] P. M. Lushnikov, H. A. Rose, D. A. Silantyev, and N. Vladimirova. Vlasov multi-dimensional model dispersion relation. *Phys. of Plasmas*, 21:072103, 2014.

[8] George G. Stokes. Supplement to a paper on the theory of oscillatory waves. *Mathematical and Physical Papers*, 1:314–326, 1880.

[9] Vladimir E. Zakharov, Alexander O. Korotkevich, Andrei Pushkarev, and Donald Resio. Coexistence of weak and strong wave turbulence in a swell propagation. *Phys. Rev. Lett.*, 99(16):164501, 2007.

[10] Vladimir E. Zakharov, Alexander O. Korotkevich, and Alexander O. Prokofiev. On dissipation function of ocean waves due to whitecapping. *AIP Proceedings, CP1168*, 2:1229–1231, 2009.

[11] V. E. Zakharov, A. I. Dyachenko, and A. O. Prokofiev. Freak waves as nonlinear stage of Stokes wave modulation instability. *European Journal of Mechanics B/Fluids*, 25:677–692, 2006.

[12] R. C. T. Rainey and Michael S. Longuet-Higgins. A close one-term approximation to the highest Stokes wave on deep water. *Ocean Engineering*, 33:2012–2024, 2006.

[13] S. Dyachenko and A. C. Newell. Whitecapping. *Studies in Applied Mathematics*, 137(2):199–213, 2016.

[14] M. S. Longuet-Higgins and M. J. H. Fox. Theory of the almost-highest wave: the inner solution. *J. Fluid Mech.*, 80(4):721–741, 1977.

[15] M. S. Longuet-Higgins and M. J. H. Fox. Theory of the almost-highest wave. part 2. matching and analytic extension. *J. Fluid Mech.*, 85(4):769–786, 1978.

[16] L. W. Schwartz and J. D. Fenton. Strongly nonlinear waves. *Ann. Rev. Fluid. Mech*, 14:39–60, 1982.

[17] N. A. Krall and A. W. Trivelpiece. *Principles of Plasma Physics*. McGraw-Hill Inc., New York, 1973.

[18] E. M. Lifshitz and L.P. Pitaevskii. *Physical Kinetics: Volume 10*. Butterworth-Heinemann, Oxford, 1981.

[19] D. R. Nicholson. *Introduction to Plasma Theory*, volume XII. John Wiley & Sons, New York, 1983.

[20] T. P. Coffey. Breaking of large amplitude plasma oscillations. *The Physics of Fluids*, 14(7):1402–1406, 1971.

[21] R. L. Dewar. Frequency shift due to trapped particles. *Physics of Fluids*, 15(4):712–714, 1972.

[22] R. L. Dewar and J. Lindl. Nonlinear frequency shift of a plasma wave. *The Physics of Fluids*, 15(5):820–824, 1972.

[23] Wallace M. Manheimer and Robert W. Flynn. Formation of stationary large amplitude waves in plasmas. *Physics of Fluids*, 14(11):2393–2396, 1971.

[24] G. J. Morales and T. M. O'Neil. Nonlinear frequency shift of an electron plasma wave. *Phys. Rev. Lett.*, 28:417–420, Feb 1972.

[25] Chang Liu and Ilya Y Dodin. Nonlinear frequency shift of electrostatic waves in general collisionless plasma: Unifying theory of fluid and kinetic nonlinearities. *Physics of Plasmas*, 22(8):082117, 2015.

[26] J. L. Kline, D. S. Montgomery, B. Bezzerides, J. A. Cobble, D. F. DuBois, R. P. Johnson, H. A. Rose, L. Yin, and H. X. Vu. Observation of a transition from fluid to kinetic nonlinearities for langmuir waves driven by stimulated raman backscatter. *Phys. Rev. Lett.*, 94:175003, May 2005.

[27] J. L. Kline, D. S. Montgomery, L. Yin, D. F. DuBois, B. J. Albright, B. Bezzerides, J. A. Cobble, E. S. Dodd, D. F. DuBois, J. C. Fernandez, R. P. Johnson, J. M. Kindel, H. A. Rose, H. X. Vu, and W. Daughton. Different $k\lambda_d$ regimes for nonlinear effects on langmuir waves. *Physics of Plasmas*, 13(5):055906, 2006.

[28] B.J. Winjum, J. Fahlen, and W.B. Mori. The relative importance of fluid and kinetic frequency shifts of an electron plasma wave. *Physics of Plasmas*, 14(10):102104, 2007.

[29] Harvey A. Rose and L. Yin. Langmuir wave filamentation instability. *Physics of Plasmas*, 15(4), 2008.

[30] L. Yin, B. J. Albright, K. J. Bowers, W. Daughton, and H. A. Rose. Saturation of backward stimulated scattering of laser in kinetic regime: Wavefront bowing, trapped particle modulational instability, and trapped particle self-focusing of plasma waves. *Physics of Plasmas*, 15(1), 2008.

[31] R. L. Berger, S. Brunner, J. W. Banks, B. I. Cohen, and B. J. Winjum. Multidimensional vlasov simulations and modeling of trapped-electron-driven filamentation of electron plasma waves. *Physics of Plasmas*, 22(5), 2015.

[32] K. J. Bowers, B. J. Albright, L. Yin, B. Bergen, and T. J. T. Kwan. Ultrahigh performance three-dimensional electromagnetic relativistic kinetic plasma simulationa). *Physics of Plasmas*, 15(5), 2008.

[33] L. Yin, B. J. Albright, H. A. Rose, K. J. Bowers, B. Bergen, D. S. Montgomery, J. L. Kline, and J. C. Fernandez. Onset and saturation of backward stimulated raman scattering of laser in trapping regime in three spatial dimensions. *Physics of Plasmas*, 16(11), 2009.

[34] L. Yin, B. J. Albright, H. A. Rose, D. S. Montgomery, J. L. Kline, R. K. Kirkwood, J. Milovich, S. M. Finnegan, B. Bergen, , and K. J. Bowers. Stimulated scattering in laser driven fusion and high energy density physics experiments. *Physics of Plasmas*, 21:092707, 2014.

[35] David A. Russell, D. F. DuBois, and Harvey A. Rose. Nonlinear saturation of stimulated raman scattering in laser hot spots. *Physics of Plasmas*, 6(4):1294–1317, 1999.

[36] D. S. Montgomery, J. A. Cobble, J. C. Fernandez, R. J. Focia, R. P. Johnson, N. Renard-LeGalloudec, H. A. Rose, and D. A. Russell. Recent trident single hot spot experiments: Evidence for kinetic effects, and observation of langmuir decay instability cascade. *Physics of Plasmas*, 9(5):2311–2320, 2002.

[37] Claire Ellen Max, Jonathan Arons, and A. Bruce Langdon. Self-modulation and self-focusing of electromagnetic waves in plasmas. *Phys. Rev. Lett.*, 33:209–212, Jul 1974.

[38] S. Depierreux, V. Yahia, C. Goyon, G. Loisel, P. E. Masson-Laborde, N. Borisenko, A. Orekhov, O. Rosmej, T. Rienecker, and C. Labaune. Laser light triggers increased Raman amplification in the regime of nonlinear Landau damping. *Nature Communications*, 5:4158, 2014.

[39] Andrew J. Schmitt and Bedros B. Afeyan. Time-dependent filamentation and stimulated brillouin forward scattering in inertial confinement fusion plasmas. *Physics of Plasmas*, 5(2):503–517, 1998.

[40] P. M. Lushnikov and H. A. Rose. How much laser power can propagate through fusion plasma? *Plasma Physics and Controlled Fusion*, 48:1501–1513, 2006.

[41] P. M. Lushnikov and H. A. Rose. Instability versus equilibrium propagation of laser beam in plasma. *Phys. Rev. Lett.*, 92:255003, 2004.

[42] J. W. Banks, 2016. Private communication.

[43] Harvey A. Rose and William Daughton. Vlasov simulation in multiple spatial dimensions. *Physics of Plasmas*, 18(12), 2011.

[44] Y. Kato, K. Mima, N. Miyanaga, S. Arinaga, Y. Kitagawa, M. Nakatsuka, and C. Yamanaka. Random phasing of high-power lasers for uniform target acceleration and plasma-instability suppression. *Phys. Rev. Lett.*, 53:1057–1060, Sep 1984.

[45] J. D. Lindl, P. Amendt, R. L. Berger, S. H. Glenzer S. G. Glendinning, S. W. Haan, R. L. Kauffmanand O. L. Landen, and L. J. Suter. The physics basis for ignition using indirect-drive targets on the National Ignition Facility. *Phys. Plasmas*, 11:339–491, 2004.

[46] N. B. Meezan, L. J. Atherton, D. A. Callahan, E. L. Dewald, S. Dixit, E. G. Dzenitis, M. J. Edwards, C. A. Haynam, D. E. Hinkel, O. S. Jones, O. Landen, R. A. London, P. A. Michel, J. D. Moody, J. L. Milovich, M. B. Schneider, C. A. Thomas, R. P. J. Town, A. L. Warrick, S. V. Weber, K. Widmann, S. H. Glenzer, L. J. Suter, B. J. MacGowan, J. L. Kline, G. A. Kyrala, and A. Nikroo. National Ignition Campaign Hohlraum energetics. *Phys. Plasmas*, 17:056304, 2010.

[47] James Paul Holloway and J. J. Dorning. Undamped plasma waves. *Phys. Rev. A*, 44:3856–3868, Sep 1991.

[48] Mark Buchanan and J. Dorning. Nonlinear electrostatic waves in collisionless plasmas. *Phys. Rev. E*, 52:3015–3033, Sep 1995.

[49] Thomas O'Neil. Collisionless damping of nonlinear plasma oscillations. *Physics of Fluids*, 8(12):2255–2262, 1965.

[50] A. A. Vlasov. The vibrational properties of an electron gas. *Soviet Physics Uspekhi*, 10(6):721, 1968.

[51] L. D. Landau. On the vibrations of the electronic plasma. *J. Phys.(USSR)*, 10:25–34, 1946. [Zh. Eksp. Teor. Fiz.16,574(1946)].

[52] B. D. Fried, M. Gell-Mann, J. D. Jackson, and H. W. Wyld. Longitudinal plasma oscillations in an electric field. *Journal of Nuclear Energy. Part C, Plasma Physics, Accelerators, Thermonuclear Research*, 1(4):190–198, 1960.

[53] D. S. Montgomery, R. J. Focia, H. A. Rose, D. A. Russell, J. A. Cobble, J. C. Fernández, and R. P. Johnson. Observation of stimulated electron-acoustic-wave scattering. *Phys. Rev. Lett.*, 87:155001, Sep 2001.

[54] Carlo Lancellotti and J. J. Dorning. Critical initial states in collisionless plasmas. *Phys. Rev. Lett.*, 81:5137–5140, Dec 1998.

[55] R. L. Berger, S. Brunner, T. Chapman, L. Divol, C. H. Still, and E. J. Valeo. Electron and ion kinetic effects on non-linearly driven electron plasma and ion acoustic waves. *Physics of Plasmas*, 20(3):032107, 2013.

[56] W. L. Kruer, J. M. Dawson, and R. N. Sudan. Trapped-particle instability. *Phys. Rev. Lett.*, 23:838, 1969.

[57] C.Z Cheng and Georg Knorr. The integration of the vlasov equation in configuration space. *J. of Comp. Phys.*, 22(3):330–351, 1976.

[58] J. W. Banks, R. L. Berger, S. Brunner, B. I. Cohen, and J. A. F. Hittinger. Two-dimensional vlasov simulation of electron plasma wave trapping, wavefront bowing, self-focusing, and sidelossa). *Physics of Plasmas*, 18(5), 2011.

[59] V. E. Zakharov. Collapse of langmuir waves. *Sov. Phys. JETP*, 35:908, 1972.

[60] V. E. Zakharov. Collapse of langmuir waves. *Zh. Eksp. Teor. Fiz.*, 62:1745, 1972.

[61] H. Yoshida. Construction of higher order sympletic integrators. *Phys. Lett. A.*, 150:262–268, 1990.

[62] F. Neri. Lie algebras and canonical integration. *Department of Physics, University of Maryland, preprint*, 1988.

[63] Q. Sheng. Solving linear partial differential equations by exponential splitting. *IMA Journal of Numerical Analysis*, 9(2):199–212, 1989.

[64] Masuo Suzuki. General theory of fractal path integrals with applications to many-body theories and statistical physics. *Journal of Mathematical Physics*, 32(2):400–407, 1991.

[65] Daniel Goldman and Tasso J. Kaper. Nth-order operator splitting schemes and nonreversible systems. *SIAM Journal on Numerical Analysis*, 33(1):349–367, 1996.

[66] Sergio Blanes and Fernando Casas. On the necessity of negative coefficients for operator splitting schemes of order higher than two. *Applied Numerical Mathematics*, 54(1):23 – 37, 2005.

[67] S. Blanes, F. Casas, P. Chartier, and A. Murua. Optimized high-order splitting methods for some classes of parabolic equations. *Math. Comp.*, 82(283):1559–1576, 2013.

[68] Vladimir E. Zakharov. Stability of periodic waves of finite amplitude on a surface. *J. Appl. Mech. Tech. Phys.*, 9(2):190–194, 1968.

[69] Alexander I. Dyachenko, Evgenii A. Kuznetsov, Michael Spector, and Vladimir E. Zakharov. Analytical description of the free surface dynamics of an ideal fluid (canonical formalism and conformal mapping). *Phys. Lett. A*, 221:73–79, 1996.

[70] George G. Stokes. On the theory of oscillatory waves. *Transactions of the Cambridge Philosophical Society*, 8:441–455, 1847.

[71] George G. Stokes. On the theory of oscillatory waves. *Mathematical and Physical Papers*, 1:197–229, 1880.

[72] L. W. Schwartz and J. D. Fenton. Strongly nonlinear waves. *Ann. Rev. Fluid. Mech*, 14:39–60, 1982.

[73] Leonard W. Schwartz. Computer extension and analytic continuation of Stokes' expansion for gravity waves. *J. Fluid Mech.*, 62(3):553–578, 1974.

[74] J. F. Toland. On the existence of a wave of greatest height and Stokes's conjecture. *Proc. R. Soc. Lond. A*, 363:469–485, 1978.

[75] Malcolm A. Grant. The singularity at the crest of a finite amplitude progressive Stokes wave. *J. Fluid Mech.*, 59(2):257–262, 1973.

[76] M. S. Longuet-Higgins and E. D. Cokelet. The deformation of steep surface waves on water i. a numerical method of computation. *Proc. R. Soc. Lond. A*, 350:1–26, 1976.

[77] Michael S. Longuet-Higgins. On an approximation to the limiting Stokes wave in deep water. *Wave Motion*, 45:770–775, 2008.

[78] Jianke Yang. Newton-conjugate-gradient methods for solitary wave computations. *J Comput. Phys.*, 228(18):7007–7024, 2009.

[79] D.E. Pelinovsky and Yu.A. Stepanyants. Convergence of petviashvili's iteration method for numerical approximation of stationary solutions of nonlinear wave equations. *SIAM J. Numer. Anal.*, 42:1110–1127, 2004.

[80] Sergey A. Dyachenko, Pavel M. Lushnikov, and Alexander O. Korotkevich. The complex singularity of a Stokes wave. *JETP Letters*, 98(11):675–679, 2014.

[81] Sergey A. Dyachenko, Pavel M. Lushnikov, and Alexander O. Korotkevich. Branch Cuts of Stokes Wave on Deep Water. Part I: Numerical Solution and Padé Approximation. *Studies in Applied Mathematics*, 137(4):419–472, 2016.

[82] Pavel M. Lushnikov. Structure and location of branch point singularities for Stokes waves on deep water. *Journal of Fluid Mechanics*, 800:557594, 2016.

[83] Pavel M. Lushnikov, Sergey A. Dyachenko, and Denis A. Silantyev. New conformal mapping for adaptive resolving of the complex singularities of stokes wave. *Proceedings of the Royal Society of London A: Mathematical, Physical and Engineering Sciences*, 473(2202), 2017.

[84] Lev V. Ovsyannikov. Dynamics of a fluid. *M.A. Lavrent'ev Institute of Hydrodynamics Sib. Branch USSR Ac. Sci.*, 15:104–125, 1973.

[85] D. Meison, S. Orzag, and M. Izraely. Applications of numerical conformal mapping. *J. Comput. Phys.*, 40:345–360, 1981.

[86] S. Tanveer. Singularities in water waves and Rayleigh-Taylor instability. *Proc. R. Soc. Lond. A*, 435:137–158, 1991.

[87] S. Tanveer. Singularities in the classical Rayleigh-Taylor flow: formation and subsequent motion. *Proc. R. Soc. Lond. A*, 441:501–525, 1993.

[88] Vladimir E. Zakharov, Alexander I. Dyachenko, and Oleg A. Vasiliev. New method for numerical simulation of nonstationary potential flow of incompressible fluid with a free surface. *European Journal of Mechanics B/Fluids*, 21:283–291, 2002.

[89] A. I. Dyachenko, V. E. Zakharov, and E. A. Kuznetsov. Nonlinear dynamics of the free surface of an ideal fluid. *Plasma Physics Reports*, 22:829–840, Oct 1996.

[90] Vladimir I. Petviashvili. Equation for an extraordinary soliton. *Sov. J. Plasma Phys.*, 2:257–258, 1976.

[91] P. M. Lushnikov. Dispersion-managed soliton in a strong dispersion map limit. *Opt. Lett.*, 26:1535 – 1537, 2001.

[92] Taras I. Lakoba and J. Yang. A generalized Petviashvili iteration method for scalar and vector Hamiltonian equations with arbitrary form of nonlinearity. *J. Comput. Phys.*, 226:1668–1692, 2007.

[93] John M Williams. *Tables of Progressive Gravity Waves.* Pitman, London, 1985.

[94] Jianke Yang. *Nonlinear Waves in Integrable and Nonintegrable Systems.* SIAM, 2010.

[95] J. M. Williams. Limiting gravity waves in water of finite depth. *Phil. Trans. R. Soc. Lond. A*, 302(1466):139–188, 1981.

[96] J. M. Williams. Near-limiting gravity waves in water of finite depth. *Phil. Trans. R. Soc. Lond. A*, 314(1530):353–377, 1985.

[97] J. P. Boyd. *Chebyshev and Fourier Spectral Methods: Second Revised Edition.* Dover Publications, 2001.

[98] T. W. Tee and L. N. Trefethen. A Rational Spectral Collocation Method with Adaptively Transformed Chebyshev Grid Points. *SIAM J. SCI. COMPUT.*, 28:1798–1811, 2006.

[99] F. D. Gakhov. *Boundary Value Problems*. Pergamon Press, New York, 1966.

[100] Andrei D. Polyanin and Alexander V. Manzhirov. *Handbook of Integral Equations: Second Edition*. Chapman and Hall/CRC, Boca Raton, 2008.

[101] B Chen and PG Saffman. Numerical evidence for the existence of new types of gravity-waves of permanent form on deep-water. *Studies in Applied Mathematics*, 62(1):1–21, 1980.

[102] I. S. Gandzha and V. P. Lukomsky. On water waves with a corner at the crest. *Proc. R. Soc. A*, 463:1597–1614, 2007.

[103] Maklakov V. Dmitri. Almost–highest gravity waves on water of finite depth. *Euro. Jnl of Applied Mathematics*, 13:67–93, 2002.

[104] I.M. Gel'fand. Some problems in the theory of quasilinear equations. *Transl., Ser. 2, Am. Math. Soc.*, 29:295–381, 1963.

[105] J. H. Maddocks. Stability and folds. *Archive for Rational Mechanics and Analysis*, 99(4):301–328, Dec 1987.

[106] G. A. Chandler and I. G. Graham. The Computation of Water Waves Modelled by Nekrasov's Equation. *SIAM Journal on Numerical Analysis*, 30(4):1041–1065, 1993.

[107] Aleksandr I. Nekrasov. On steady waves. *Izv. Ivanovo-Voznesensk. Polytech. Inst.*, 3:52–56, 1921.

[108] Michael Longuet-Higgins and Mitsuhiro Tanaka. On the crest instabilities of steep surface waves. *Journal of Fluid Mechanics*, 336:5168, 1997.